SANDIA REPORT

SAND2005-0072
Unlimited Release
Printed January, 2005

Characterizing the Effects of Heating Rate and Scale on Microscale Explosive Ignition Criteria

Everett S. Hafenrichter and Robert J. Pahl

Prepared by
Sandia National Laboratories
Albuquerque, New Mexico 87185 and Livermore, California 94550

Sandia is a multiprogram laboratory operated by Sandia Corporation,
a Lockheed Martin Company, for the United States Department of Energy's
National Nuclear Security Administration under Contract DE-AC04-94AL85000.

Issued by Sandia National Laboratories, operated for the United States Department of Energy by Sandia Corporation.

Available to DOE and DOE contractors from
U.S. Department of Energy
Office of Scientific and Technical Information
P.O. Box 62
Oak Ridge, TN 37831

Telephone: (865)576-8401
Facsimile: (865)576-5728
E-Mail: reports@adonis.osti.gov
Online ordering: http://www.osti.gov/bridge

Available to the public from
U.S. Department of Commerce
National Technical Information Service
5285 Port Royal Rd
Springfield, VA 22161

Telephone: (800)553-6847
Facsimile: (703)605-6900
E-Mail: orders@ntis.fedworld.gov
Online order: http://www.ntis.gov/help/ordermethods.asp?loc=7-4-0#online

SAND2005-0072
Unlimited Release
Printed January 2005

Characterizing the Effects of Scale and Heating Rate on Micro-Scale Explosive Ignition Criteria

Everett S. Hafenrichter and Robert J. Pahl
Explosive Components Facility
Sandia National Laboratories
P.O. Box 5800
Albuquerque NM 87185-1452

Abstract

Laser diode ignition experiments were conducted in an effort to characterize the effects of scale and heating rate on micro-scale explosive ignition criteria. Over forty experiments were conducted with various laser power densities and laser spot sizes. In addition, relatively simple analytical and numerical calculations were performed to assist with interpretation of the experimental data and characterization of the explosive ignition criteria.

Acknowledgements

The authors would like to thank Anita Renlund, who secured the Laboratory Directed Research and Development (LDRD) funds that made this project possible, and who assisted with technical direction. The authors would also like to acknowledge Shane Snedigar, who built and calibrated the five-color pyrometry system, and Adam Wadin, who was responsible for performing the experiments and handling all the instrumentation associated with the experimental work. Finally, the authors thank Tom Hafenrichter and Eric Welle for their assistance with the revision of this document.

Contents

List of Figures

List of Tables

1 Introduction

1.1 Goal

The primary goal of this study is to investigate the effects of scale and heating rate on the critical temperature of explosives. The critical temperature is defined as the temperature at which the energy balance between chemical energy release and thermal conduction favors thermal runaway within the explosive. It is known that critical temperatures are scale dependant, and furthermore, it is known that the critical temperature is affected by heating rate; however, experiments that characterize the effects of scale and heating rate on critical temperature have typically been conducted at large scales with relatively low heating rates. The recent trend towards the miniaturization of explosive devices underscores the need to understand the critical temperature of explosives at small scales and high heating rates.

1.2 Approach

The present work seeks to build this understanding by performing experiments that allow for the fast thermal heating of a relatively small portion of an explosive. This is accomplished by using a high powered laser diode and focusing optics. The focusing optics are used to produce a small laser spot size on the surface of the explosive, thereby directly thermally heating a correspondingly small volume of the explosive. By using relatively high laser power densities, it is possible to quickly heat this small portion of the explosives to the critical temperature. If the power density is high enough, the area of the explosive directly heated by the laser radiation will reach the critical temperature before a significant amount of energy is conducted away from the ignition region.

From a research perspective, using lasers to initiate explosives is advantageous because it allows the researcher to closely control and measure how much energy is delivered to the explosive and the rate at which that energy is delivered (power). Furthermore, the researcher has some degree of control over how much of the explosive material is heated by the laser. This is accomplished primarily by varying the spot size produced by the laser, as control over the penetration depth of the laser light into the explosive is much more limited and difficult to measure. Finally, using a laser to initiate the explosive makes it possible to incorporate a recently developed diagnostic technique that provides valuable ignition-related data (this technique is described in Section 3.1).

1.3 Background

This paper addresses the laser initiation of condensed phase high explosives. Four distinct regions can be defined when an explosive is heated directly by laser radiation (see Figure 1).[1-3] The first region (Region I) occurs with low power densities where the laser causes the explosive to reach a steady-state temperature lower than the temperature required for a self-sustained reaction (often referred to as the critical temperature). Ignition, therefore, is not achieved. This region is called the conduction-dominated region because at the steady-state temperature, heat is conducted away from the ignition region at a rate equal to the input of laser energy. As power density is increased, Region

II is approached, and the critical temperature is reached before the steady-state temperature, thereby achieving ignition. Further increases in power density heat the explosive at a higher rate, and therefore less time is required to reach the critical temperature. In these cases, less heat is conducted away from the ignition region, and the ignition energy is therefore lower; thus, Region II is called the conduction-affected region. Region III is approached when power density is increased to still higher levels. In Region III, the explosive is heated so quickly that there is insufficient time for a significant amount of heat to conduct away from the ignition region. Therefore, ignition energy is constant in this conduction-unaffected region. Finally, when the power density becomes extremely high, the laser light is sufficient to ablate the surface of the explosive, and the explosive is essentially shock heated (Region IV, not shown in Figure 1).

Laser initiation of explosives has been studied since the 1960's.[4] Much of the work has used high-power, Q-switched lasers to shock heat the explosive (Region IV). These experiments were largely successful in promptly initiating insensitive explosives,[4-10] but the large and expensive high power lasers used in these experiments limited the practical application of such laser-initiated devices in ordnance systems.

The small size and relatively low cost of laser diodes seem to make them ideal for use in practical laser-initiated devices. Unfortunately, there are some disadvantages associated with laser diodes, such as high beam divergence and relatively low output power. As a result, most previous studies with laser diodes have been conducted with relatively low power densities, in the conduction-affected region.[11-21] In this region, ignition occurs on relatively long time scales, typically hundreds of microseconds to milliseconds.

In early 2001, Sandia National Laboratories began work that was geared towards reducing the ignition delay of laser diode ignited devices. The research used the most advanced laser diode and optics technology available to design a fast functioning laser detonator. With the latest in semiconductor and optics technology, it is now possible to achieve power densities that approach five megawatts per square centimeter (MW/cm^2) with laser diodes. Although power densities of this level are insufficient for shock initiation of the explosive (Region IV), they are high enough to allow for studies well into the conduction-unaffected region (Region III).

In Region III, the laser energy heats the explosive in a purely thermal manner, meaning the explosive deflagrates once ignited. Thus, the explosive must undergo a deflagration-to-detonation transition (DDT) to achieve detonation. As a result, laser diode-initiated detonators must use explosives that readily undergo the DDT process.

Two DDT explosives commonly used by Sandia National Laboratories (SNL) are CP[22] and BNCP.[23] These two explosives can be thought of as a compromise between classical primary explosives and secondary explosives. They both DDT much more readily than classical secondary explosives, such as HMX and RDX, but are much less sensitive to means of accidental initiation (such as electrostatic discharge, impact, friction, etc.) than classical primary explosives, such as the heavy metal azide and styphnates. Previous work has shown that CP and BNCP are readily initiated by laser diodes, provided that

measures are taken to increase the absorptivity of the explosive to the spectrum of the laser.[1-3, 17, 18]

Most high-powered laser diodes emit light with a wavelength near 800 nm, which is in the near infrared (NIR). Unfortunately, most explosives do not naturally absorb NIR light, and CP and BNCP are no exception. Typically, the explosives are mixed with a dopant such as carbon black so that the laser light is more readily absorbed. This serves to greatly increase ignition sensitivity.

Previous work conducted by the author has indicated that BNCP has superior laser sensitivity when compared to CP.[2] Thus, the experiments presented in this paper are conducted with BNCP-based ignition increment mixtures.

2 Description of Experiments

2.1 Instruments

The laser used for all experiments was a Model S35-808-1 fiber coupled laser diode array, manufactured by Apollo Instruments, Inc. The laser's driving electronics are custom built into a single housing that is co-located with the laser diode unit. This helps to reduce circuit inductance, which allows for fast rise times and fall times. Pulse width is continuously variable from zero to 5 μs. A photograph of the laser diode is shown in Figure 2.

The output of the laser diode array is coupled to a 100 micron core diameter fiber optic using focusing optics. The 808 nanometer wavelength laser is capable of reaching power levels as high as 70 watts from the fiber output, with continuous variability below this level.

2.2 Detonator

A schematic of the laser diode detonator is shown in Figure 3. The detonator consists of a focusing optics assembly and a charge holder assembly. The focusing optics assembly collimates the light from the 100 micron core diameter fiber and then refocuses the light to the desired spot size on the surface of the explosive. The charge holder is bonded to the focusing optics assembly, and the ignition increment is pressed directly on top of a sapphire window that is bonded to the optics assembly.

The ignition increment consists of 25 micron mean-particle size BNCP explosive mixed with one percent carbon black by weight. BNCP is a DDT explosive that is ideal for use in laser diode initiated detonators. Past experiments by the author have shown that this particular configuration (25 micron mean particle size and one percent carbon black) is superior in sensitivity and consistency compared to other explosive mixtures by the author.[2, 3]

The diameter of the charge cavity is 0.08 inches. The ignition increment was pressed to a nominal height of 0.04 inches using a pressure of 16 ksi. A CP DDT increment was pressed on top of the ignition increment to a nominal height of 0.08 inches. The DDT increment consisted of coarse particle size CP pressed to a pressure of 10 ksi. Although most WR components contain 3 DDT increments and an output pellet, only one DDT increment was used in these experiments in an effort to reduce net explosive weight and therefore mitigate damage to expensive diagnostic hardware. The single DDT increment was incorporated to ensure that the laser initiated ignition increment was capable of initiating the DDT increment.

2.3 Test Matrix

A test matrix was devised to investigate and characterize ignition using several different laser spot sizes and several different laser power densities. Four nominal spot sizes were investigated, including 200, 100, 50, and 40 microns. The experiments spanned over six

different nominal power densities, including 0.2, 0.5, 0.75, 1.0, 2.5, and 4.5 MW/cm^2. While desirable spot sizes and power densities were chosen when possible, practical limitations associated with the capabilities of the laser (power and pulse width) and the capabilities of the focusing optics (spot size and throughput efficiency) also played a role in determining the test matrix. The lowest allowable power density level was determined by estimating the lowest power density that would initiate the explosive before significant heat was conducted away from the ignition region. It was estimated that ignition could take no longer than 1-2 μs for this to be the case, which corresponds to an estimated power density of about 0.2 MW/cm^2. With the capabilities of the laser, the largest allowable spot size that corresponds to 0.2 MW/cm^2 is 200 microns. The smallest spot size that can be reliably produced by present-day optics technology from a 100 micron, 0.22 NA fiber is 40 microns (the vendor attempted to achieve 25 microns, but failed). The largest power density that could be achieved with the 40 micron spot size was 4.5 MW/cm^2. Thus, the limits of spot size and power density were determined, and the test matrix was populated between these limits as budget and schedule allowed. The tabulated test matrix is shown in Table 1. When possible, five experiments were performed at each test condition.

A series of "crowbar" experiments was also conducted. The crowbar experiments involved using a constant power density but variable pulse width. The objective was to determine how much laser energy, if any, was required to sustain the reaction in the explosive once ignition occurred. These experiments were conducted using the highest achievable power density (4.5 MW/cm^2), which corresponds to the smallest achievable spot size (40 μm).

3 Experimental Set-Up

3.1 Past Work

A diagnostic tool that allows the researcher to make direct measurements near the ignition region in confined, laser initiated energetic devices was developed by Sandia in LDI work that began in the spring of 2001.[1] In early experiments,[1, 2] the technique involved using a dual fiber optic cable assembly that consisted of a "delivery" fiber and a "diagnostic" fiber. The delivery fiber is coupled to the laser and delivers the laser light to the focusing optics, and ultimately the explosive. The diagnostic fiber basically serves as a "pick-up" fiber. The light gathered by the diagnostic fiber from the reflected laser signal and the self-light of the reacting explosive is transferred to various pieces of diagnostic equipment. The data are then analyzed in an effort to gain insight into the ignition process. A schematic of the experimental set-up is shown in Figure 4.

In initial work, the light gathered by the diagnostic fiber was piped to a Thorlabs PDA-55 10 MHz photodetector. Early experiments proved that the diagnostic technique could provide valuable data concerning the ignition process.[1, 2] With the proper settings, the signal from the photodetector closely follows the intensity of the laser light reflected from the explosive surface. The photodetector signal therefore corresponds to the overall intensity of the laser signal, assuming constant reflectivity of the explosive. The photodetector is able to track the increase in intensity due to the rise of the laser signal when the laser is functioned, and the signal reaches a maximum when the laser power reaches its maximum. When the explosive begins to react, it affects the photodetector signal in a noticeable manner. This therefore allows the researcher to directly measure "ignition delay," the time required for the laser to ignite the explosive.

There are several challenges associated with using this particular diagnostic technique. First of all, it can be difficult to achieve an optimum signal from the photodetector. The most straightforward way to modify the amount of light that reaches the detector face is to move the position of the fiber output with respect to the detector face. As the light leaves the fiber output, it diverges according to the numerical aperture of the fiber (0.22). If the diagnostic fiber output is located too close to the detector face the detector will saturate and all ignition delay data are lost. In contrast, if the diagnostic fiber output is located too far from the detector face the signal is extremely weak, making it difficult to extract useful ignition delay data. To further complicate matters, the signal strength changes from experiment to experiment depending on power density, spot size, and the alignment of the diagnostic fiber to the focusing optics.

Another challenge associated with this technique is the speed with which the explosive is ignited. In several experiments, and especially in those that use high laser power density, the explosive is ignited extremely quickly, even before the laser reaches its maximum level (i.e., the ignition delay is shorter than the laser rise time). This can make it difficult to accurately determine the ignition delay time from the photodetector signal. To further complicate matters, the signal does not always increase upon ignition. While it may seem intuitive that ignition would cause an increase in the photodetector signal due to the self-

light of the explosive, this is not always the case. The plasma formed by the reacting explosive does produce light, but it is also a strong absorber of light (stronger than the unreacted explosive). This implies that the signal from the photodetector could increase or decrease upon ignition, depending on whether the light emitted by the plasma is more or less intense than the laser light absorbed by the plasma when compared to the unreacted explosive.

3.2 Present Work

The present work relies on the same pick-up fiber approach as previous work, but uses a fiber optic bundle consisting of seven fibers instead of just a dual fiber assembly. The fibers are arranged in a rosette pattern with six fibers surrounding the single center fiber. The center fiber is utilized as the delivery fiber, and the other six fibers are utilized as diagnostic fibers. The additional diagnostic fibers are used to maximize the chances of obtaining a strong but unsaturated signal from its corresponding photodetector. A schematic of the set-up is shown in Figure 5.

Five of the six diagnostic signals are sent to various photodetectors. Three of the signals are sent directly into three photodetectors with different sensitivities, including a Thorlabs 10 MHz detector, a New Focus 125 MHz detector, and a New Focus 1 GHz detector. The fourth signal is sent to a Thorlabs 10 MHz detector through a narrow bandpass filter that passes wavelengths near the laser wavelength, while the fifth signal is sent to a Thorlabs 10 MHz detector through a bandstop filter that removes wavelengths near the laser wavelength.

The sixth and final signal is sent to a five-color pyrometry system. The pyrometry system was developed specifically for use in this program, and will be discussed in detail in the following subsection.

Output from the DDT column is detected by a single 1 mm core diameter fiber. This fiber, which is damaged and subsequently re-cleaved after each experiment, is run to a 10 MHz detector, as shown in Figure 5.

3.2.1 Five Color Pyrometer

The main point of interest in this project is to determine the timing and phenomenology of laser initiation of the BNCP initial pressing (IP). In determining the timing, the various optical detectors described above were used to measure changes in emitted and reflected light. To gain more information on the phenomenology of initiation, more sophisticated diagnostics were in order. In particular, it was desirable to measure temperature of the igniting surface of the BNCP IP to characterize how the surface was heated by laser illumination from its initial condition to the point of initiation.

When measuring the temperature of a surface, there are two general classes of diagnostics: contact and non-contact. Contact thermometers, such as thermocouples, are useful because they are easy to calibrate, and the data reduction is straightforward. Unfortunately, contact thermometers are inherently slow, offering time resolutions on the order of milliseconds. Since the LDI tests performed here result in initiation times on the

order of microseconds or less, it seemed unlikely that any contact thermometer would provide useful data. In addition, the small nature of the laser spot and of the detonator itself makes the introduction of such a diagnostic difficult if not impossible.

The second class of temperature diagnostics is non-contact thermometers. In this type of diagnostic, the light emitted by a hot surface is recorded and used to calculate the temperature of that surface. This type of diagnostic has the benefit of being remarkably fast, with the speed mainly limited by the strength of the optical signal coming from the surface and the corresponding sensitivity and speed of the photodetectors. These advantages make non-intrusive optical temperature measurement the ideal choice for this work.

When considering optical temperature measurement, there are two basic approaches. Both are discussed at length in the literature;[24] therefore, only the basic principles are discussed here. The first approach is absolute pyrometry where the intensity of the light emitted from a surface is directly used to calculate a temperature. This approach has the advantage that there are no assumptions or approximations used in the calculation of temperature. The disadvantage is that every detail and material property of the optical system must be known to calculate the temperature. This includes characterizing the reflectivity of the surface of interest, the transmission losses of every component in the system, the geometry of the collection optics, the absolute calibration of the photodetector(s), accounting for any stray or reflected light in the system, etc. Obviously, the measurement and characterization of all these parameters is not always practical, and some of these parameters are difficult to measure in the test setup used in this work. For example, the geometry of the collection optics (i.e. how much light from the surface was collected and entered into the collection fiber) changed for each detonator-fiber bundle assembly, and the enclosed design of the delivery-collection optics made measuring this parameter difficult.

A second approach to optically measuring temperature is relative or ratio pyrometry. This approach is often more practical, and was used in the present work. The details of this approach can be found in the literature,[24] so only the basic principles are discussed here. In this approach, light emitted by a surface is measured at two or more wavelengths. The ratio of these signals is then compared to the ratio predicted by Planck's law, and a temperature is calculated. The advantage of this technique is that most of the details of the test setup necessary for absolute pyrometry are not needed. As a result, implementation of this diagnostic is much more straightforward and practical. The disadvantages of this technique are that the optical components used in the test must be identical to those used during calibration, and the optical material properties of the surface must be independent of wavelength and temperature. In the present experimental setup, the optical components change from test to test as both the delivery-collection fiber bundle and the lenses of the detonator are consumed. This was not considered to be a serious problem since the properties of both were expected to be fairly consistent from test item to test item. In contrast, the requirement that the material properties of the surface not change with respect to wavelength and temperature most likely was not strictly true. In fact, all materials show some wavelength dependency in their optical

properties. Therefore, the data reduction methodology must be carefully derived to account for these discrepancies.

3.2.1.1 Wavelength Selection

The first step in designing the pyrometer was wavelength selection. In these experiments, the temperature range of the IP surface was expected to range from room temperature to ~2500K. The basis of multi-color pyrometry is Planck's law given by

$$e(\lambda,T)=\frac{C_1}{\lambda^5\left(\exp\left[\frac{C_2}{\lambda T}\right]-1\right)}, \quad (1)$$

where e is the blackbody heat flux from a surface, T is the surface temperature, λ is the wavelength of light, C_1 =37413 W-μm^4/cm^2, and C_2 =14388 μm-K. The maximum wavelength of Plank's law is given by Equation 2, which is often referred to as Wien's Law:

$$\lambda_{max}=\frac{2898}{T}\ \mu\text{m K}. \quad (2)$$

When making temperature measurements, multi-color pyrometry is more sensitive to temperature if the wavelengths chosen are on the 'blue' or short wavelength side of maximum. However, Planck's law rapidly falls to zero at shorter wavelengths, and so the window of usable wavelengths on the 'blue' side of the maximum is narrow. Thus the wavelengths must be as close to the maximum as possible. Given our large range of temperature, this meant that at the cold temperature (room temperature), λ should be close to ~9600 nm, and at the hottest temperature (~2500K), λ should be close to ~1200 nm. Other wavelengths would ideally be interspersed between these two values.

In addition to sensitivity concerns, there were other issues considered when choosing the wavelengths for the pyrometer. In particular, the path of light from the detonator IP surface to the detectors passed through optical fiber and open air. Both of these transmission media have their respective absorption bands. The transmission curve for air is well known[24] and will not be reproduced here. The fiber used in this work was a broadband 100 μm diameter fiber manufactured by Polymicro Technologies, LLC, with a known and well-characterized transmission curve. It was imperative to select wavelengths outside of the absorption bands of these two materials to obtain the maximum signal throughput and to reduce false signals.

A third issue considered in the selection of wavelengths was the characteristics of detectors. Silicon (Si) detectors typically have a useable range of ~300 to ~1000 nm. Similarly, photomultiplier tubes (PMT's) typically have ranges spanning ~200 to ~900 nm. Both of these detectors were readily available with bandwidths up to the GHz range, with PMT's being more sensitive. Indium-Gallium-Arsenide (InGaAs) detectors (with cooling) can have ranges from 500 to 2600 nm. The drawback with InGaAs detectors,

however, is that they are generally slower (or have a lower bandwidth) than Si detectors for a given input power level.

In addition to these considerations, the pyrometer designed and fabricated in this work was also designed to be used in other work directed towards characterizing the combustion of aluminized energetic materials, which meant that the spectral location of AlO emission peaks must be avoided by the wavelengths chosen for this system. Based on a rough optimization of all of these considerations, it was decided to utilize two of the five wavelengths in the range covered by PMT's and the remaining three detectors in the range of InGaAs detectors. The specific wavelengths, narrow bandpass filters, and detectors are listed in Table 2.

3.2.1.2 Pyrometer Layout

Once the wavelengths were selected, the general layout of the pyrometer was considered. Pyrometers can be arranged in a number of different configurations depending on the number of wavelengths considered and the wavelengths themselves. In general, it is advantageous to disperse the wavelengths into each detector in a way that maximizes signal strength. To accomplish this, two general approaches are common, including the use of a dispersion media, such as a prism, or wavelength filters. A prism-type system has the advantage of high throughput, since there is only one optic (the prism) that will absorb or reflect light. It has the disadvantage that the prism itself can be expensive and the setup of the optics can be more challenging. The filter-type system has the opposite advantages/disadvantages in that it is relatively inexpensive and easy to implement, but suffers from reduced signal throughput. A review of the literature[25-29] indicated that filter-type pyrometers are more frequently implemented, and thus it was decided to implement this type of system here.

The next option in the pyrometer layout design is the location of the detectors and beam splitters. The layout most often seen in the literature is one where the detectors are in order of increasing or decreasing wavelength as shown in Figure 6. Dichroic beamsplitters are usually implemented so that the longer (or shorter) wavelengths passing through are minimally attenuated. The attenuation from these dichroic optics, however, is not negligible. In fact, these optics can attenuate up to 20% of the light passing through the optic. When this fact was considered, it was decided that an alternative layout would better balance the attenuation of each wavelength channel in a five-color design. The layout of the five color pyrometer used in this work is shown in Figure 7. As this figure shows, the 900 nm and 1270 nm channels were attenuated by three dichroic beamsplitters and the remaining channels were attenuated by only two. The long pass dichroic beamsplitters, which were manufactured by Spectragon, had cutoffs of 850 nm, 1100 nm, 1500 nm, and 1850 nm.

3.2.1.3 Detector and Amplifier Design

The final consideration in pyrometer design was the design and selection of the detectors, pre-amplifiers, and amplifiers for each channel. Since the goals and scope of this work did not include advancing the state-of-the-art in detectors or amplifiers, commercial devices were used for all components.

It was necessary to estimate the light energy expected at each detector face before components could be selected. Assuming the thermal energy emitted at the heated surface of the BNCP IP behaved as a diffuse source and that the first lens collecting the light from the surface will collect all light available, the estimate of the energy reaching a detector, E, was given by

$$E = q'' \cdot A_s \cdot \tau_{tot}, \tag{3}$$

where *q"* is the energy leaving the HE surface collected by the detonator lenses, A_s is the heated spot size on the BNCP IP, and τ_{tot} is the total transmittance of the system for a given detector. In detail, *q"* is given by

$$q'' = n^2 \int_0^{2\pi} \int_0^{\theta_s} I(\theta,\phi)\cos\theta \sin\theta \, d\theta \, d\phi = \sigma T^4 f(\lambda_c, \Delta\lambda, T) n^2 \sin^2 \theta_s, \tag{4}$$

where n is the index of refraction of the sapphire window at the IP surface, $I(\theta,\phi)$ is the intensity of the radiation emitted by the surface, σ is the Stefan-Boltzmann constant, T is the surface temperature in Kelvin, $f(\lambda_c,\Delta\lambda,T)$ is defined below, and θ_s is the limiting angle of light collected by the first lens. For angles larger than θ_s, light passing through the detonator lens system does not enter the fiber due to the collection fiber numerical aperture (*N.A.*). θ_s is related to the *N.A.* of the optical fiber by the principle of optical invariance,[24] and can be written in terms of the fiber and spot size diameter as

$$\sin\theta_s = \frac{N.A.}{n} \frac{d_f}{d_s}, \tag{5}$$

where d_f is the fiber core diameter and d_s is the spot size diameter. *q"* then becomes

$$q'' = \sigma T^4 f(\lambda, \Delta\lambda, T)(N.A.)^2 \left(\frac{d_f}{d_s}\right)^2. \tag{6}$$

The remaining term in Eq (6) yet to be defined is the function $f(\lambda_c,\Delta\lambda,T)$. This function is the fraction of the total blackbody emission flux curve, described by Planck's Law, which passes through the narrow band pass filter in front of each detector. It is a function of the center wavelength, λ_c, and the half maximum, full width of the filter, $\Delta\lambda$, as well as a function of the IP surface temperature, T. f can be written as

$$f(\lambda_c, \Delta\lambda, T) = F\left(\left(\lambda + \frac{\Delta\lambda}{2}\right)T\right) - F\left(\left(\lambda - \frac{\Delta\lambda}{2}\right)T\right) \tag{7}$$

using the fractional function, $F(\lambda T)$, which has been tabulated and can be found in any standard radiation heat transfer textbook.[30, 31]

The last term in Eq (3) to be defined is τ_{tot}, the total transmittance of the system. It is expressed as the product of the transmittances of each of the components between the front surface of the IP and the detector face. Table 3 shows the estimated value for each component. It was expected that these values would change for each wavelength, and so the value of τ_{tot} calculated using these data was used as a rough estimate. It was therefore expected that these values would have significant errors.

Using the assumed values to calculate τ_{tot}, the energy reaching each detector as a function of temperature was estimated. The results of these estimates are plotted in Figure 8. As this figure shows, the estimated energy reaching each detector varied with temperature and ranged from < 0.1 nW to as high as > 1 μW. These data clearly indicated that the detector and amplifier designs must be chosen wisely to detect these low powers. In addition, the events to be captured were expected to occur in times less than 1 μs, and so it was decided that the detectors and amplifiers must have high signal bandwidths. This combination of low signal strength and high speeds resulted in a challenging detector design.

For the 700 nm and 900 nm channels, it was decided to use PMT's due to their high sensitivity and high speeds. In particular, Hamamatsu PMT model R928 was chosen for both channels. This model's sensitivity at 700 nm and 900 nm was approximately 30 mA/W and 0.05 mA/W, respectively. It was thought that the reduced sensitivity at longer wavelengths could be overcome by selecting the appropriate amplifier. The PMT's were then incorporated into detector housings with appropriate circuitry by the PMT+ company. The amplifier chosen for each channel was an AC coupled low noise bipolar voltage amplifier (model 322-6) produced by Analog Modules, Inc (described below). This amplifier has a manufacturer's stated bandwidth of 100 MHz and a gain of 40 dB. The stated noise was ~400 $pV/Hz^{1/2}$. It was thought that the gain provided by this amplifier would be sufficient to detect signal levels > 1 nW, even with the relatively poor sensitivity at 900 nm.

For the remaining near infrared (NIR) channels, it was decided to use thermoelectrically cooled InGaAs photodiodes. The photodiodes were selected from models available from Judson Technologies, which has a large selection of TE cooled detectors. The first parameter considered in selecting the photodiodes was the time constant of the detector, $\tau = RC$, where C is the capacitance of the diode and R is the impedance of the device (nominally 50 ohms). The capacitance of the diode usually decreases with decreasing detector size; therefore the smallest detector was desirable. The second parameter considered was the noise equivalent power (NEP), which is a measure of the inherent noise of the photodiode. As mentioned, smaller diodes have smaller NEP. Both of these parameters competed with the difficulty of focusing the light beam down to a spot size small enough to fit on the detector face. The final parameter of interest was the sensitivity of the detector, which gives an estimate of the current output of the detector when irradiated. The sensitivity is important in the sizing of amplifiers discussed next. A summary of all of these parameters for each detector is listed in Table 4.

The next step in the design of the NIR channels is the sizing of the amplifiers. The amplification of the detector output was completed in two steps. First, a transimpedance amplifier (or preamplifier) was used to convert the current output of the diode into a voltage output with high gain. The second step was boosting the voltage signal to measurable levels using a voltage amplifier. To size the gain of the amplifiers correctly, the sensitivity was used with the estimated input power at each wavelength to calculate the current output of each detector. These data, along with manufacturer's data on various amplifier models, were then used to select the appropriate transimpedance and voltage amplifiers. The implemented design used an AC-coupled high-bandwidth bipolar transimpedance amplifier (model # 313A-1 manufactured by Analog Modules Inc.). The input capacitance of each transimpedance amplifier was matched to the capacitance of each NIR photodiode. The voltage amplifiers used for each channel were the same as those used for the PMT's, model 322-6 manufactured by Analog Modules Inc. A summary of the properties of each amplifier is provided in Table 5.

The total signal-to-noise ration (S/N) at each wavelength was estimated by summing the total noise of the detectors, preamplifiers and amplifiers and comparing the sum with an input signal of 10 nW. These results are shown in Table 6. These data indicated that for a 10nW input signal, the S/N of the system would be sufficient to see the thermal emissions of the solid surface against the noise inherent to the detector systems. According to the manufacturer's data, the noise from the voltage amplifier would be negligible. Indeed, it was hoped that the system would even yield usable data when light levels approached a 1 nW level. If the design criteria shown here were accurate, it was expected that the five-color pyrometer described here would be capable of producing acceptable results, even at low temperatures. As will be discussed below, however, the implemented design did not yield signals that could be used for temperature calculation at low temperatures. It will be shown that this is most likely due to large, unexpected sources of noise in the preamplifiers and amplifiers.

4 Experimental Method

The most critical parameter that affects ignition delay in laser ignited detonators is laser power density. Furthermore, from a research perspective, it is critical to accurately characterize the laser power density and energy delivered to the explosive in each experiment. Power density is a function of both laser power, Q, and spot size, d_s, while energy is a function of power and pulse width. Unfortunately, it is extremely difficult to directly measure the power of single, short duration laser pulses. Also, it is not sufficient to measure average power, as the rise time and fall time of the laser pulse can have significant affects on ignition if ignition occurs quickly.

A method was devised to accurately reconstruct a power density versus time plot for each experiment. The spot size and throughput efficiency delivered by each optics device was individually measured by the optics vendor. After arriving at Sandia National Laboratories, a random sample of the optics was chosen, and spot size and throughput efficiency were measured independently. Spot size was measured by inspecting a magnified image of the spot produced by the optics on a CCD array. Throughput efficiency was calculated by measuring the energy delivered by a pulse directly from the laser fiber and then measuring the energy delivered through the optics by an identical laser pulse. Sandia's measurements were consistent with the vendor's measurements, and therefore the values supplied by the vendor were used for all experiments.

Energy was measured using an Ophir energy meter that was specifically configured to measure the energy of short pulses of 808 nm light. Most experiments used a 5 μs laser pulse width. The rise time and fall time of the laser are about equal (300 ns), so the power delivered by the laser is first estimated by dividing the energy by the laser pulse width (this estimation will later be corrected with an exact, integrated calculation). For each experiment, the laser settings are modified until the laser delivers the desired energy that results in the desired power density, based on the calculated power and measured spot size delivered by the optics device. For example, if the target power density for the experiment is 1.0 MW/cm^2, and the optics device delivers a 49 micron spot size with 98% throughput efficiency, the target energy that should be delivered from the delivery fiber by a 5 μs pulse is calculated as:

$$E = \frac{(1x10^6 W/cm^2)\frac{\pi}{4}(0.0049cm)^2(5\mu s)}{0.98} = 96.2\mu J$$

Thus, to achieve this power density with this particular optics device, the laser power is adjusted until the laser pulse delivers approximately 96.2 μJ from the delivery fiber.

It was discovered that the fiber optic bundle assembly used in the experiments could be used to reconstruct the shape of the laser pulse delivered to the energy meter. This is accomplished by utilizing the diagnostic fibers to gather a portion of the reflected laser light from the surface of the energy meter. Figure 9 shows the photodetector signal from a diagnostic fiber while conducting an energy measurement. The intensity of the laser

light is directly proportional to power, implying that the signal from the photodetector is directly proportional to power. Since the energy delivered by the pulse is known, the proportionality constant can be calculated by integrating the photodetector signal to calculate an "unscaled" energy, and dividing the unscaled energy into the actual measured energy. In the example above, the unscaled energy that corresponds to the area under the curve in Figure 9 is 25.9 μJ. This gives a proportionality constant of 96.2/25.9 = 3.71. The subsequent multiplication of the signal in Figure 9 by 3.71 gives a power versus time plot. Finally, dividing the signal by the area of the laser spot size gives a power density versus time plot. The resulting plot is shown in Figure 10. For this particular experiment, the nominal power density would be reported as 1.0 MW/cm^2, but the actual temporal data would be used for all calculations.

5 Results

5.1 Photodetector Data

The unfiltered data from the three photodetectors can provide significant insight into the ignition of the BNCP ignition increment. This is achieved by comparing the photodetector signal from the experiment to the signal from the "set-up" shot performed just before the experiment. The set-up shot, which is performed to achieve the desired energy, and therefore power density, for the experiment, produces a photodetector signal similar to Figure 9. This value is convenient for use as "no-fire" baseline data, since the laser settings for the set-up shot are identical to the actual experiment, and since the surface of the energy meter is non-reactive. It is then possible to determine when the explosive begins to react by superimposing the photodetector signal from the experiment on the photodetector signal from the set-up shot.

Figure 11 shows photodetector data from an experiment performed with a power density of 0.2 MW/cm^2. The photodetector data from the experiment is superimposed on the baseline set-up data from just before the shot. The signals follow each other extremely closely until about 1.5 μs after the start of the laser pulse. At this point, the explosive begins to react, which causes a deviation of the photodetector signal from the baseline signal. Note that the signal *decreases* upon reaction.

Figure 12 shows similar data for an experiment performed with a much higher power density of 2.5 MW/cm^2. Note that the reaction starts much more quickly in this case, as the photodetector signal deviates from the baseline signal after just 350 ns. For this particular experiment, reaction is marked by an *increase* in the photodetector signal compared to the baseline signal.

5.2 Filtered Data

The previous section gave two examples which showed that the photodetector signal can increase or decrease with respect to the baseline signal. One possible explanation for this was briefly mentioned in Section 3.1. Before the explosive begins to chemically react, the signal to the photodetector solely represents the reflected laser light from the unreacted explosive. Chemical reaction, when it occurs, produces high-temperature ionized gases that emit light; however, this plasma also strongly absorbs light. Because of this strong tendency to absorb light, less laser light is reflected from the reacting explosive than the unreacted explosive. The overall signal can then either increase, decrease, or possibly stay the same, depending on the relative intensity of the light reflected by the unreacted explosive compared to the light emitted by the plasma.

Filters were utilized with two of the diagnostic fibers in an effort to deconvolute the competing effects of the reflected laser light and the light emitted by the plasma. The light from both fibers was collimated, passed through a filter, and then refocused onto the face of a Thorlabs PDA-55 10 MHz photodetector. A bandpass filter was incorporated with one fiber, while a bandstop filter was used with the other. The bandpass filter only

passed light near the laser wavelength, while the bandstop filter stopped a narrow bandwidth of light that included the laser wavelength.

It was expected that the signal from the bandstop filtered photodetector would essentially stay near zero until the explosive began to react, since the reflected laser light would be removed from the signal. In contrast, it was expected that the signal from the bandpass filtered photodetector would follow the rise of the laser, and that the signal would consistently decrease upon reaction, since the signal from the reflected laser light would decrease upon formation of the highly absorbing plasma.

The signals gathered from the bandstop filtered photodetector looked as expected (See Figure 13), although the signal strength was relatively low. The custom made filter removes the laser wavelength very well; however, the signal does not begin to increase until well after reaction, as indicated by the 10 MHz photodetector data also shown in Figure 13.

The signals gathered from the bandpass filtered photodetector were not as useful as hoped. First of all, as with the bandpass filtered photodetector, signal strength was low. Secondly, the off-the-shelf filter did not pass as narrow of a wavelength band as the bandstop filter stopped. Finally, it became evident that the reacting explosive produced ample light in the passing bandwidth. Thus, the signal did not solely consist of reflected laser light. For these reasons, the data from the bandpass filtered photodetector are not presented in this report (it is only mentioned here to document the effort). Future efforts, if any, would incorporate a custom designed, narrow bandpass filter, as well as a more sensitive photodetector or photomultiplier tube.

5.3 Pyrometry Data

5.3.1 Temperature Analysis

As was described in Section 3.2.1.1, the five color pyrometer was designed with five wavelengths spread out through the NIR spectrum so that temperatures could be calculated from ~700 K up to ~2500 K. It was expected that the three InGaAs detectors would be sensitive enough to measure temperatures in the lower end of this range, while the PMT's would be useful at the higher end of this temperature range. The system was designed to have adequate amplification and a noise level low enough to ensure a strong signal to noise ratio in the resulting voltage traces at all temperatures within this range. Unfortunately, the system did not perform as designed. In particular, it was discovered that the noise level present in the transimpedance and voltage amplifiers was much larger than calculations from the manufacturer's specifications predicted. The noise levels were so large that the signal to noise level was less than unity. As an example of the noise level present in each detector-amplifier channel, Figure 14 shows a chopped input light signal and the corresponding output of the preamplifier. The input signal level present was much larger than what was expected during a test, but the output of the amplifier was still too noisy to see the square-wave amplitude of the input signal. The result of this underperformance is that the data channels for each of the NIR photodetectors recorded

noise in every shot. Thus, it was not possible to measure the lower temperatures of the IP surface expected prior to ignition.

At the higher temperature ranges, the 700 and 900 nm channels were expected to be sufficiently amplified to record enough data to measure higher temperatures. Unfortunately, the 900 nm channel used an amplifier to boost the signal to measurable levels and this channel correspondingly had the same noise problems as those present in the NIR channels. The only recourse was to directly measure the unamplified output of the 700 and 900 nm channels. Unfortunately, the sensitivity of the PMT's at 900 nm was not large enough to produce measurable signals at early time scales. Figure 15 shows an example of the data recorded from these two channels along with voltage data from the other detectors in the LDI setup. As this figure shows, the signal strength of the 900 nm channel did not become measurable until approximately 0.5 μs after the 700 nm channel showed significant signal strength. This signal rise occurs long after the IP has ignited. At these late times, it is uncertain what was actually being measured since the IP surface most likely had deflagrated or was significantly different from a pristine surface at this point. In addition, recovery of post-test detonator parts showed complete destruction of the collection optics and IP window, further casting doubt on the phenomena being measured at post-ignition time scales.

Looking at the voltage data, it appears that in some experiments, the voltage level of the 700 nm channel starts to rise before IP ignition. Unfortunately, with the layout of the detectors, a temperature cannot be ascertained with a single channel. As was discussed in Section 3.2.1, the optical temperature measurement technique chosen for this work was multi-color pyrometry. This method demands that data from at least two different wavelength channels must be recorded to calculate temperature. A single channel does not allow a temperature measurement using a ratio pyrometry technique. Although absolute pyrometry could have been implemented at this point, the design of the detonator optics and lack of necessary calibration equipment did not allow it here. As a result, the pyrometry system was not able to measure pre-ignition temperatures, but the single active channel did yield some interesting qualitative and quantitative results and has indicated possible improvements to the photodetector layout as discussed in Section 5.3.2. Thus, although the attempt to implement a five-color pyrometer to measure temperatures during laser heating was unsuccessful, lessons learned from this attempt will aid in future pyrometry design, as well as LDI experimental equipment design.

5.3.2 Other Uses for the Pyrometry Data

While the pyrometry data failed to provide an accurate time history of the heating of the explosive, the data gathered from the system proved useful for characterizing other aspects of the ignition phenomenon. In many ways, the signals gathered by the pyrometer are similar to those gathered by the bandstop filtered photodetector mentioned in Section 5.2. Indeed, the pyrometer uses the same bandstop filter to remove the laser wavelength. However, with the pyrometer, the signal represents only a narrow wavelength bandwidth, while with the bandstop filtered photodetector, the signal represents a broad wavelength bandwidth that only excludes the laser wavelength. Also,

the PMT's used in the pyrometry system are much more sensitive than the PDA-55 photodetector used with the bandstop filter.

As expected, the raw signals from the pyrometry system look similar to the signals from the bandstop filtered photodetector. Figure 16 shows the same data from Figure 13, with the 700 nm and 900 nm raw data from the pyrometer added to the plot. The signal from both the 700 nm and 900 nm channels is zero when the laser is first functioned, as referenced to the signal from the 10 MHz unfiltered photodetector. After reaction begins, the 700 nm and 900 nm signals begin to increase. Note that the 700 nm signal begins to increase before the 900 nm signal, while the 900 nm signal begins to increase at about the same time as the bandstop filtered photodetector signal (this is consistent in every experiment). The PMT is much more sensitive near 700 nm, which likely explains why the signal increases first at that wavelength. The plot also suggests that the sensitivity of the PMT at 900 nm is likely similar to the overall sensitivity of the PDA-55 photodetector, which explains why those two signals increase at about the same time. As will be shown in later sections of this report, the signals from the 700 nm channel of the pyrometer proved valuable for providing insight into the ignition phenomenon. Data from the bandstop filtered photodetector, as well as data from the remaining four pyrometry channels will not be presented due to the relatively low sensitivity of the PDA-55 detectors and the problems with the pyrometry system that were outlined above.

6 Discussion of Experimental Results

6.1 Variable Pulse Width Experiments

Variable pulse width experiments were conducted with high power density and small spot size. The goal of these experiments was to establish how much, if any, additional laser energy is needed to promote a self-sustaining reaction in the explosive once reaction begins. These experiments were conducted with the highest possible power density to ensure negligible heat loss due to conduction away from the region of the explosive heated directly by the laser diode. The smallest achievable spot size, 40 μm, was used with the highest laser power setting to achieve a nominal power density of 4.5 MW/cm^2 (this is the nominal power density actually delivered to the explosive). The laser pulse width was set to 3 μs for the first experiment and was decreased until the laser failed to initiate a self-sustaining reaction (defined as a reaction that consumed the ignition increment and DDT increment, and referred to as a "fire") in the explosive.

Figure 17 shows the data from the first experiment, which was conducted with a laser pulse width of 3 μs. The 10 MHz photodetector signal suggests that reaction begins after 190 ns. The 700 nm signal from the pyrometer begins to rise almost immediately, and has a distinct inflection point after about 840 ns, after which the signal strength increases dramatically. Output is detected after 4.24 μs.

The pulse width was shortened first to 2 μs, then to 1 μs, and then to 500 ns. All three of these experiments resulted in a "fire," and the data are shown in Figure 18, Figure 19, and Figure 20. Finally, a pulse width of 250 ns led to a "no-fire." The pulse width was then increased to 400 ns, which also resulted in a no-fire. Next, the experiment at 500 ns was repeated, again resulting in a fire. Finally, two experiments were conducted with a pulse width of 450 ns, with one test resulting in a no-fire and one test resulting in a fire. This suggests a threshold pulse width at or near 450 ns. The data from the two experiments with a 450 ns pulse width are shown in Figure 21 and Figure 22.

The data from the variable pulse width experiments are summarized in Table 7. The time required for the photodetector signal to deviate from the baseline signal averaged 0.28 μs, with a relatively low standard deviation of 0.05 μs.

The data from the 700 nm channel of the pyrometer is slightly more difficult to interpret. In some cases the signal began increasing almost immediately after the laser was functioned, while in other cases the signal appeared to begin to increase at roughly the same time as the signal from the unfiltered photodetector deviated from the baseline signal. In all cases, the signal has an inflection point that separates a shallower slope portion of the signal from a steeper slope portion, although the inflection point is more pronounced in some experiments than others. It is theorized that the initial portion of the signal with the shallower slope is a result of the heating of the carbon black in the ignition increment. Any signal from the 700 nm channel implies that at least a portion of the ignition increment is heated to an extremely high temperature. It is possible that the high power density in the experiment heats the carbon black so quickly that the

temperature increase of the explosive, or at least a portion of the explosive, lags behind the temperature increase of the carbon black. Thus, there is a slight delay before the critical temperature is reached in a substantial enough portion of the explosive, resulting in the subsequent increase in signal strength that results in the steeper slope portion of the curve (this theory will be addressed further in Section 8.2). At any rate, the time required to reach the inflection point, which averages 0.69 μs with a standard deviation of 0.07 μs, is shown in Table 7.

The time to output was extremely consistent for each experiment, with an average time of 4.26 μs and a standard deviation of just 0.09 μs. This implies that the excess laser energy from the experiments with relatively long pulse width does little to accelerate the deflagration process once the ignition increment is initiated, indicating that the energy input from the laser into the reacting explosive is negligible (or ineffective) compared to chemical energy release.

A calculation was performed for each experiment that determined the amount of laser energy required for the unfiltered photodetector signal to deviate from the baseline signal, as well as the energy delivered up to the time where the signal from the 700 nm channel reaches the inflection point. These values are also tabulated in Table 7. An average of 9.7 μJ is required for the unfiltered photodetector signal to deviate from the baseline signal, while an average of 32.5 μJ is required to reach the inflection point on the signal from the 700 nm pyrometer channel. Interestingly, the latter energy is consistent with the energy delivered from the shortest pulse that achieved ignition and sustained reaction (450 ns pulse with 32 μJ of energy). This suggests that once reaction begins, it is possible that the reaction will quench without the additional laser energy required to promote a self-sustaining reaction. At this particular energy delivery rate (i.e., power density), it appears that 32 μJ of energy is required to achieve a self-sustaining reaction.

The variable pulse width experiments revealed that the data from the filtered photodetectors (both the bandpass and bandstop), as well as the 900 nm pyrometer channel give erroneous ignition time and/or self-sustaining ignition times due to the reduced sensitivity of the photodetectors and PMT's. Therefore, these data will not be discussed or referred to in the remainder of the report.

6.2 Nomenclature and Experimental Repeatability and Uncertainty

At this point, it is instructive to discuss nomenclature that will be used for the remainder of the report. Strictly speaking, an explosive is always reacting, and the reaction rate is dependent on the temperature of the explosive. At relatively low temperatures near room temperature, the reaction rate is so low that any heat produced by reactions is dissipated quickly enough to prevent self-heating of the explosive. If the explosive is heated by some external source, there are two sources of energy: the energy from the heating source (in this case a laser), and the chemical energy from the reaction of the explosive. As the temperature of the heating explosive increases, the reaction rate and corresponding rate of chemical energy production increases, until the energy delivery rate from both the chemical reactions and heating source is sufficient to promote thermal runaway within

the explosive. At this point, which will be referred to as "ignition" (abbreviated as subscript "ign"), the explosive is still dependant on the heating source, and the reaction could quench if the heating source is removed. Finally, the reaction progresses to achieve temperatures that allow for a self-sustaining reaction without additional energy from the external heating source. This point will be referred to as "self-sustained ignition" (abbreviated as subscript "ss ign"). For simplicity, the explosive will be referred to as an "unreacted" explosive before ignition, and as a "reacting" explosive after ignition.

Determining when ignition and self-sustained ignition occur has its limitations. Strictly speaking, the signal to the unfiltered photodetector should deviate from the baseline case immediately, since the chemical reactions from the explosive should provide additional energy as soon as the explosive is heated when compared to the non-reactive baseline case (the surface of the energy meter). This additional energy, however, is so small initially that the sensitivity limitations of the photodetector prevent this from being observed. Eventually, the additional energy from the chemical reactions is sufficient to cause the signal to deviate noticeably from the baseline signal. Referring to this point as "ignition" is somewhat arbitrary since it is dependant on the sensitivity of the photodetector and the alignment of the optics; however, the limited insensitivity of the photodetector creates an artificial threshold that therefore requires something significant to occur in the unreacted explosive to cause a noticeable deviation in the photodetector signal. Similarly, the inflection point in the signal from the 700 nm pyrometry channel (which uses a PMT tube with much higher sensitivity than a photodetector) implies that something significant had to happen within the reacting explosive.

The argument in the preceding paragraph underscores the need to obtain strong signals from the photodetector used to determine the time to ignition. In general, the ignition time was determined from the strongest signal from the most sensitive photodetector (10 MHz). Data from the 125 MHz and 1 GHz photodetector were only used if the signal from the 10 MHz detector was saturated or extremely weak. It is notable that when strong signals were obtained from all three photodetectors, the ignition time determined by the 10 MHz signal was slightly shorter than the ignition time determined by the 125 MHz and 1 GHz detectors due to the increased sensitivity of the 10 MHz detector.

Before continuing, it is appropriate to make a few comments regarding experimental repeatability and uncertainty. A detailed error analysis of the experimental method is omitted here, since the multiple potential sources of error and the large differences in power density and spot size between experiments make accurate uncertainty calculations difficult, if not impossible. Instead, the veracity of the results is established based on the repeatability of the experiments, which underscores the need to perform multiple experiments for each test condition. In general, five experiments were conducted at each test condition, and average and standard deviation data are presented along with the individual data. It should be noted, however, that this approach towards accuracy does not exclude the possibility of experimental uncertainty that systematically skews the data in a consistent manner. In most cases, it would be expected that such errors would still allow for relative comparisons and conclusions. Whenever possible, the implications of such errors will be mentioned with the corresponding conclusions.

6.3 Variable Power Density and Laser Spot Size Experiments

Thirty-seven experiments were conducted with various power densities and spot sizes. For the most part, five experiments were conducted for each power density and spot size combination, although only two experiments were conducted with a power density of 0.75 MW/cm^2 and 50 micron spot size due to a shortened supply of 50 micron optics devices. Representative data from each power density and spot size combination will be presented first, starting with the highest power density and moving towards the lowest power density. It should be noted that the laser pulse width was set to 5 μs for all of the experiments discussed in this section. The average data from the variable pulse width experiments are also included in this section, including only the data from the six experiments that resulted in a "fire" (it was established in Section 6.1 that the variable pulse width did not appear to affect the ignition, self-sustained ignition, or output times).

Data from an experiment conducted with a nominal power density of 2.5 MW/cm^2 and 50 micron nominal spot size are shown in Figure 23. Qualitatively, the signals look similar to those from the variable pulse width experiments. The ignition time can readily be obtained from the comparison of the 10 MHz detector signal to the baseline signal, and the 700 nm pyrometer channel shows the now familiar inflection point that denotes the onset of a self-sustaining reaction. For these five experiments, t_{ign} averaged 0.30 μs, while $t_{ss\ ign}$ averaged 0.66 μs. These times are nearly identical to the times obtained in the variable pulse width experiments (conducted with a power density of 4.5 MW/cm^2), suggesting a law of diminishing returns at these extremely high power densities (a possible explanation for this is offered in Section 8.2).

Figure 24 shows data from an experiment conducted with a power density of 1.0 MW/cm^2 and 50 micron spot size. These data are also qualitatively similar to the previously discussed data, although it should be noted that the signal from the 700 nm pyrometer channel did not always exhibit the inflection point seen in Figure 24. In fact, in four out of the five experiments conducted at 1.0 MW/cm^2, there is no initial increase in the 700 nm signal, and the signal simply ramps up quickly later in time, as shown in Figure 25. In Section 6.1, it was suggested that the initial increase in the 700 nm line is caused by high temperature carbon black that heats at a significantly higher rate than that of the neighboring explosive particles. Thus, the data from the experiments at 1.0 MW/cm^2 suggest that this power density is marginal in achieving this phenomenon. Indeed, at all power densities below 1.0 MW/cm^2, the initial increase in the signal from 700 nm pyrometry channel prior to achieving the self-sustaining reaction is not evident. For experiments that did not exhibit this initial increase, the time to self-sustained ignition was taken as the time required for the signal to first increase, as shown in Figure 25. The ignition time and self-sustained ignition time for these experiments averaged 0.53 μs and 1.31 μs, respectively. These times are significantly longer than the times at 2.5 and 4.5 MW/cm^2.

Two sets of experiments were conducted with a power density of 0.75 MW/cm^2, with one set using optics that produced a 50 micron spot size on the explosive, while the other set produced a 100 micron spot size. Representative data from these two sets of experiments are shown in Figure 26 and Figure 27. For the experiments conducted with a 50 micron

spot size, t_{ign} averaged 0.54 μs and $t_{ss\ ign}$ averaged 1.22 μs, while with a 100 micron spot size, t_{ign} averaged 0.44 μs and $t_{ss\ ign}$ averaged 1.10 μs. While the numbers are slightly lower with the larger spot size, these times agree within the uncertainty in the measurements, suggesting that changing from a 50 to 100 micron spot size has little, if any, effect on ignition at this power density.

Representative data from the two sets of experiments conducted with a power density of 0.5 MW/cm^2 are shown in Figure 28 and Figure 29. Figure 28 shows data from an experiment conducted with a 50 micron spot size (note that the signal from the 700 nm pyrometer channel was clipped by the oscilloscope, but the data can still be used as a timing fiducial), while Figure 29 shows the data from an experiment conducted with a 100 micron spot size. With a 50 micron spot size, ignition time averaged 0.68 μs and self-sustained ignition time averaged 1.16 μs, while with a 100 micron spot size, ignition time averaged 0.75 μs and self-sustained ignition time averaged 1.40 μs. Again, these values agree within experimental repeatability and measurement uncertainty, suggesting that changing from a 50 to 100 micron spot size does not appreciably affect ignition at this power density.

The last two sets of experiments were conducted with the minimum power density of 0.2 MW/cm^2, with spot sizes of 100 and 200 microns. Representative data from an experiment conducted with a 100 micron spot size are shown in Figure 30, while representative data from the 200 micron spot size are shown in Figure 31. Unfortunately, ignition time data from the experiments conducted with the 100 micron spot size could not be accurately determined for four out of the five experiments due to the low strength of the photodetector signals at this relatively low power density. For the one experiment where it could be determined, the ignition time was 2.1 μs. The self-sustaining ignition time was evident from the signal from the 700 nm pyrometer channel, and averaged 3.56 μs. For the experiments with a spot size of 200 microns, ignition time averaged 1.98 μs, while self-sustained ignition time averaged 2.13 μs. Interestingly, the ignition times agree within experimental error and measurement uncertainty, but the self-sustaining ignition time is significantly longer for the experiments with 100 micron spot size versus 200 micron spot size. It is likely that this is due to heat losses from conduction away from the ignition region, which is more likely to occur at this relatively low power density of 0.2 kW/cm^2 (this will be addressed further in Section 8.2).

The average data from all experiments is summarized in Table 8. The data from each experiment can be found in Appendix A.

6.4 Output Data

The output time is defined as the time required for the output fiber to detect light, referenced to the time when the laser first begins to irradiate the explosive. In general, the output time decreased as power density increased, as one would expect; however, a careful examination of the timing data reveals another significant trend. When calculating the differences between various times, it was discovered that the time from self-sustained ignition to output was fairly constant, ranging from 3.06 to 3.58 μs. In contrast, the time from ignition to output was not as constant, ranging from 3.34 to 4.52

μs. This, of course, can also be related to the fact that the time from ignition to self-sustained ignition was not as constant, ranging from 0.15 to 1.46 μs. The output timing and differences are summarized in Table 9.

These data provide further evidence that once the explosive reaches self-sustained ignition, the excess energy from the laser does not significantly affect the deflagration process, since higher laser power densities do not reduce the time from self-sustained ignition to output. The time averaged 3.28 μs. Over this time, the reaction progresses through the ignition increment, which is nominally 0.040 inches tall, and the DDT increment, which is nominally 0.080 inches tall (it should be noted that these distances are nominal, not exact, since the two increments were pressed to a pressure, not a stop). Although average velocity could be calculated from these data, the calculated velocity would be nearly meaningless, since the velocity of the reaction front is actually exponentially increasing from nearly zero at ignition through two materials with different DDT rates.

7 Modeling and Analysis

A modeling effort was undertaken to better understand the data recorded during the LDI experiments described in Sections 6.1 and 6.3. This modeling effort is fairly simple in nature since the goal was to better understand the data and not to attempt a complete explanation of the underlying phenomenon. Future modeling work, if attempted, may accomplish this goal.

The modeling effort will be described in five sections. The first section covers the basic heat transfer analysis and assumptions used in this work. The second section describes how the temporal aspects of the heat flux are handled and the third section describes how the spatial nature of the heat flux is handled. The fourth section addresses material properties, and the last section summarizes the findings here in a manner in which they can be compared with timing data.

7.1 Fundamentals

To begin the analysis of the LDI problem, it is first assumed that the laser-material interaction is purely thermal in nature. In other words, it is assumed that there is no ablative-like behavior taking place, and the laser pulse does not create a shock in the BNCP IP. This assumption follows that of previous researchers.[13-15, 20]

The assumption of a purely thermal interaction means that a standard heat transfer approach can be taken. The governing equation is the three-dimensional, time-dependent heat diffusion equation,

$$\nabla\left(k\,\nabla T\right)+\dot{q}=\rho c_{p}\,\frac{\partial T}{\partial t}\,, \qquad \textbf{(1)}$$

where k is the material thermal conductivity, ρ is the IP density and c_p is the specific heat. Previous researchers[13-15, 20] have started here and generated results by expanding this equation into a finite-difference or finite-element equation that was then solved using standard numerical methods. Although a similar approach could be taken here, we instead chose to simplify the equation using reasonable assumptions. These simplifications yield an equation that can be solved analytically.

In previous modeling work, the laser pulses used to heat the material to its critical temperature covered the range from 5 μs to 10 ms. In our work, the longest pulse used was 5 μs, and most test data show initiation in less than ~2.5 μs. The shorter and narrower range of ignition times brings forth the question as to whether the complete three-dimensional, time-dependent heat diffusion equation is needed. In particular, at these short times, it is possible that the heat generation term is large enough to make the divergence of the heat flux vector term negligible (i.e. conduction effects can be ignored). Previous work[20] has indicated that this may be the case.

A simple way of offering a heuristic answer to the question of whether or not conduction effects are negligible is to look at the infinite slab problem as shown in Figure 32. In this problem, the surface of the infinite slab is instantaneously brought to a high temperature. The temperature profile in the slab is then calculated at later times to determine the rate at which the thermal energy propagates into the slab. If the temperature in the slab increases by a negligible amount in 5 μs, it can be assumed that the material not directly heated by the laser pulse is not affected by the laser pulse. Conduction effects would therefore be negligible.

To begin, we use the equation for the temperature, T, as a function of depth, x, into the slab at time, t. This equation is derived in any standard heat transfer textbook and is given by

$$\frac{T(x,t)-T_s}{T_i-T_s} = erf\left(\frac{x}{2\sqrt{\alpha t}}\right), \qquad \textbf{(2)}$$

where T_s is the surface temperature, T_i is the initial slab temperature, and α is the thermal diffusivity. Next, the material properties of the HE column are listed. Here, it is assumed that the 1.0% mass of carbon black added to the HE does not significantly change the thermal properties of BNCP. It is also assumed that the material behaves as a homogeneous solid so that crystal boundary effects can be ignored. The density of the detonator IP is 1.7 g/cm^3, and the heat capacity is 1.07 J/g-K. Thermal conductivity data for the IP material was not available, so the value of 362 W/cm-s-K for CP was taken from the research of Glass et al.[15] Since CP is similar in chemistry to BNCP, it is assumed that thermal conductivity is also similar at comparable densities. Using these properties, Eq. (2) is plotted in Figure 33. As this figure shows, for a large temperature difference (T_s = 300ºC, T_i = 25ºC) and for the longest duration of laser pulse (5 μs), the effects of the surface temperature rise were negligible after ~4 μm into the slab.

This 4 μm distance result along with several important aspects of the experimental setup indicated that thermal conduction could be neglected in this problem. BNCP ignites at lower temperatures (250-280ºC, based on differential scanning calorimetry experiments) than that used in the infinite slab example, so the actual maximum possible temperature difference in the HE material should be much lower than that of the proposed infinite slab problem. Also, as will be shown later, the spatial distribution of the laser energy in the IP column was expected to be smooth with very small spatial discontinuities (i.e. the IP is not heated in a manner that will create large localized temperature gradients). These two facts indicated that the local temperature gradient in the IP would be much less than at the surface of the infinite slab problem. Furthermore, as the data from the experiments show, the ignition times were normally less than ~2.5 μs, thus further reducing the thermal energy penetration depth before ignition. Finally, in the present experiments the laser spot sizes ranged from 40 μm to 200 μm. Even if thermal conduction effects would expand the heated region of the IP by a micron, this would lead to a marginal increase in the volume heated to near critical temperature by the laser. Taking all of these facts into

account, the conduction terms of the heat diffusion equation can be ignored and the governing equation can now be written as

$$\dot{q} = \rho c_p \frac{\partial T}{\partial t}. \tag{3}$$

If a simple form of $\dot{q}(x, y, z, t)$ is chosen, a closed form analytical solution to this problem is easily calculated.

This conclusion greatly simplifies the analysis of this problem in that the spatial and temporal deposition of thermal energy are decoupled (i.e. the spatial distribution of thermal energy is not dependent on time). Mathematically, $\dot{q}(x, y, z, t)$ can be written as the product of a spatial energy distribution, $\dot{q}_s(x, y, z)$, and a time dependent modulation function, $\dot{q}_t(t)$, or

$$\dot{q}(x, y, z, t) = \dot{q}_s(x, y, z)\, \dot{q}_t(t). \tag{4}$$

This decoupling means that once the spatial distribution of laser energy is calculated, then each point in space can be marched forward in time without accounting for interactions of the surrounding material.

7.2 Derivation of the time dependent modulation function

The time dependent modulation function was based on a rough approximation of the intensity-time profile of the laser pulse. Figure 34 shows a trace measuring the normalized output of the laser as measured during a no-fire test. This trace suggests a simple equation of the form

$$\dot{q}_t(t) = \begin{cases} t \big/ t_{rise} & 0 \le t < t_{rise} \\ 1 & t_{rise} < t \end{cases}, \tag{5}$$

where t_{rise} is the rise time of the laser pulse. Equation (5) is also plotted in Figure 34. Although Eq. (5) does not exactly follow the output trace of the laser, it is a good approximation that can be improved upon in future work, if needed.

Using Eqs. (3), (4), and (5), an equation relating the temperature in the IP as a function of time and spatial energy distribution is

$$T(x, y, z, t) = \begin{cases} \dfrac{\dot{q}_s(x, y, z)}{2\rho c_p} \dfrac{t^2}{t_{rise}} + T_0 & 0 \le t < t_{rise} \\ \dfrac{\dot{q}_s(x, y, z)}{\rho c_p} \left(t - \dfrac{1}{2} t_{rise} \right) + T_0 & t_{rise} < t \end{cases}, \tag{6}$$

where T_0 is the initial temperature of the HE IP. Now, all that is remaining is the derivation of the spatial energy distribution function, $\dot{q}_s(x, y, z)$.

7.3 Derivation of the spatial energy distribution function

The spatial energy distribution function, $\dot{q}_s(x, y, z)$, describes how the laser energy is deposited within the IP column. A true and accurate description of energy distribution in the IP column is a very difficult task. As well as being a function of position (x, y, z), $\dot{q}_s$ is also a function of BNCP crystal size distribution, BNCP crystal morphology, BNCP crystal optical properties, mass of carbon black added, optical properties of the carbon black, coating efficiency of carbon black onto the BNCP crystals, IP column density, optics delivering the laser power, etc. A complete description of the absorption and scattering effects within this heterogeneous material would be extremely difficult and would most likely contain sizable errors. In fact, such packed bed scattering problems are usually "solved" using gross approximations. In addition, the optical properties of BNCP are not completely known, and previous work[20] has shown that the optical properties of a pressed HE pellet can be fairly difficult to measure experimentally. For this reason, we will start with a simple one-dimensional approach. Later, a three dimensional numerical model will be developed to determine the applicability of the one-dimensional model to the experimental data.

The simplest approach for the spatial energy distribution function is to assume the laser energy reaches the surface as a collimated beam of light with a "top-hat" profile. The light intensity then decays exponentially with depth into the IP column with no scattering (i.e. the column acts as a homogeneous solid with constant optical properties and no voids). Experimentally, the input energy per unit surface area (or heat flux, q_0'') is measured at the surface of the IP. This input energy is reduced by the reflectivity of the IP front surface so that the actual amount of energy entering into the IP pellet at the surface ($x = 0$) is $\alpha q_0''$, where α is the bulk absorptivity ($\alpha = 1 -$ reflectivity) of the IP surface. If the intensity decays exponentially with distance, the heat flux through an imaginary plane at position x in the IP column can be written as

$$q'' = \alpha q_0'' \exp[-\beta x], \tag{7}$$

where β is the extinction coefficient of the IP column. The spatial energy distribution function can then be found by

$$\dot{q}_s(x) = -\frac{dq''}{dx} = \alpha\beta q_0'' \exp[-\beta x], \tag{8}$$

where the negative sign is to ensure the *positive* direction of energy *into* the IP column. Substituting this into Eq. (6) gives the temperature distribution in the IP as a function of distance into the pellet and time or

$$T(x,t)=\begin{cases}\dfrac{\alpha\beta q_0''\exp[-\beta x]}{2\rho c_p}\dfrac{t^2}{t_{rise}}+T_0 & 0\le t<t_{rise}\\ \dfrac{\alpha\beta q_0''\exp[-\beta x]}{\rho c_p}\left(t-\dfrac{1}{2}t_{rise}\right)+T_0 & t_{rise}<t\end{cases}. \qquad \textbf{(9)}$$

Once the necessary optical properties, α and β, are measured, it is possible to calculate the temperature profile of the IP column during a laser pulse.

Even though this one-dimensional model is useful in the analysis of the experimental data, it completely eliminates any information related to laser irradiation spot size, one of the important parameters varied in the experiments. One approach to remedying this shortfall is to apply the 1-D model to a spot-sized area of the IP pellet in a kind of "pseudo-3-D" approach. In this manner, the temperature profile of the IP column can now be written as

$$T(r,z,t)=\begin{cases}\dfrac{\alpha\beta q_0''\exp[-\beta z]}{2\rho c_p}\dfrac{t^2}{t_{rise}}+T_0 & 0\le t<t_{rise} \quad r<r_{spot}\\ \dfrac{\alpha\beta q_0''\exp[-\beta z]}{\rho c_p}\left(t-\dfrac{1}{2}t_{rise}\right)+T_0 & t_{rise}<t \quad r<r_{xpot}\\ 0 & 0\le t \quad r>r_{spot}\end{cases}, \qquad \textbf{(10)}$$

where cylindrical coordinates are used for simplicity. Although this is now a three-dimensional model, nothing is really gained in terms of understanding how the laser energy couples into the IP column. A second, more informative, approach is to attempt a modeling of the laser focusing optics and scattering effects.

The first step in a three-dimensional model is to describe how the laser light impinges onto the IP front surface. This involves examining the properties of the fiber optic supplying the laser energy as well as the lenses that focus the light down to a spot size. Figure 35 depicts a conceptual drawing of the detonator showing all relevant components.

Fiber optics have the unique property of emitting (and accepting) radiation into a limited range of angles from the end of the fiber. This angle, θ_f, is related to the numerical aperture of the fiber, N.A., by

$$N.A.=\sin\theta_f. \qquad \textbf{(11)}$$

Because the fiber emits light into a limited range of angles, the light reaching the BNCP IP has a limited range of angles of incidence. The principle of invariance of optical extent[24] is used to calculate the maximum angle of incidence at the IP surface, θ_s. This principle states that for any two locations in a non-absorbing optical path,

$$n_1^2 dA_{1,n} d\varpi_1 = n_2^2 dA_{2,n} d\varpi_2, \quad \textbf{(12)}$$

where n_1 and n_2 are the indices of refraction for locations 1 and 2, $dA_{1,n}$ and $dA_{2,n}$ are the differential normal areas of the "beam" at locations 1 and 2, and $d\omega_1$ and $d\omega_2$ are the differential solid angles of the beam at locations 1 and 2. If location 1 is selected to be the air-side surface at the output of the fiber and location 2 is selected to be the sapphire window-side of the window-IP interface, then

$$dA_{f,n} d\varpi_f = n_s^2 dA_{s,n} d\varpi_s. \quad \textbf{(13)}$$

Here, *f* notes the area and solid angle at the fiber and *s* notes the index of refraction, spot size area, and solid angle at the window-IP interface. Integrating both sides over the area of the beam and solid angles of the beam,

$$\int_{\Omega}\int_{A} dA_{f,n} d\varpi_f = n_s^2 \int_{\Omega}\int_{A} dA_{s,n} d\varpi_s. \quad \textbf{(14)}$$

Expanding the integrals over solid angle gives

$$\int_0^{2\pi} d\phi \int_0^{\theta_f} \cos\theta \sin\theta \, d\theta \int_{A_{fiber}} dA_f = n_s^2 \int_0^{2\pi} d\phi \int_0^{\theta_s} \cos\theta \sin\theta \, d\theta \int_{A_{spot}} dA_f. \quad \textbf{(15)}$$

Solving these integrals, dividing out similar terms, and noting that $\sin\theta_s = N.A.$ gives

$$(N.A.)^2 r_f^2 = n_s^2 \sin\theta_s r_{spot}^2 \quad \textbf{(16)}$$

so that

$$\sin\theta_s^{\max} = \frac{N.A.}{n_s} \frac{d_f}{d_s}. \quad \textbf{(17)}$$

In these equations d_f and d_s are the fiber and spot diameters, respectively. This relationship now gives the largest angle of incidence possible at the window-IP interface given the index of refraction of the window, the numerical aperture of the fiber, and the fiber and spot size radii. This maximum angle is independent of the intervening optics (assuming the optics are not designed to create a limiting aperture).

In past work attempting a three-dimensional description of laser energy deposition,[15] the effects of this limited angle of incidence were neglected and it was assumed that the laser energy was evenly deposited within a frustum as shown in Figure 36. Other work[13, 14, 20] assumed that three-dimensional effects were negligible and used a one-dimensional approximation similar to Eqs. (9) and (10). Here, it is intended to outline and

demonstrate a method to account for the three-dimensional distribution of laser energy in the LDI IP.

When the limited angle of incidence is considered, the three-dimensional deposition of energy within the IP is much more complicated as shown in Figure 37. Simple inspection shows that there are three regions with different energy deposition rates. In region I, shown in Figure 38a, each point receives the maximum amount of light obtainable at that depth. In regions II and III, shown in Figure 38b and Figure 38c, respectively, each point receives less than the maximum amount of light. The farther a point is from region I, the less light it will receive at a given depth. It is also expected that a solution to the problem will be smooth across all three regions, and that the solution will show the exponential decay behavior seen in the one-dimensional model. A direct analytical calculation of the energy deposition at a given location involves solving complex integral equations. As was noted in the beginning of this section, these equations involve many of the material properties and crystal morphologies of both BNCP and carbon black, most of which have not been measured. In addition, even if the IP column is assumed to be a homogeneous solid with no voids, these equations may still be intractable due to the complex geometric relations involved.

An alternative numerical approach to find the energy deposition throughout the solid is to use the Monte Carlo method. This statistical method, which is well documented in standard radiation heat transfer textbooks and the literature,[30-32] can solve the homogeneous material case and can be expanded to handle complex scattering behavior if and when optical material properties become available. In principle, the Monte Carlo method involves sending out a large number of "energy bundles" from the light source. The direction and propagation properties of each of these bundles are determined by probability distribution functions (PDF's) that are formed to represent the experiment at hand. These PDF's are then integrated to arrive at the cumulative distribution functions (CDF's). A CDF is simply a relation between a random number and a property of the bundle (e.g. emission location, emission direction, depth of penetration, etc.). The behavior of all the bundles are tallied and then averaged to determine the desired model data (in this case, the energy deposition rate, $\dot{q}_s(z,r,\theta)$, is of interest). The full derivation of PDF's and their corresponding CDF's are developed in standard radiation heat transfer textbooks, so they will not be given here. Instead, only the CDF's are given. In this analysis, it is again assumed that the BNCP/carbon black mixture is a homogeneous solid with constant optical properties and no scattering. Based on the infinite slab problem results, it is also assumed that the IP column behaves as a cold medium (i.e. there is no re-radiating of heat energy within the IP column). Although these assumptions may not be accurate, the results of this simple model prove to be very informative.

The Monte Carlo code used in this work is shown in block form in Figure 39. The FORTRAN code used is listed in Appendix B. First a random number generator[33] is used along with the CDF's to determine the starting position and direction of each energy bundle. The position of the starting point of each bundle is determined by

$$r = r_s \sqrt{R} \tag{18}$$

and

$$\sin\theta = \sqrt{R}\,, \tag{19}$$

where r and θ are the polar coordinates from an origin located at the center of the laser spot, r_s is the spot radius, and R is a random number ranging from 0 to 1. The direction cosines of the bundle emitted from the starting point can be calculated from the polar (θ) and azimuthal (ϕ) angles given by

$$\sin\theta = \sqrt{R}\sin\theta_s \tag{20}$$

and

$$\phi = 2\pi R\,. \tag{21}$$

These four equations yield the starting point and direction for each bundle. The next step is to determine if the bundle is reflected or absorbed by the IP surface. This is done simply by comparing a random number, R, to the surface absorptivity, α. If $R < \alpha$, the bundle is absorbed (i.e. allowed to propagate into the material and allowed to be tallied with results), and if $R > \alpha$, the bundle is reflected (i.e. the bundle is not propagated and tallied). Next, the length of penetration (L) of each bundle into the IP at its given direction is given by

$$L = -\frac{1}{K}\ln R\,, \tag{22}$$

where K is the extinction coefficient of the IP material. This then results in an ending position (z, r, θ) for each emitted bundle. To simplify the recording of the ending location of each bundle, the IP column is split into small annular volumes given by

$$Vol_{i,j} = \left(z_{i+1} - z_i\right)\pi\left(r_{j+1}^2 - r_j^2\right), \tag{23}$$

where $\Delta z = z_{i+1}$-z_i and the distances between r_{j+1} and r_j are chosen to acceptably resolve the IP volume. By binning each of the ending locations, the three-dimensional output data is reduced into a two-dimensional axisymmetric output. This greatly simplifies the post-processing of the data and reduces the memory load of the code. In addition, this assumption of an axisymmetric problem has the added benefits of reducing statistical noise and increasing the speed of convergence by effectively averaging the results.

The last element of the Monte Carlo approach described here is the assignment of an energy value to each bundle. As was noted above, the laser flux on the surface is

measured, and so it is useful to use this value in assigning an energy value to each bundle. The total power, Q, delivered to the IP front surface is given by

$$Q = q_0'' A_s, \tag{24}$$

where q_0'' is the surface power density and A_s is the area of the laser spot. Therefore the power per each bundle, q_B, is given by

$$q_B = \frac{Q}{N}, \tag{25}$$

where N is the total number of bundles emitted. The output data are thus converted to a two-dimensional axisymmetric spatial energy distribution function, $\dot{q}_s(z,r)$, by noting that

$$q_B \frac{n_{B,i,j}}{Vol_{i,j}} = \frac{Q}{N}\frac{n_{B,i,j}}{Vol_{i,j}} = q_0'' \frac{A_s}{N}\frac{n_{B,i,j}}{Vol_{i,j}} = \dot{q}_s(z_i, r_j). \tag{26}$$

Here, $n_{B,i,j}$ is the number of bundles stopped in a given annular volume, $Vol_{i,j}$. The output of the Monte Carlo code is an ASCII text file that holds both the input parameters and a r vs. z vs. $\dot{q}_s$ matrix, which can easily be read into a standard plotting software package. One interesting property of the Monte Carlo analysis is that the output function $\dot{q}_s(z,r)$ is readily scalable to different power levels by multiplying the $\dot{q}_s(z,r)$ matrix by

$$\frac{q_{0,2}''}{q_{0,1}''}, \tag{27}$$

where $q_{0,1}'' = q_0''$ is the value initially used in the code and $q_{0,2}''$ is a different power level. This, of course, assumes that all other parameters (spot size, fiber properties, etc) are held constant. In this way, a nominal result can be used to analyze a number of different input power levels.

In order to confirm that the code works from a theoretical and implementation standpoint, the simplified "pseudo-3-D" case is run and compared with the results of Eq. (10). In this case, the direction of propagation for each bundle is set perpendicular to the IP front surface so that the unit vector points in the positive z direction. The material properties used in this case are summarized in Table 10.

The code was run to track the progress of 1×10^7 bundles. The output of the code in Watts/μm^3 is shown in Figure 40. By plugging each z_i, r_j point into Eq. (6) and moving forward in time, it is possible to calculate how the IP heats with time as shown in Figure 41. To compare the code with the pseudo-3-D solution, the temperature trace as a function of time for various distances into the IP is plotted in Figure 42. As this plot

shows, the code closely matches the analytical result. It is now possible to apply the code to the real problem to obtain an estimate of the energy deposition in the IP. Before that can be done, however, the material properties input into the code must be specified.

7.4 Material Properties

To obtain an estimate of the laser energy deposition in the IP, it is necessary to quantify the relevant optical material properties to be entered into the code. In particular, it is necessary to determine the IP surface absorptivity, α; the IP extinction coefficient, β; the delivery fiber numerical aperture, *N.A.*; the delivery fiber diameter, d_f; the spot size diameter, d_s; and the index of refraction of the sapphire window, n_s. The fiber-related parameters, *N.A.* and d_f , are specified by the manufacturer. The spot size, d_s, is determined by the design and assembly of the lenses in the detonator, and the actual value of d_s for the manufactured detonator is measured as described in Section 4. The value of n_s for sapphire can be found in several places (literature, manufacturer's data, etc). The value used here is $n_s = 1.76$. Each of these parameters are different from α and β in that they only affect the maximum angle of incidence, θ_s, as was shown in Eq. (17). θ_s only affects the rate at which the input energy spreads out radially, and so small errors in the estimates of these parameters are expected to have a minimal effect on the general form of the spatial energy distribution function, $\dot{q}_s(z,r)$. In contrast, α and β will directly affect how the laser energy penetrates into the IP.

The value of α, the surface absorptivity, is roughly estimated at 0.8 for the detonator design used here. The actual value of α could be measured experimentally, but is not done here. In general, it is not critical to accurately characterize absorptivity because the main effect of a change in α is a scaling of q_0''. As was noted above, the output of the Monte Carlo code is scaleable if all other parameters are held constant. Thus, the general form of $\dot{q}_s(z,r)$ will not be affected. If at a later date the value of α is known with more certainty, the results found here can be re-scaled accordingly.

The final parameter to be determined is the extinction coefficient, β. In radiation heat transfer, β is the sum of two components: the scattering coefficient, σ_s, and the absorption coefficient, σ_a. Both of these parameters have units of 1/length and can be thought of as a measure of how far light travels into a material before being absorbed or scattered into other directions. In order to implement both absorption and scattering into any model (including the present case), values for both σ_s and σ_a are needed along with an estimate of the scattering phase function, which is a measure of the preferential direction of scattering (see Brewster, Siegel and Howel, and Bohren for the details of radiation heat transfer in an absorbing and scattering medium).[30-32] As was shown in Eq. (8), the effects of β on the spatial energy distribution function can be exponential in nature. This implies that changes in β can lead to large changes in energy distribution within the IP column. Thus, it is important to obtain an accurate estimate of β to properly model the IP column. Unfortunately, σ_s and σ_a as well as β are very difficult to measure for any packed bed of particles.[34] In addition, β is not constrained to a narrow range of values. For example, aluminum has a single-crystal absorption coefficient at 808 nm of 1.3×10^6 cm^{-1}, where

for silicon, σ_a = 1x10^3 cm^{-1}.[35] The scattering coefficient can also vary by orders of magnitude depending on crystal size, morphology, material index of refraction, packing density, etc.

In the LDI literature, there are very little data on measured values of β for carbon black-doped explosives. In addition, there are no data available for the BNCP used here. Because of the difficulty in measurement of β for this material, an independent measurement of β was beyond the scope of this work. Instead, the values presented in previous work are used. In the paper by Skocypec et al.,[20] the extinction coefficient of a 0.8% carbon black-doped CP column having a density of 1.5-1.6 g/cm^3 was measured to be 128 cm^{-1}. Later, in a paper by Glass et. al.,[15] this value was updated to 290 cm^{-1}. Although the material in this work is different both in carbon black mass percentage and in base material, this value for CP is likely a good starting estimate of the extinction coefficient of IP material.

Using the parameter values listed in Table 11, sample cases were run using the Monte Carlo code. The resulting energy distribution function and the corresponding temperature profile are shown in Figure 43 and Figure 44. In Figure 45, Figure 43 is enlarged to show the three regions as described above. Here is it seen that the area receiving the largest energy per unit volume is in region I. It would be expected that the ignition point of the LDI detonator would occur here. Within region I, the laser energy appears to decrease at an exponential rate, as was seen in the one-dimensional approximation described in Eq. (8). Figure 46 shows a comparison between the one-dimensional approximation and the Monte-Carlo solution along the centerline of the IP.

This result brings forth two important conclusions. First, the one-dimensional assumption made by previous researchers is accurate, as long as the IP is only considered in region I, or under the condition that

$$r < r_s - z \tan \theta_s \,. \qquad \textbf{(28)}$$

Second, since the energy is concentrated in region I and, in particular, the first few microns of the IP column, it is expected that initiation of the IP will occur in this region. This implies that the one-dimensional case described by Eq. (8) and (9) is all that is needed to describe the thermal initiation behavior of the IP pellet. Of course, this statement is true only if all the above assumptions are valid.

7.5 Conclusions from 1-D analysis

Now that it has been established that a one-dimensional approach is applicable if the IP ignites close to the laser irradiated surface, some simple conclusions can be drawn that will be important later during the analysis of the experimental data. First, if it is assumed that ignition occurs at a constant distance from the surface, Eq (9) can be rewritten as

$$T - T_0 = \begin{cases} Cq_0''t^2 & 0 \le t < t_{rise} \\ (2Ct_{rise})q_0''\left(t - \frac{t_{rise}}{2}\right) & t_{rise} < t \end{cases}, \quad \textbf{(29)}$$

where the constant C is

$$C = \frac{\alpha\beta \exp[-\beta x]}{2\rho c_p t_{rise}}. \quad \textbf{(30)}$$

This form is useful because all of the unknown material properties have been lumped together creating a single term that is affected by material properties. This equation can now be written in a linear form by calculating the natural log of both sides:

$$\begin{aligned} \ln(t) &= -\frac{1}{2}\ln(q_0'') + \frac{1}{2}\ln\left(\frac{T - T_0}{C}\right) \quad 0 \le t < t_{rise} \\ \ln\left(t - \frac{t_{rise}}{2}\right) &= -\ln(q_0'') + \ln\left(\frac{T - T_0}{2Ct_{rise}}\right) \quad t_{rise} < t \end{aligned}. \quad \textbf{(31)}$$

This equation is extremely useful in answering one of the prevailing questions of this work. If it is assumed that the IP will react when the material reaches a critical temperature, T, and that temperature does not change with respect to spot size or power density, then the slope of the time vs. q_0'' data should be a straight line with a slope of -1/2 for $t < t_{rise}$ or a slope of -1 for $t > t_{rise}$. The unknown material properties are lumped together into the intercept term and will not affect the slope. If the data have a slope that is significantly different from the predictions, or if the slope changes as a function of power density, then there is clear evidence that one or more of the assumptions made above is not valid. Namely, this would indicate that the material may not be behaving as a homogeneous solid, the critical temperature may not be independent of spot size or power density, the material properties may not be independent of power density, or possibly a combination of these causes. In this manner, the timing data alone can indicate whether the IP is undergoing thermal ignition during laser irradiance. If a measurement of the surface temperature of the IP during laser radiation was also available, the nature of the departure from strict thermal ignition could also be revealed.

8 Discussion of the Experimental Data with Insight from the Computational Data

8.1 Ignition Timing Data and the 1-D Model

In Section 7.4, it was revealed that a one-dimensional approach is sufficient to describe the processes of LDI under a number of simple assumptions. The basic assumptions were a purely thermal ignition phenomena (where once a critical temperature is reached, the IP ignites), that the material behaves as a homogeneous material, and that the material properties of the IP are independent of power density. The results of that section showed that if these assumptions held, a comparison of Eq (31) and timing data should show a similar slope with differences in intercept being explained as errors in assumed material properties. In particular, Eq (31) showed that if the time of ignition was larger than the rise time of the laser pulse, a plot of timing and power density data should have a slope of -1. If the time of ignition was shorter than the rise time of the laser pulse, the slope should be -1/2. In Figure 47, the average ignition times at each power level recorded by the 700 nm channel are plotted along with a line of slope -1 passing through the first two data points. A slope of -1 is chosen since all the ignition times recorded with the 700 nm channel are larger than the assumed rise time of 0.4 μs. This plot shows that at lower power densities, the ignition of the IP is most likely a purely thermal process. At higher power densities, it is obvious that the experimental data no longer follows a -1 slope. Although changing material properties can shift the analytical curve vertically, the slope will not change if the ignition of the IP is assumed to be purely thermal.

In Figure 48 and Figure 49, the average ignition times at each power level recorded by comparing the 10 MHz detectors with baseline no-fire signals are plotted along with lines of slopes -1 and -1/2 respectively. The data from this timing method show results contradictory to the 700 nm data analysis results. In Figure 48, data are plotted in the form of $\ln(t_{ign}-t_{rise}/2)$ vs. $\ln(q_0'')$. Here, we see that when the measured t is greater than t_{rise}, the data follow a line with slope of -1, but not as clearly as for the 700 nm channel data. Also, for measured t less than t_{rise}, the data follow the -1 slope much closer than that for the 700 nm channel. In Figure 49, data are plotted in the form of $\ln(t_{ign})$ vs. $\ln(q_0'')$. Here we see that when the measured t is greater than t_{rise}, the data do not follow a -1/2 slope as expected, particularly at lower power levels. At higher power levels where the measured t is less than t_{rise}, the data seem to follow a -1/2 slope, but with only two data points, this can not be stated with certainty.

8.2 Energy Calculations

Another method for analyzing and comparing the data involves calculating the energy required for ignition and self-sustained ignition; however, a few cautions should be noted before these data are presented. First, it is important to note that the energy required for initiation can be misleading in several applications, because in many cases, the energy required depends on the energy delivery rate, or power. For example, at very low powers, an infinite amount of energy can be delivered to the explosive without initiation. In contrast, as power is increased, the energy required for initiation begins to decrease,

depending on how much energy is "wasted" by conduction away from the ignition region. Finally, if the power is sufficiently high, one would expect the energy required for initiation to be constant, since the explosive is initiated on time scales which are fast enough to preclude significant heat conduction away from the ignition region. It is expected that the laser power used in the present experiments are high enough for this to be the case.

A second caution regarding energy calculations is related to the geometry of the heating problem. It should be expected that the same amount of power and/or energy delivered to a smaller area would heat the smaller area more quickly. This is especially important when comparing the results of experiments that use different laser spot sizes. Thus, it is more instructive to calculate the power per unit area, or power density, and energy per unit area, or energy density, for each experiment. Ideally, the energy density required for ignition would be constant over a large range of power densities and spot sizes, assuming the power density is large enough to preclude significant heat conduction away from the ignition region, small enough to avoid ablation of the surface of the explosive, and spot size is large enough to preclude problems associated with a critical mass of the explosive that must be heated to the critical temperature before ignition can occur. Of course, it is exactly these types of discrepancies which this research is hoping to uncover. Thus, it is especially instructive to look for discrepancies in the energy density required for ignition, and to attempt to relate these discrepancies to effects from spot size (i.e., scale), power density (i.e., heating rate), and other factors, if appropriate.

Finally, it should be noted that the power density and energy density are not delivered to the explosive in a temporally uniform manner. Ideally, the power, and therefore energy, would be delivered to the explosive in the form of a perfect square wave; unfortunately, practical limitations impose a rise time and fall time that comprise a significant portion of the ignition time. While it is convenient to refer to the nominal power densities when comparing experiments, it is important to realize that significant time is required to reach this nominal power density. Fortunately, the experimental method outlined in Section 4 allows for the straightforward calculation of the energy required for ignition. This method uses an experimental measurement of laser energy and accounts for the exact shape of the laser energy pulse delivered to the explosive.

The energy required to produce ignition and self sustained ignition for each experiment was calculated using the method discussed in Section 4. The energy was then normalized by dividing by the area associated with the spot size of the optics device used in the experiment, producing an energy density that is most conveniently represented in units of nanowatts per square micron, or $nW/\mu m^2$.

The energy calculations are summarized in Table 12. The data indicate that at the power densities ranging from 0.2 to 2.5 MW/cm^2, the ignition energy density is fairly constant, ranging from 2.4 to 4.3 $nW/\mu m^2$. At the power density 4.5 MW/cm^2, the ignition energy density is significantly higher at 9.7 $nJ/\mu m^2$. The self-sustained ignition energy density data tell a slightly different story. For the power density ranging from 0.2 to 0.75 MW/cm^2, the self-sustained ignition energy density is fairly constant, ranging from 5.1-

7.4 nJ/μm^2, with an exception for the experiments conducted at 0.2 MW/cm^2 with 200 micron spot size, which produced an unusually low energy density of 3.8 nJ/μm^2. At the higher power densities of 1.0 to 4.5 MW/cm^2, the self-sustained ignition energy density consistently increases, from 11.2 nJ/μm^2 at 1.0 MW/cm^2, to 12.7 nJ/μm^2 at 2.5 MW/cm^2, to 32.5 nJ/μm^2 at 4.5 MW/cm^2.

The exceptionally low self-sustained ignition energy density for the experiments conducted with a 0.2 MW/cm^2 power density and 200 micron spot size is difficult to explain. As mentioned, the ignition energy density is consistent with the other experiments conducted with power densities ranging from 0.2 to 2.5 MW/cm^2. Initially, it was suspected that the lower self-sustained ignition energy was simply the result of stronger signals that reached the 700 nm channel of the pyrometer from the 200 micron spot size, the largest spot size examined; however, comparisons of the average output time of the 200 micron spot size (t_{out} = 5.32 μs) versus the 100 micron spot size (t_{out} = 6.62 μs) at 0.2 MW/cm^2 also suggest that there is a significant discrepancy between these two spot sizes. It appears that the increased spot size served to reduce the critical temperature, but not enough data were acquired to make a definitive conclusion. Alternatively, it is possible that the experiments were affected by conduction away from the ignition region, since 0.2 MW/cm^2 is the lowest power density examined. In future experiments with more advanced semiconductor technology, it may be advantageous to investigate this further at higher power densities (the 0.2 MW/cm^2 power density is the highest achievable power density with current semiconductor technology and a 200 micron spot size).

Initially, the significant increase in the self-sustained ignition energy density at high power densities may appear to suggest that the critical temperature is significantly higher at higher heating rates. This, however, is likely not the case. The effect is more likely explained by a breakdown in one of the key assumptions mentioned in Section 7. Two of the key assumptions were that the heating of the explosive is purely thermal (i.e., no ablative-like behavior) and that the heated material is homogeneous. The increasing self-sustained ignition energy density at high power density can easily be explained if either or both of these assumptions do not apply. Even at the highest power density of 4.5 MW/cm^2, it is unlikely that the power density is sufficient to ablate the surface of the explosive, as ablation is usually assumed to require power densities on the order of 1 GW/cm^2or higher. It is more likely, then, that at high power densities, the explosive mixture can not be treated as homogeneous.

It is important to note that the ignition increment contains a mixture of carbon black and BNCP. Simplistically, the carbon black can be thought of as an absorbing medium while the BNCP can be thought of as a non-absorbing medium. This implies that the carbon black particles heat when irradiated by the laser, and then transfer that heat to the explosive particles. If the rate of heat transfer from the carbon black to the explosive is approximately consistent with the rate of heating from the laser, then the material can practically be treated as homogeneous. At high laser power densities, however, it should be expected that the carbon black could heat at a rate much higher than the rate of heat

transfer from the carbon black to the explosive. In this case, the average temperature of the explosive would lag significantly behind the average temperature of the carbon black.

It is likely that this phenomenon explains why the ignition and self-sustained ignition energy density tend to increase at relatively high power density. The higher energy is likely the result of the energy that is "wasted" by heating the carbon black to temperatures that far exceed those necessary for ignition. In fact, it is possible, and even probable that the carbon black is vaporized by the laser (carbon black does not melt at atmospheric pressures; instead it sublimes at high temperatures). If this is the case, excess laser energy could be causing an increase in the rate of this phase change instead of a temperature increase of the carbon black.

Simple energy calculations (using the equation $E = mC\Delta T$, with rough approximations of laser penetration depth and material properties) indicate it is feasible to vaporize carbon black with high power densities in time scales of 100 ns or less. Thus, it is possible to reach temperatures on the order of thousands of kelvins in a short time, which likely explains the initial rise in the signal from the 700 nm pyrometry channel at high power densities. At this point, only a small amount of the ignition increment is super-heated (about 1%), which explains the relatively low signal strength. Later in time, as the heat from the carbon black is transferred to the explosive, the explosive reaches the point where self-sustained reaction is possible, and the tremendous temperatures generated by the release of chemical energy in the explosive (which comprises 99% of the ignition increment mixture) causes the subsequent increase in the 700 nm pyrometer signal that leads to the distinct inflection point first described in Section 6.1.

Indirectly, this phenomenon suggests that some significant portion of the explosive must be heated to or above the critical temperature for self-sustained reaction to commence. If the problem is reduced to a single spherical explosive particle that is heated by high-temperature carbon black particles that uniformly surround the explosive particle, one can imagine the temperature gradients that would be present in the portions of the explosive particle that are adjacent to carbon black particles as a function of time. At some given time, a significant enough portion of the explosive particle will be heated to levels that allow for chemical energy release that is significant enough to heat neighboring portions of the explosive particle and other explosive particles to allow for self-sustained reaction.

Unfortunately, it is extremely difficult to simulate even this seemingly simple reduced problem. To begin with, it is necessary to know how effectively and uniformly the carbon black is mixed with the explosive, in addition to detailed knowledge of the particle size distribution of both the carbon black and explosive. Because of the small length and time scales associated with the problem, details concerning the distance between particles and crystal imperfections and inclusions also are critical to characterize. Furthermore, it is necessary to have detailed material property information. Finally, the problem is further complicated by the fact that the carbon black is not a perfect absorber (it reflects and transmits the 808 nm laser light in addition to absorbing it), and the explosive is not a perfect transmitter (it reflects and absorbs 808 nm laser light

in addition to transmitting it). Such a calculation is beyond the scope of the present work, but if resources allow, such calculations may be attempted in the future.

9 Summary

Laser diode ignition experiments were conducted to investigate the effects of scale and heating rate on critical temperature of the explosive. It was noted that at the lowest power density (i.e., slowest heating rate but largest spot size), a lower energy density was required to initiate the explosive with a 200 micron spot size compared to a 100 micron spot size; however, spot size did not appear to affect energy density at higher power densities. At those higher power densities, it was found that the energy density required to initiate the explosive was higher than for lower power densities. This was attributed to non-uniform heating of the carbon black compared to the explosive, which resulted in a "lag" in the temperature increase of the explosive compared to the carbon black. This indirectly implies the existence of a critical volume, or mass, of the explosive that must be heated to or above the critical temperature before self-sustained ignition can occur. If this is the case, the critical volume is much smaller than the volume associated with the minimum spot size (40 microns) and penetration depth of the present experiments.

10 References

[1]Hafenrichter, E.S., Marshall, W.W., and Fleming, K.J. "Fast Laser Diode Ignition of CP and BNCP." *29th International Pyrotechnics Seminar*. 2002. Westminster, CO: pp. 787-793.

[2]Hafenrichter, E.S., Marshall, B.M., and Fleming, K.J. "Fast Laser Diode Ignition of Confined CP and BNCP." *41st Aerospace Sciences Meeting and Exhibit*. 2003. Reno, NV: AIAA-2003-0245.

[3]Hafenrichter, E.S. "Continued Studies on Fast Laser Diode Ignition of Confined Explosives." *31st International Pyrotechnics Seminar*. 2004. Fort Collins, CO: pp. 743-764.

[4]Brish, A.A., Galeeve, I.A., Zaitsev, B.N., Sbitnev, E.A., and Tatarinstev, L.V. "Laser-Excited Detonation of Condensed Explosives." *Fizika Goreniya i Vzryva*. 1966. **Vol. 2**(No. 3): pp. 132-133.

[5]Barbarisi, M.J., and Kessler, E.G. "Some Investigations of the Laser Initiation of Explosives." *Proceedings of the 6th Symposium on Electroexplosive Devices*. 1969. Franklin Institute, Philadelphia:

[6]Brish, A.A., Galeeve, I.A., Zaitsev, B.N., Sbitnev, E.A., and Tatarinstev, L.V. "Mechanism of Initiation of Condensed Explosives by Laser Radiation." *Fizika Goreniya i Vzryva*. 1969. **Vol. 5**(No. 4): pp. 457-480.

[7]Menichelli, V.J., and Yang, L.C. "Direct Laser Initiation of Insensitive Explosives." *7th Symposium on Explosives and Pyrotechnics*. 1971. Philadelphia, PA:

[8]Paisley, D.L. "Prompt Detonation of Secondary Explosives by Laser." *9th International Symposium on Detonation*. 1989. Portland, OR: pp. 1110-1117.

[9]Renlund, A.M., Stanton, P.L., and Trott, W.M. "Laser Initiation of Secondary Explosives." *9th International Symposium on Detonation*. 1989. Portland, OR: pp. 1118-1127.

[10]Yang, L.C., and Menichelli, V.J. "Laser Initiation of Insensitive High Explosives." *6th International Symposium on Detonation*. 1976. Coronado, CA: pp. 612-621.

[11]Craig, R., Gignac, W. Worland, P., and Stephenson, J. "Laser Diodes for Pyrotechnic Applications." *AIAA/SAE/ASME/ASEE 29th Joint Propulsion Conference and Exhibit*. 1993. Monterey, CA: AIAA 93-2359.

[12]Ewick, D.W., and Beckman, T.M. "Ignition Testing of Low-Energy Laser Diode Ignited Components." MLM-MU-90-64-003. EG&G Mound Applied Technologies. 1990.

[13]Ewick, D.W. "Finite Difference Modeling of Laser Diode Ignited Components." *15th International Pyrotechnics Seminar*. 1990. Boulder, CO: pp. 277-296.

[14]Ewick, D.W. "Improved 2-D Finite Difference Model for Laser Diode Ignited Components." *18th International Pyrotechnics Seminar*. 1992. Breckenridge, CO: pp. 255-266.

[15]Glass, M.W., Merson, J.A., and Salas, F.J. "Modeling Low Energy Laser Ignition of Explosive and Pyrotechnic Powders." *18th International Pyrotechnics Seminar*. 1992. Breckenridge, CO: pp. 321-334.

[16]Jungst, R.G., and Salas, F.J. "Diode Laser Ignition of Explosive and Pyrotechnic Components." *Optoelectronics 90*. 1990. Albuquerque, NM:

[17]Jungst, R.G., Salas, F.J., Watkins, R.D., and Kovacic, L. "Development of Diode Laser-Ignited Pyrotechnic and Explosive Components." *15th International Pyrotechnics Seminar*. 1990. Boulder, CO: pp. 549-568.

[18]Kunz, S.C., and Salas, F.J. "Diode Laser Ignition of High Explosives and Pyrotechnics." *13th International Pyrotechnics Seminar*. 1988. Grand Junction, CO: pp. 505-523.

[19]Roman, N.B.M. "Laser Ignition of Explosives and its Application in a Laser Diode Based Ignition System." *16th International Pyrotechnics Seminar*. 1991: pp. 822-836.

[20]Skocypec, R.D., Mahoney, A.R., Glass, M.W., Jungst, R.G., Evands, N.A., and Erickson, K.L. "Modeling Laser Ignition of Explosives and Pyrotechnics: Effects and Characterization of Radiative Transfer." *15th International Pyrotechnics Seminar*. 1990. Boulder, CO: pp. 877-894.

[21]Watson, B. "Laser Initiated Actuator Study." Document DTR-271. Unidynamics/Phoenix. 1991.

[22]Lee, L.M., Mohler, J.M., and West, G.T. "Characterization of the DDT Explosive, CP." *Seventh International Symposium on Detonation*. 1981. Annapolis, MD: pp. 865-876.

[23]Fronabarger, J., Schuman, A., Chapman, R., Fleming, W., Sanborn, W., and Massis, T. "Chemistry and Development of BNCP, A Novel DDT Explosive." *31st AIAA/ASME/SAE/ASEE Joint Propulsion Conference and Exhibit.* 1995. San Diego, CA: AIAA 95-2858.

[24]DeWitt, D.P. and Nutter, G.D. *Theory and Practice of Radiation Thermometry*. 1988. New York: Wiley-Interscience.

[25]Cashdollar, K.L., Hertzberg, M. "Infrared Pyrometers for Measuring Dust Explosion Temperatures." *Optical Engineering*. 1982. **Vol. 21**(1): pp. 82-86.

[26]Fletcher, T.H. "Time-Resolved Temperature Measurements of Individual Coal Particles During Devolatilization." *Combustion Science and Technology*. 1989. **Vol. 63**: pp. 89-105.

[27]Isreal, F., Taylor, A.M.K.P., and Whitelaw, J.H. "Simultaneous Measurement of Droplet Velocity and Size and Flame Mantle Temperature by Phase Doppler Anemometry and Two-Colour Pyrometry." *Measurement Science Technology*. 1995. **Vol. 6**: pp. 727-741.

[28]Jorgensen, F.R.A., and Zuiderwyk, M. "Two-Colour Pyrometer Measurement of the Temperature of Individual Combusting Particles." *Journal of Physics E: Scientific Instrumentation*. 1985. **Vol. 18**: pp. 486-491.

[29]Leal-Crouzet, B., Bourinnes, R., Baudin, G., Goutelle, J.C. "Ultra-Fast Optical Pyrometry for the Measurement of Detonating Explosive Temperature." *European Physics Journal*. 1999. **Vol. 8**: pp. 189-194.

[30]Brewster, M.Q. *Thermal Radiative Transfer and Properties*. 1992. New York: Wiley-Interscience.

[31]Siegel, R. and Howell, J.R. *Thermal Radiation Heat Transfer*. 4th Ed. ed. 2002. New York: Taylor and Francis.

[32]Bohren, C.F. and Huffman, D.R. *Absorption and Scattering of Light by Small Particles*. 1983. New York: Wiley-Interscience.

[33]Teukolsky, S.A., Vetterling, W.T., Flannery, B.P. *Numerical Recipes for Fortran 77*. Vol. Vol. 1. 1992. Cambridge: Cambridge University Press.

[34]Kaviany, M. *Principles of Heat Transfer in Porous Media*. 2nd. Ed. ed. 1995: Springer-Verlag.

[35]Lide, D.R. Handbook of Chemistry and Physics. 84th E. 2003. Boca Raton. CRC Press.

11 Figures

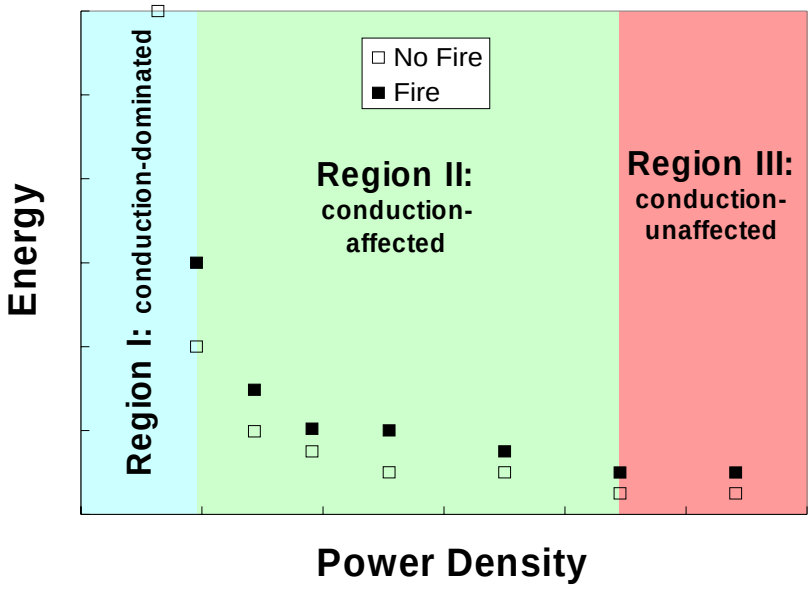

Figure 1: Firing energy vs. power density for typical LDI devices.

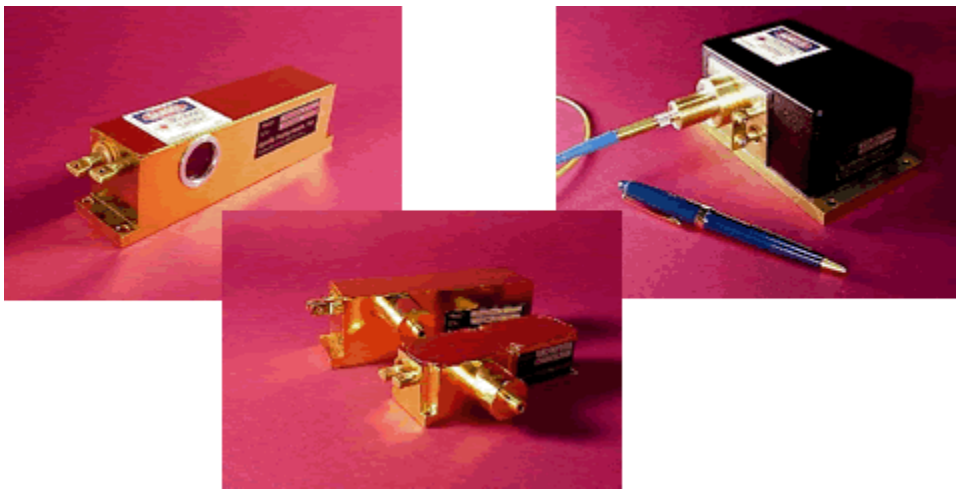

Figure 2: Photograph of laser diode (upper right).

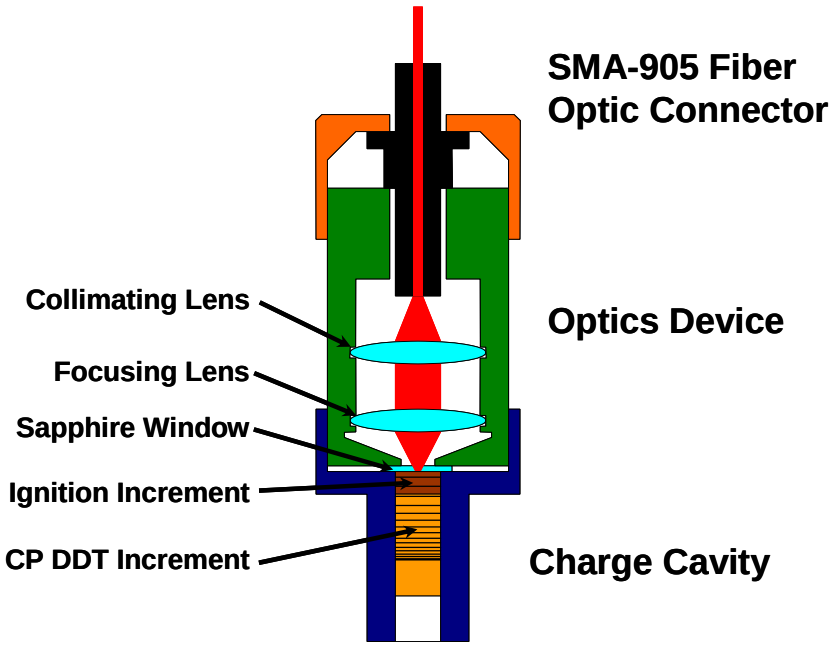

Figure 3: Schematic of LDI detonator (not to scale).

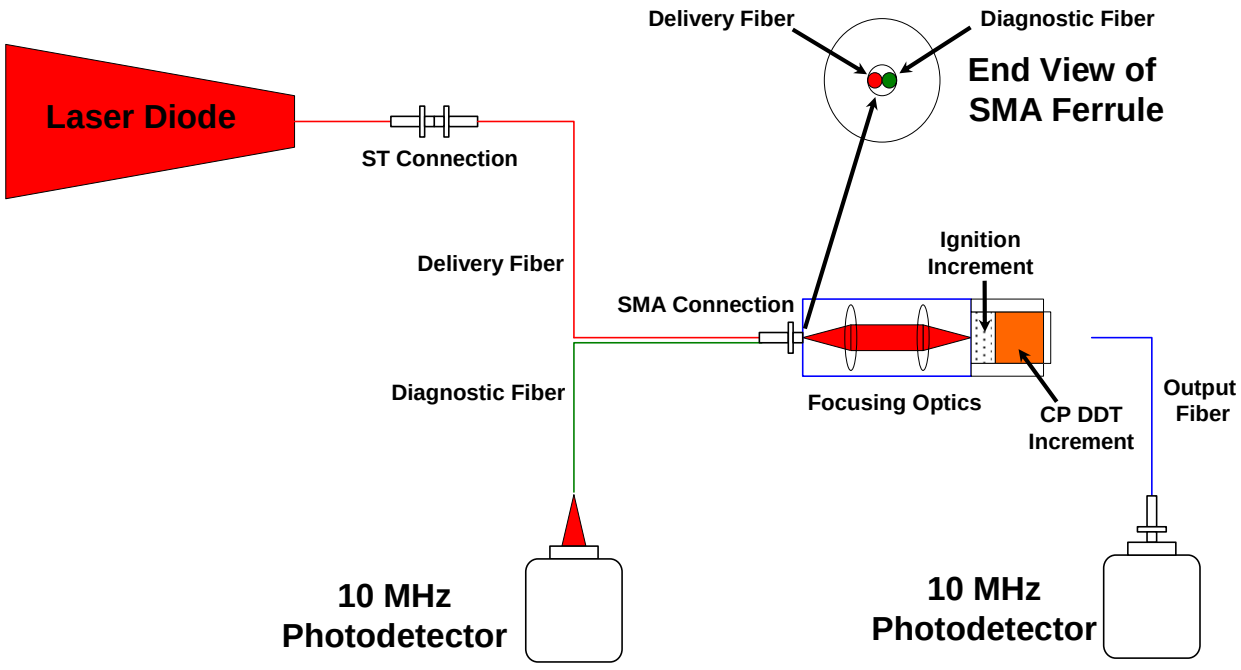

Figure 4: Schematic of previous experimental set-up.

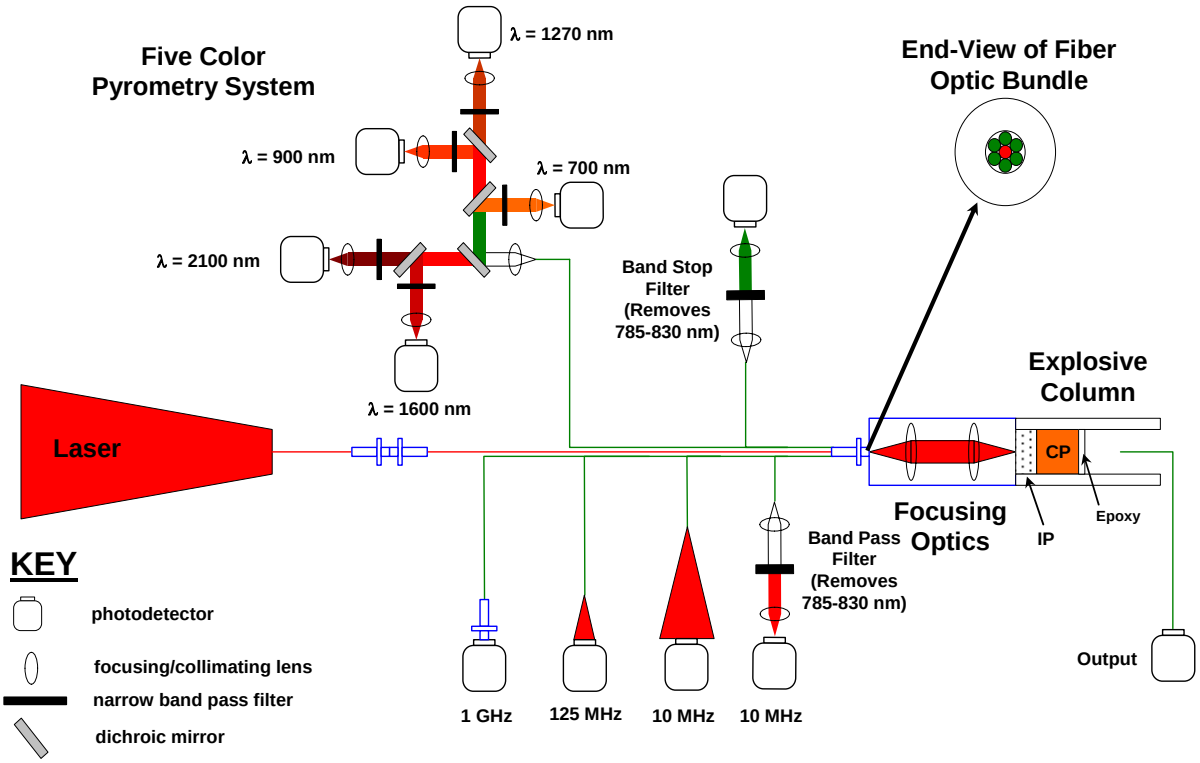

Figure 5: Schematic of present experimental set-up.

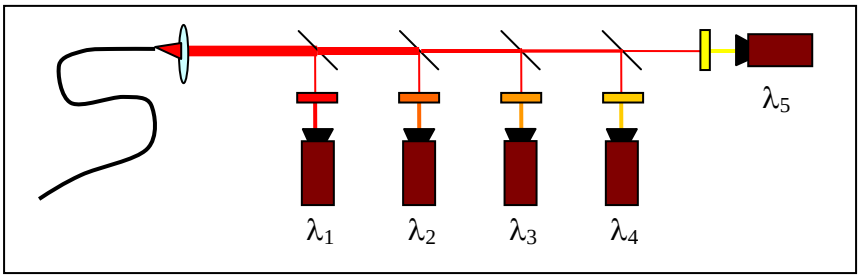

Figure 6: Standard layout of pyrometer.

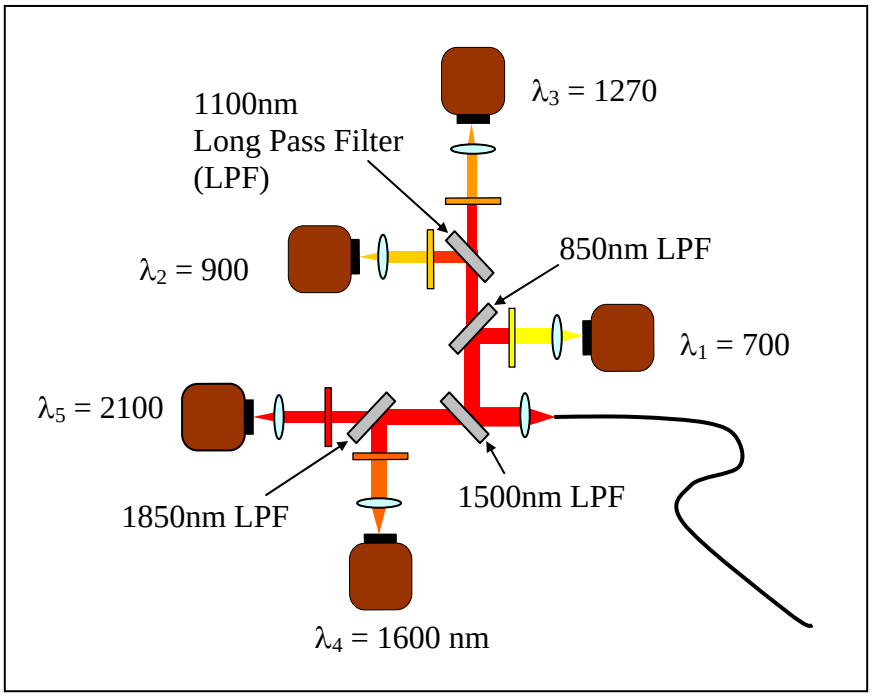

Figure 7: Five-color pyrometer layout.

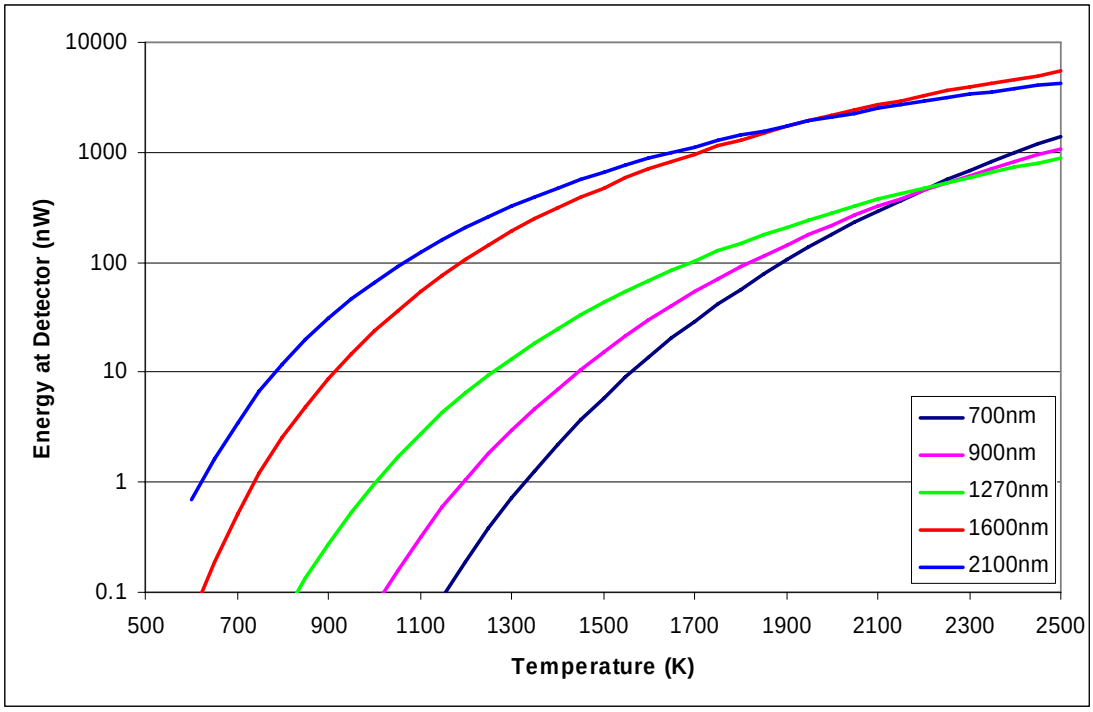

Figure 8: Estimated energy reaching the face of each pyrometer detector.

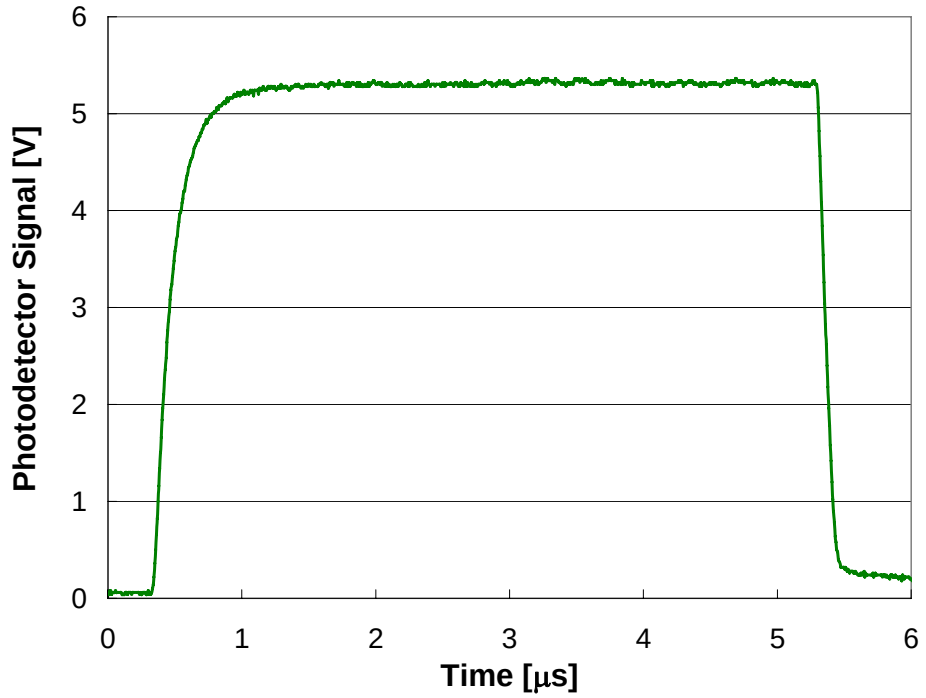

Figure 9: Laser signal reflected from face of energy meter.

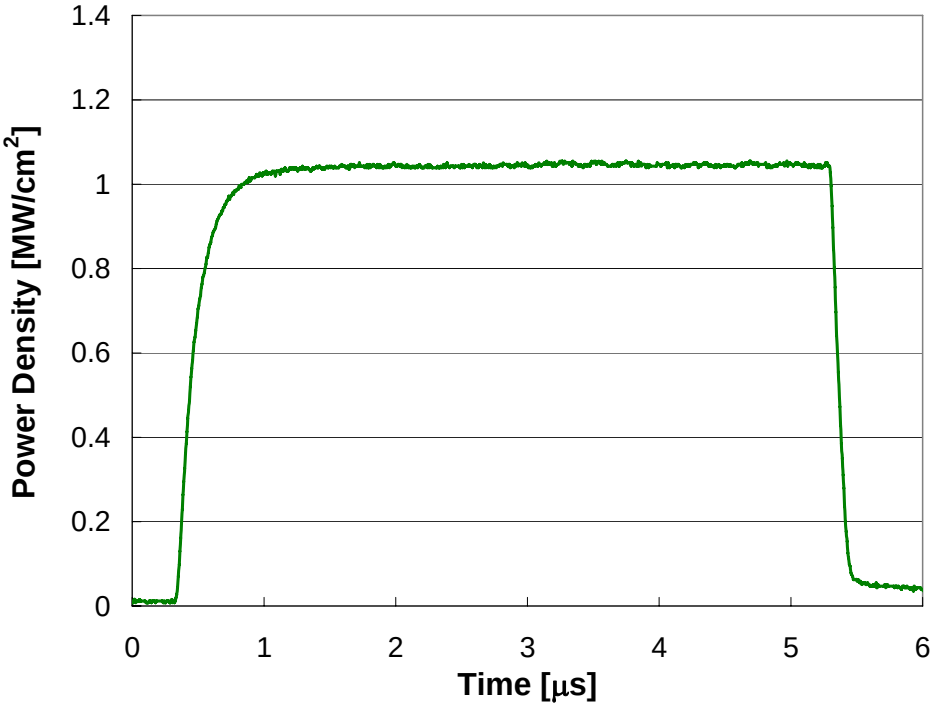

Figure 10: Power density vs. time calculated from previous figure.

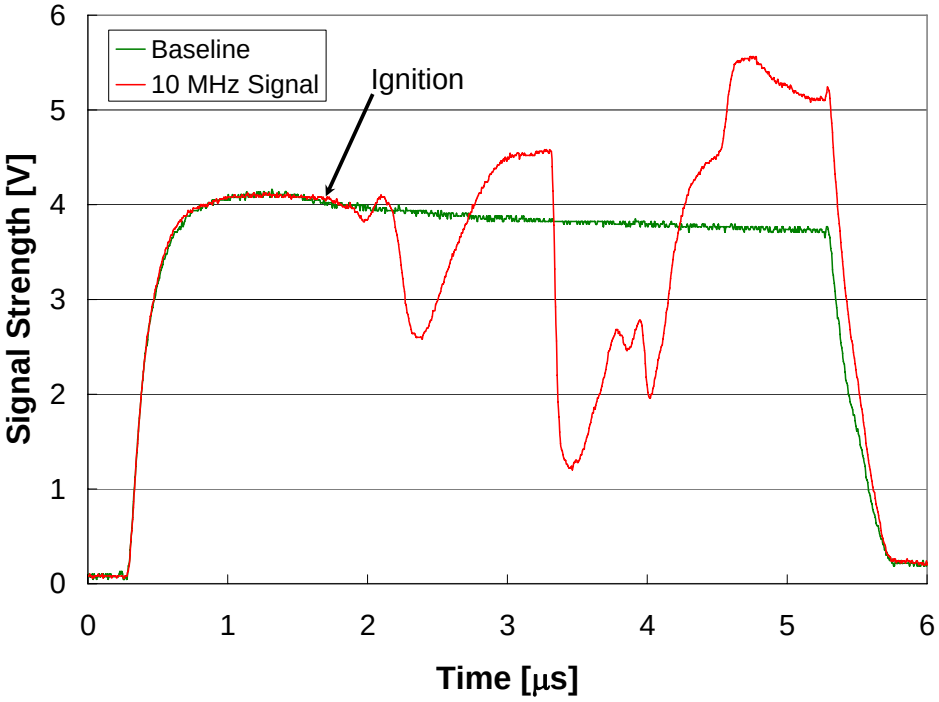

Figure 11: Photodetector comparison data, q_0" = 0.2 MW/cm^2.

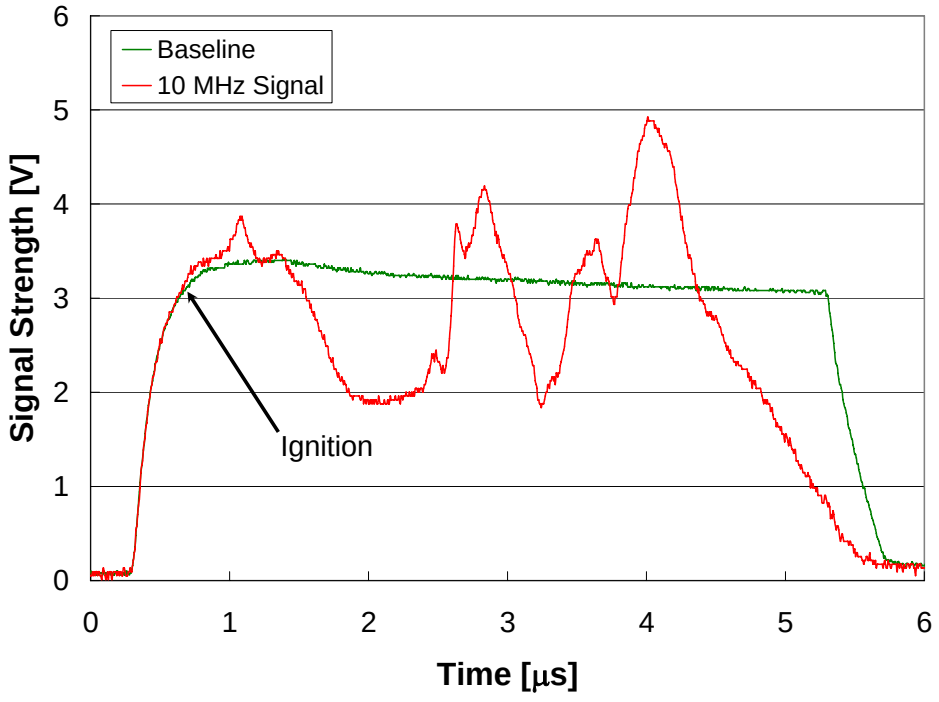

Figure 12: Photodetector comparison data, q_0" = 2.5 MW/cm^2.

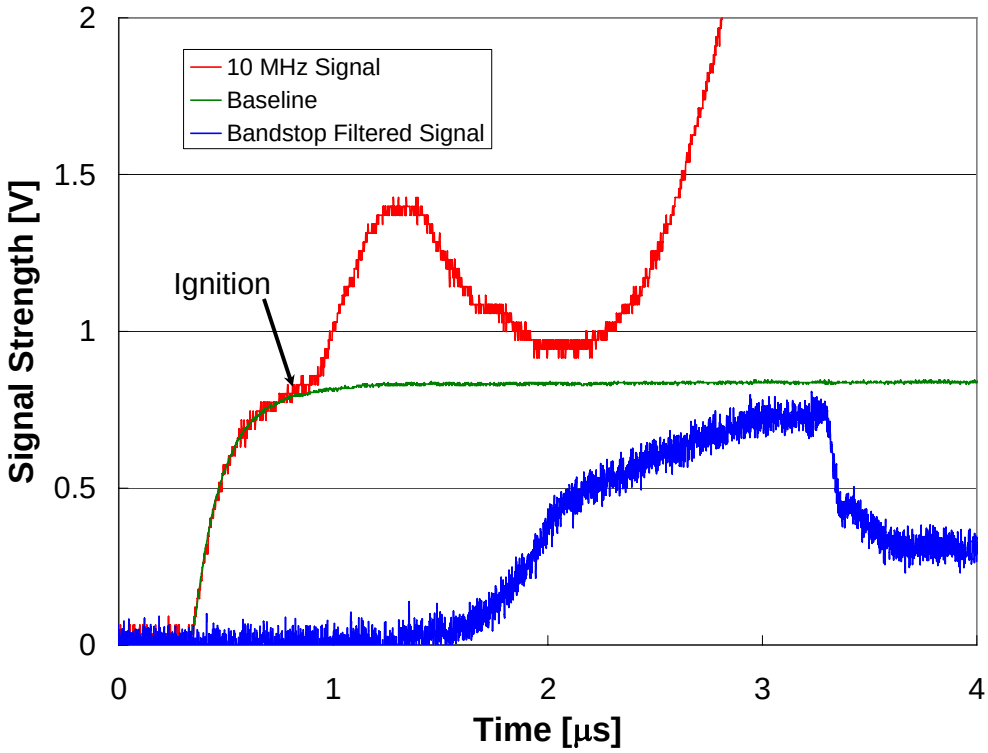

Figure 13: Bandstop filtered data.

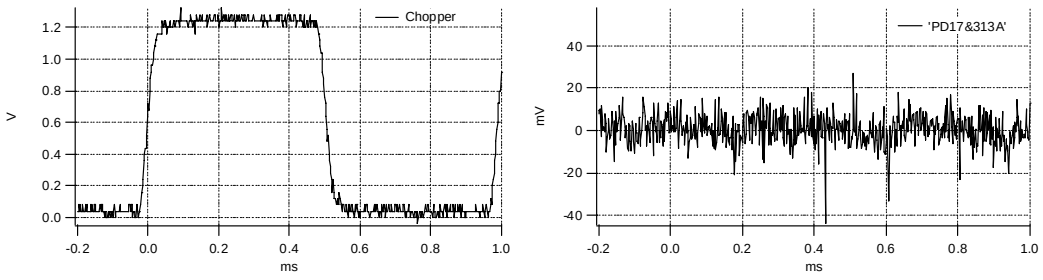

Figure 14: Noise levels from the photodetector-amplifier combination.

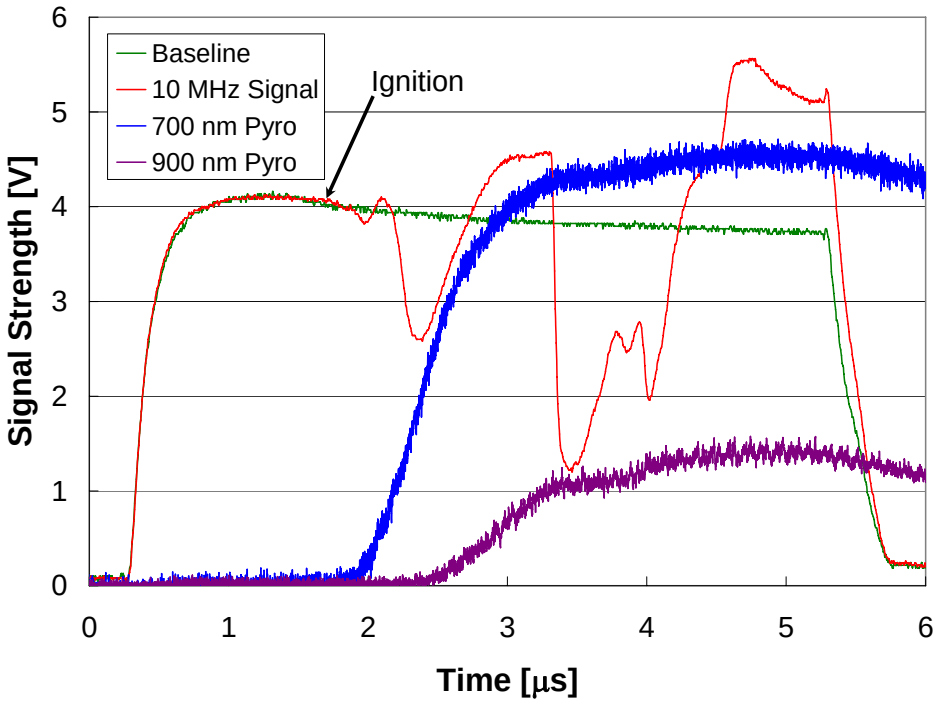

Figure 15: Pyrometer data from a typical experiment (SN02-020-2-A09).

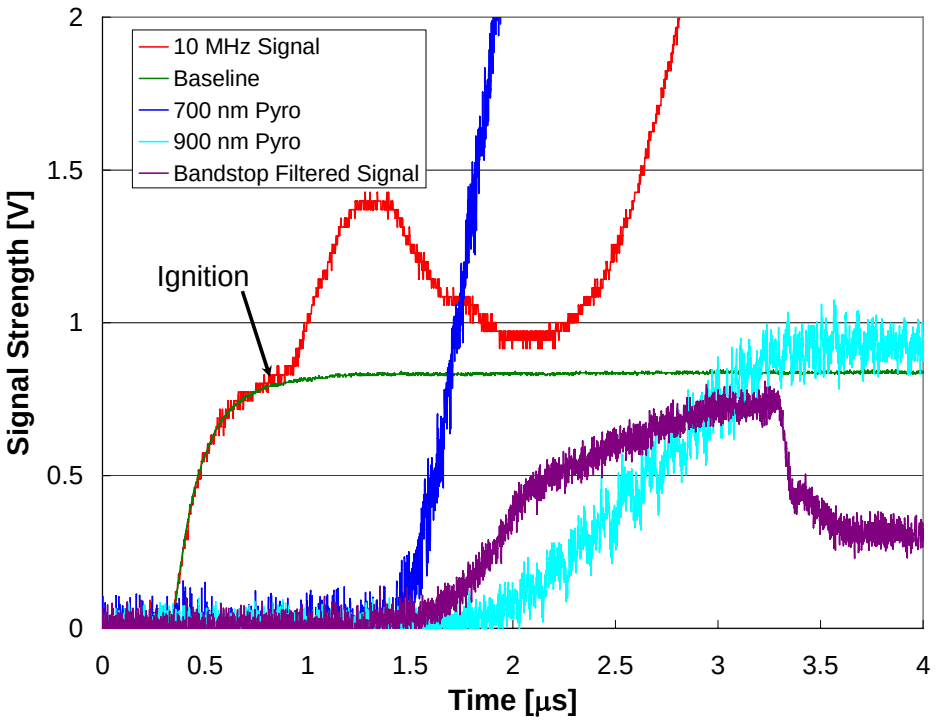

Figure 16: Pyrometry data, 700 nm and 900 nm channels.

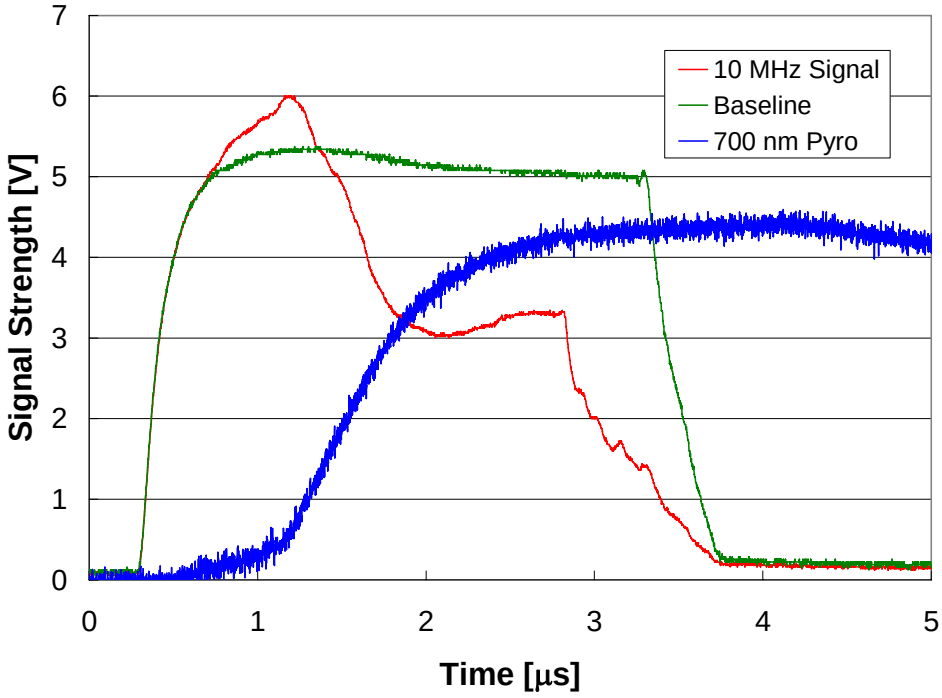

Figure 17: Data from SN01-C17, 3 μs pulse width.

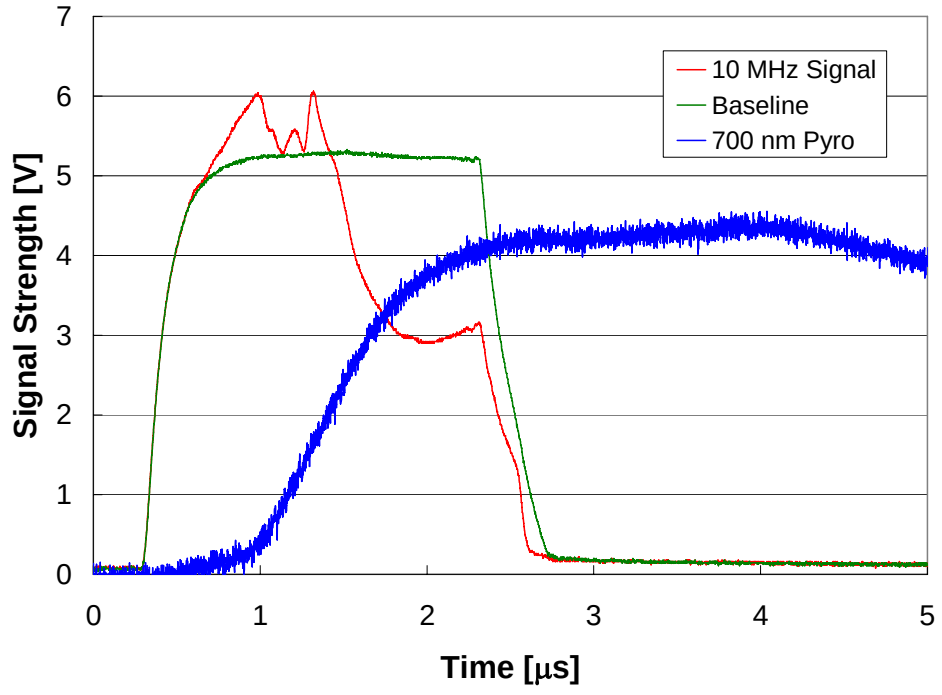

Figure 18: Data from SN02-C21, 2 μs pulse width.

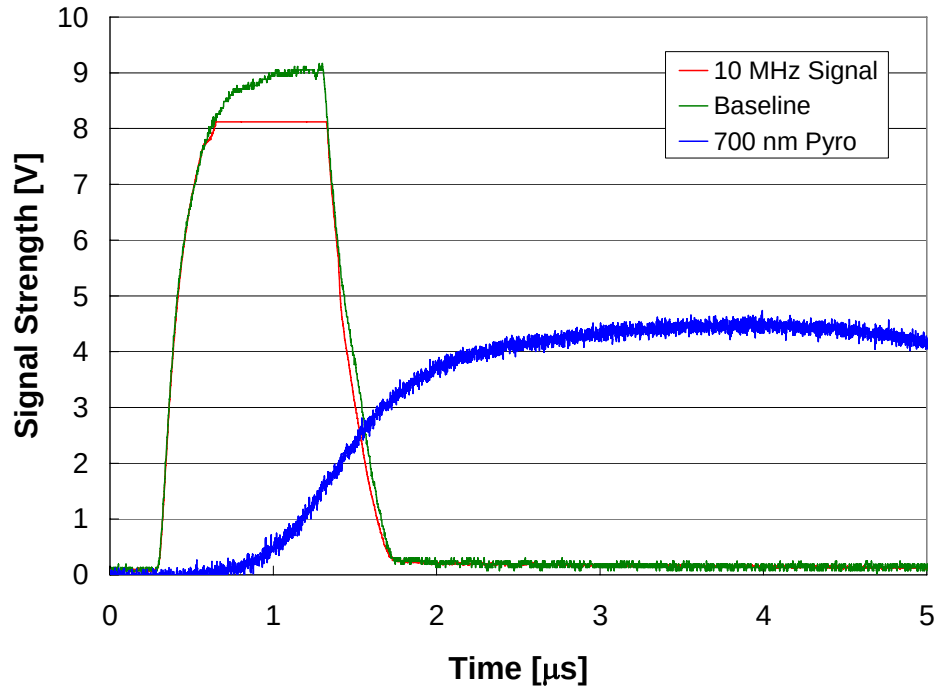

Figure 19: Data from SN03-C23, 1 μs pulse width.

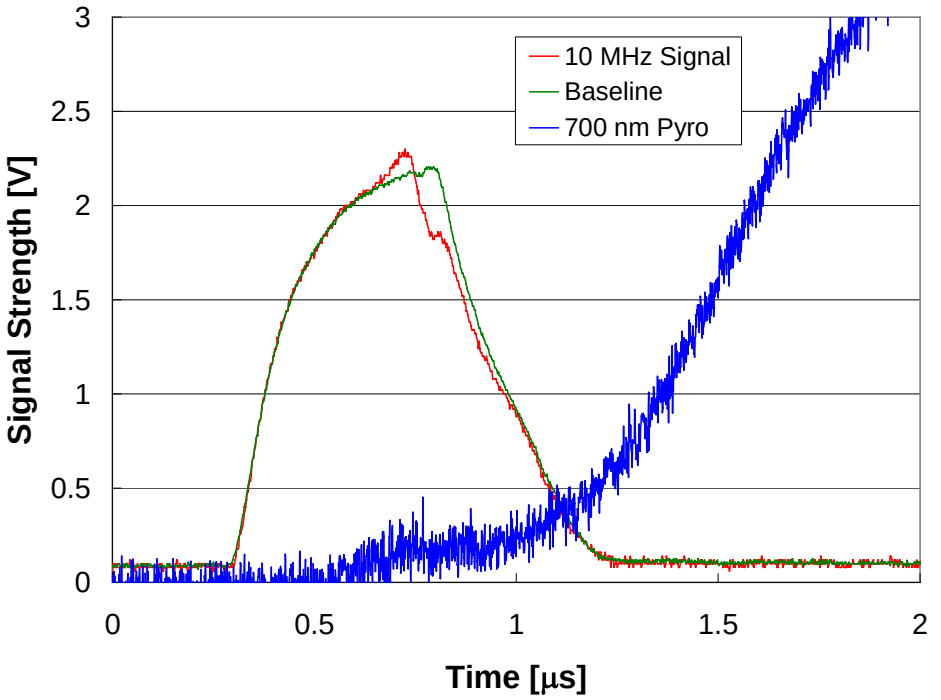

Figure 20: Data from SN04-C24, 0.5 μs pulse width.

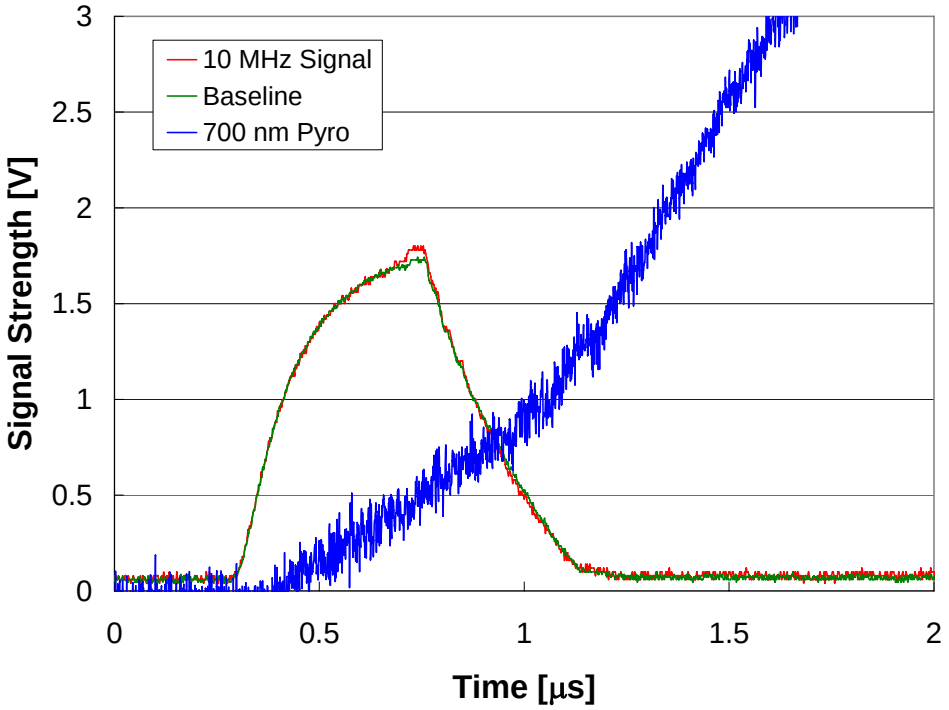

Figure 21: Data from SN06-C29, 450 ns pulse width (FIRE).

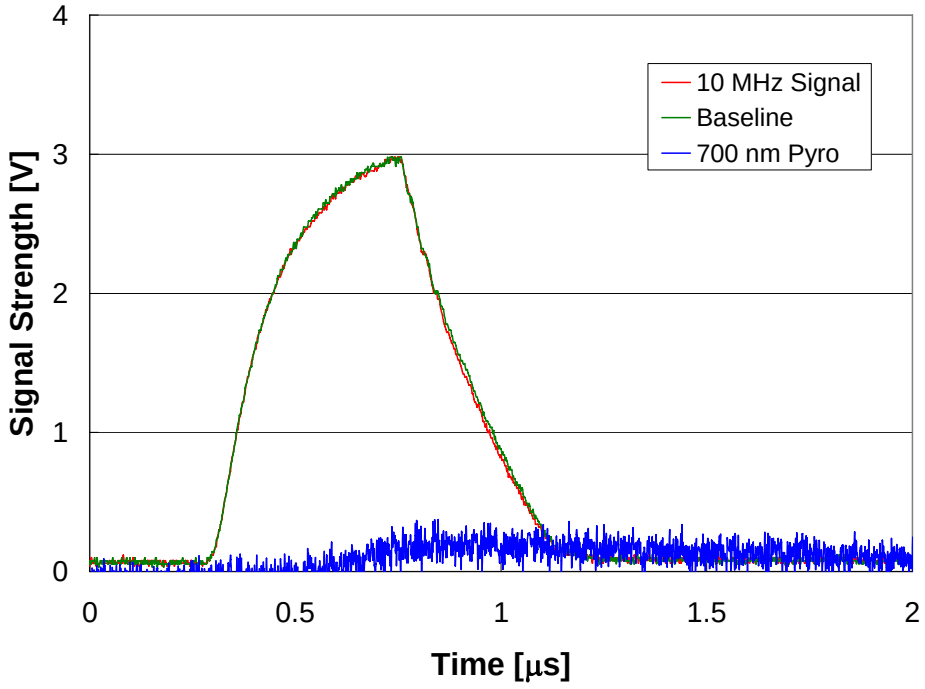

Figure 22: Data from SN07-C30, 450 ns pulse width (NO FIRE).

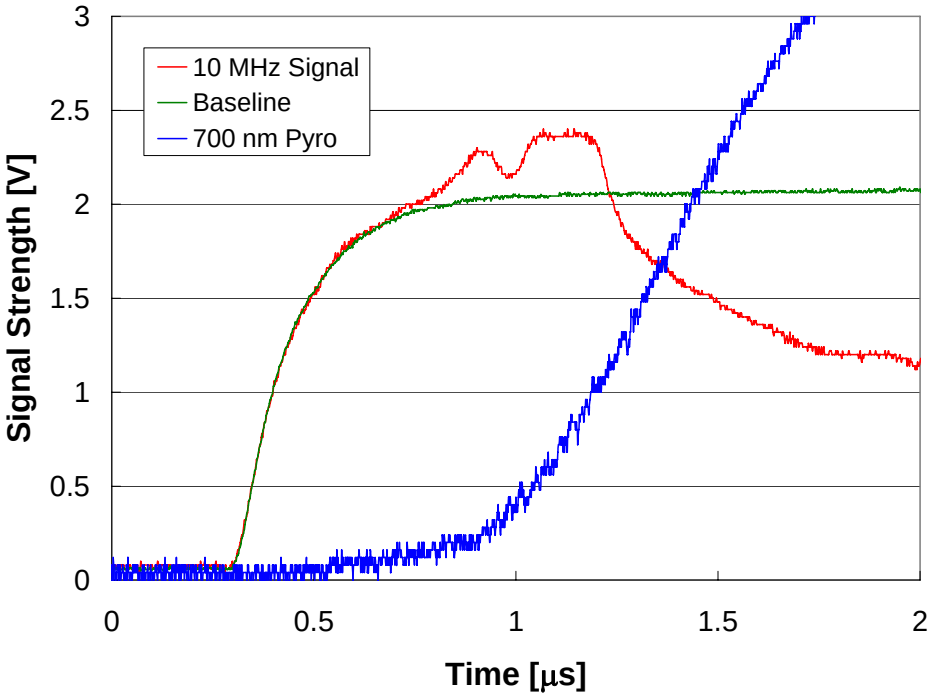

Figure 23: Experimental data, q_0" = 2.5 MW/cm^2, d_s = 50 μm.

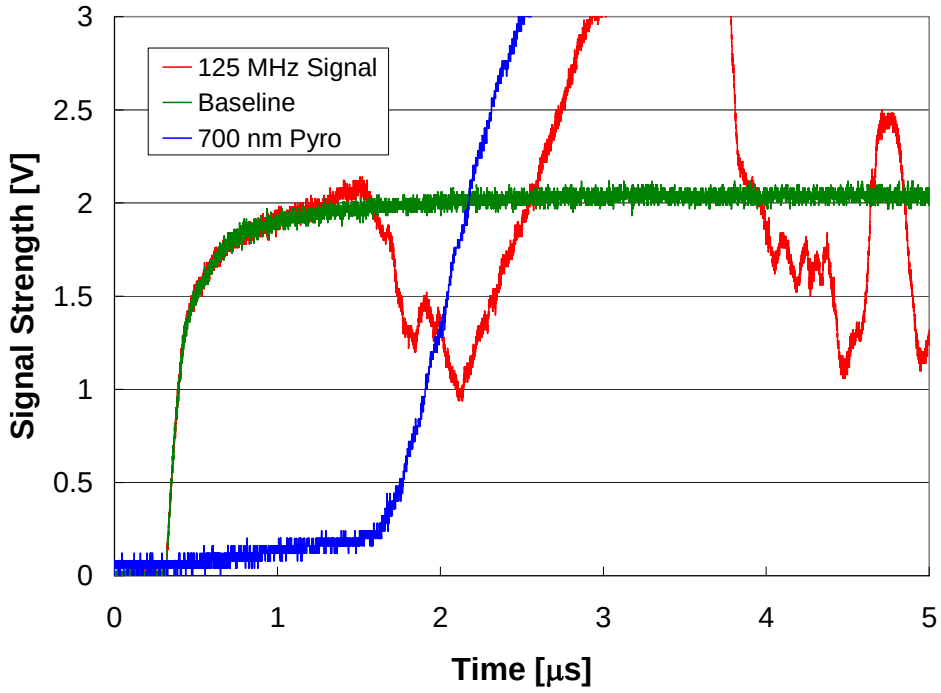

Figure 24: Experimental data, q_0" = 1 MW/cm^2, d_s = 50 μm.

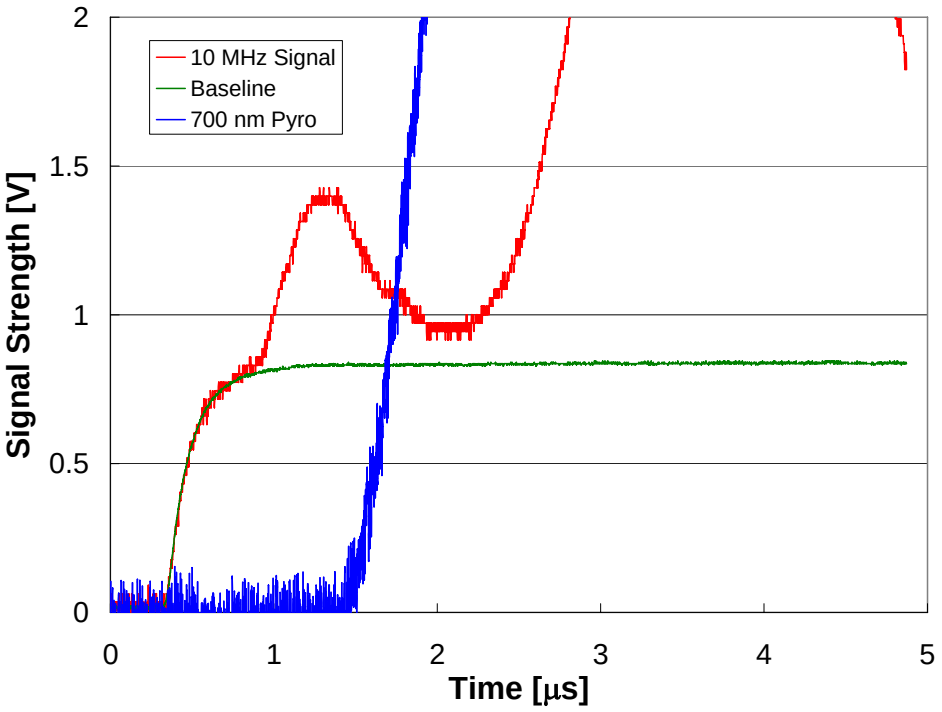

Figure 25: Experimental Data, q_0" = 1.0 MW/cm^2, d_s = 50 μm.

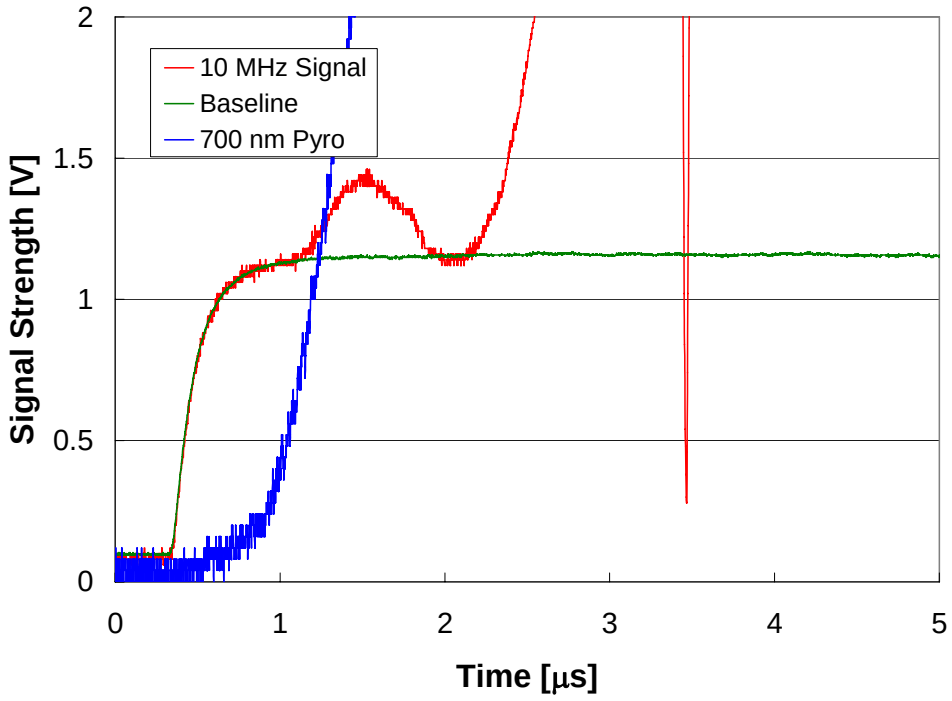

Figure 26: Experimental data, q_0" = 0.75 MW/cm^2, d_s = 50 μm.

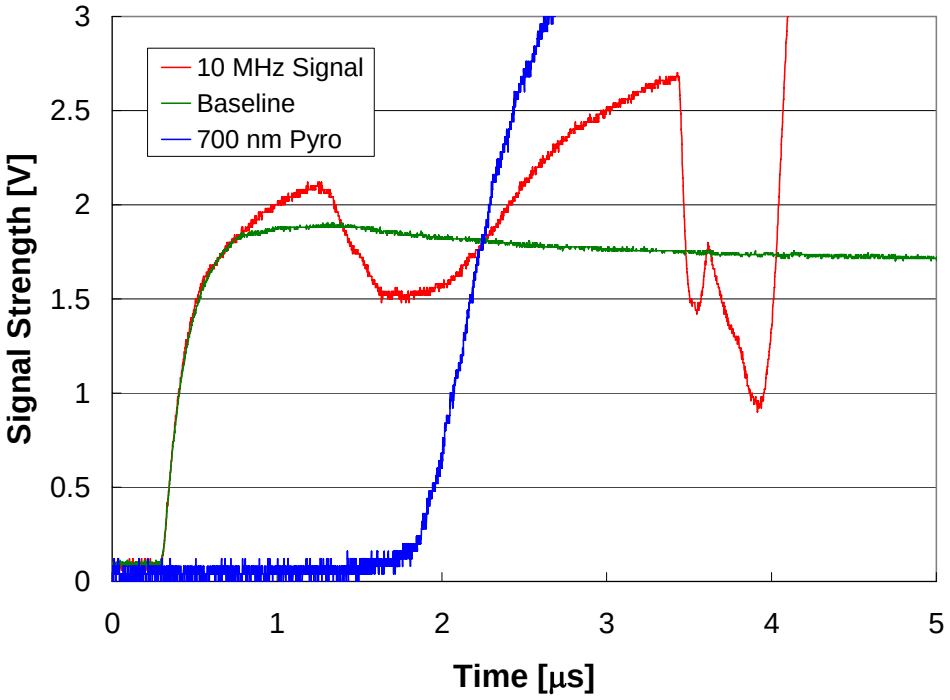

Figure 27: Experimental data, q_0" = 0.75 MW/cm^2, d_s = 100 μm.

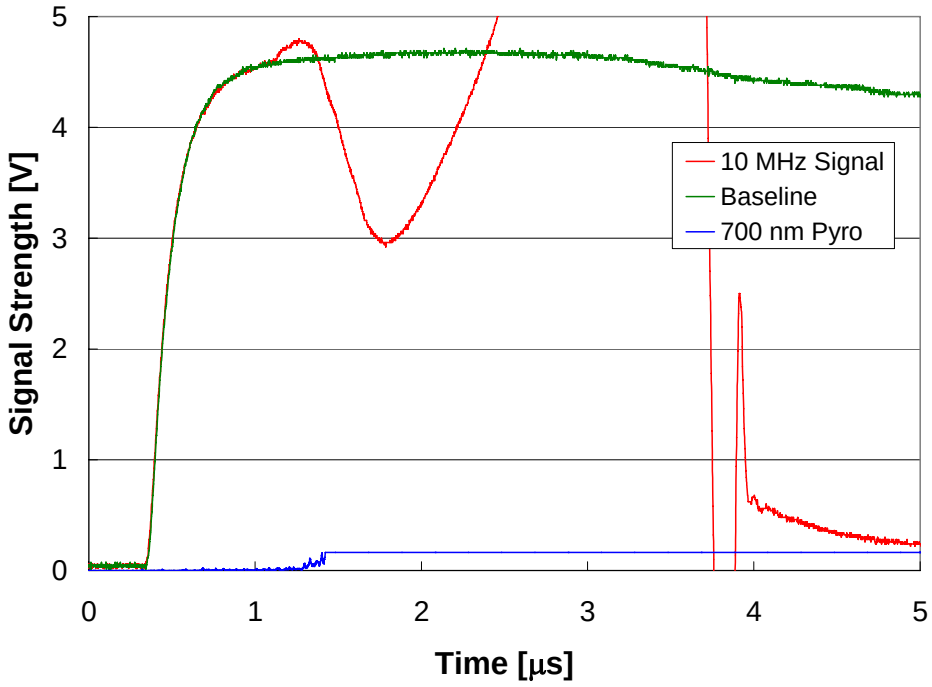

Figure 28; Experimental data, q_0" = 0.5 MW/cm^2, d_s = 50 μm.

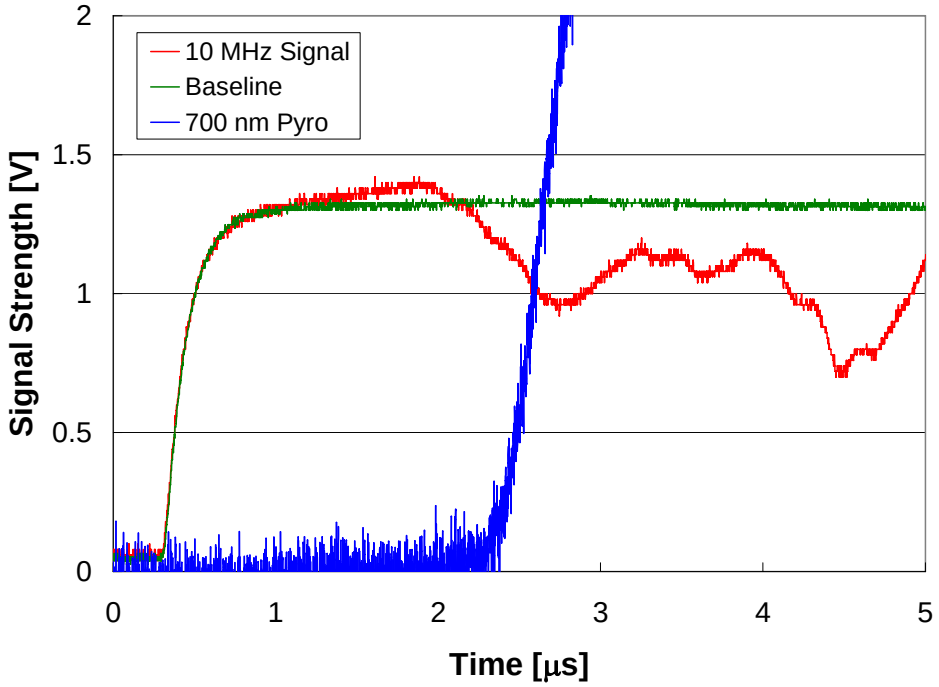

Figure 29: Experimental data, q_0" = 0.5 MW/cm^2, d_s = 100 μm.

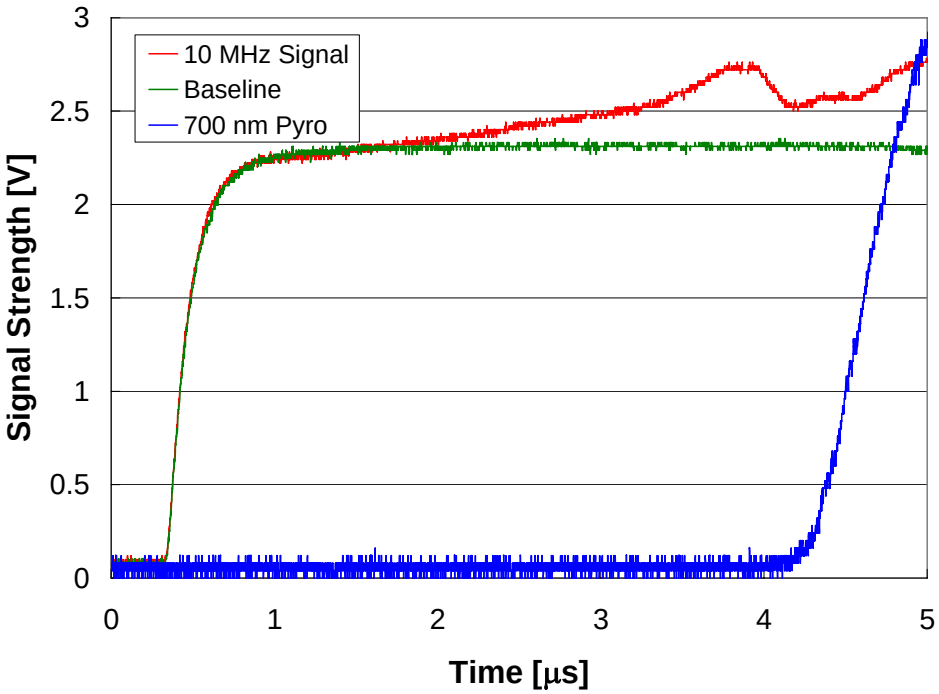

Figure 30: Experimental data, q_0" = 0.2 MW/cm^2, d_s = 100 μm.

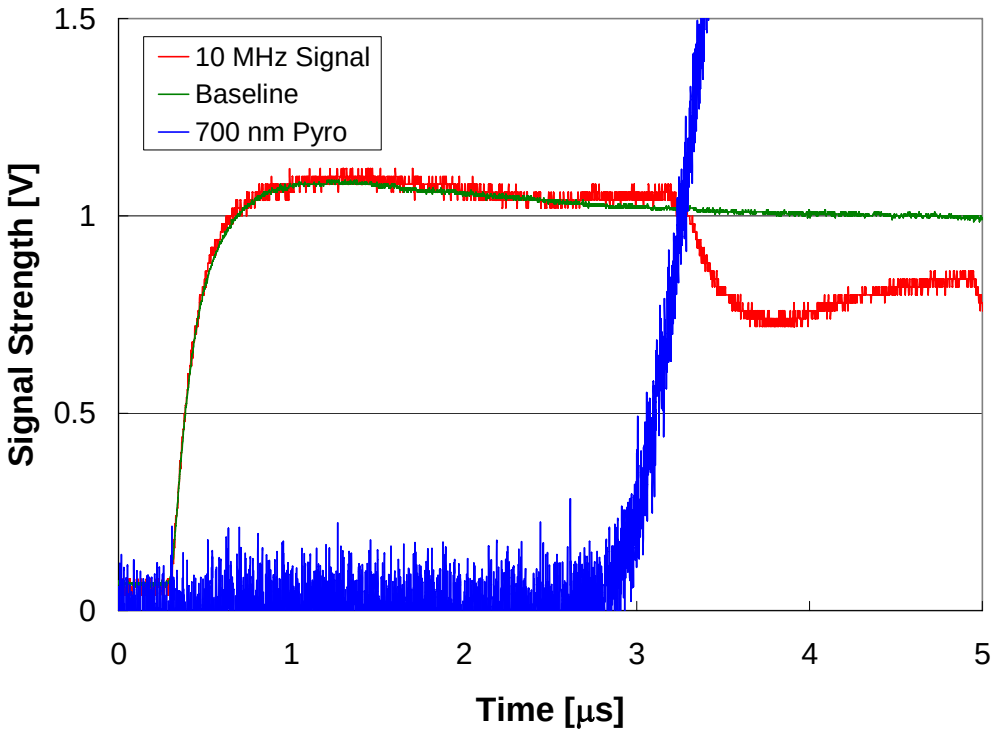

Figure 31: Experimental data, q_0" = 0.2 MW/cm^2, d_s = 200 μm.

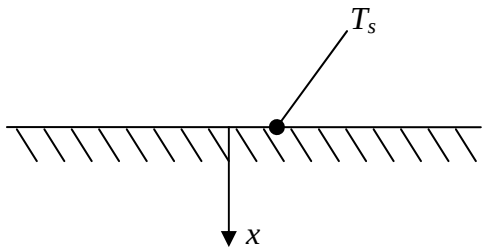

Figure 32: Diagram of infinite slab problem.

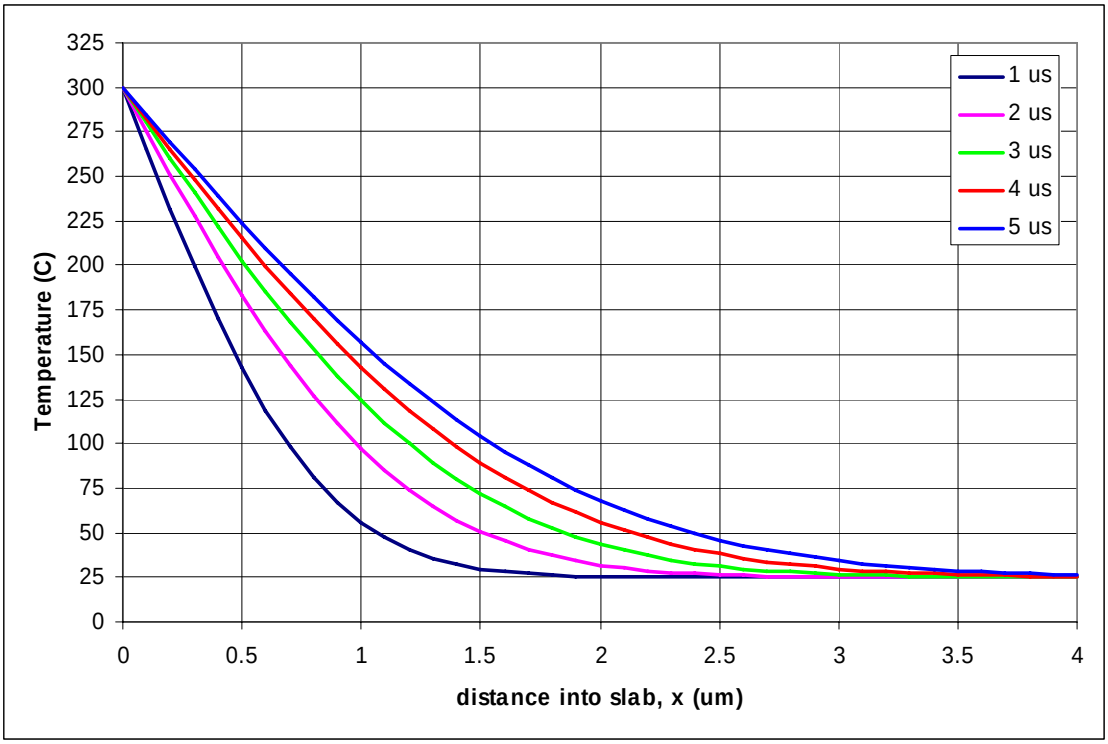

Figure 33: Temperature vs. distance into an infinite slab for different times.

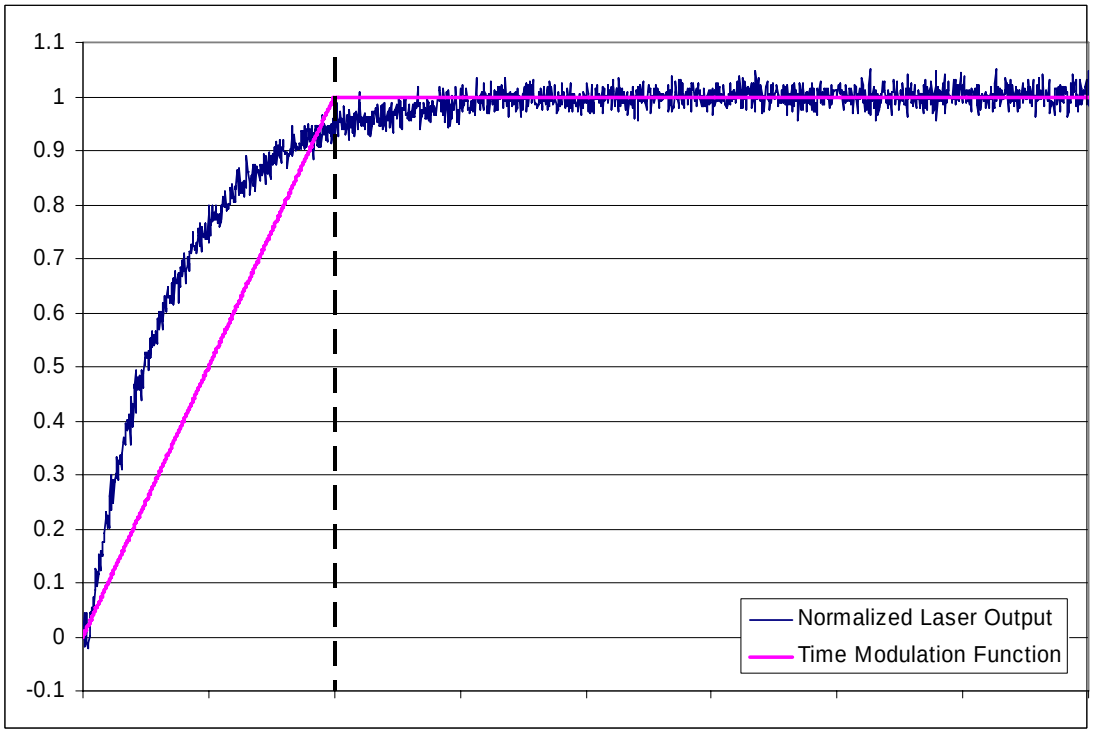

Figure 34: Time modulation function compared to baseline no-fire data.

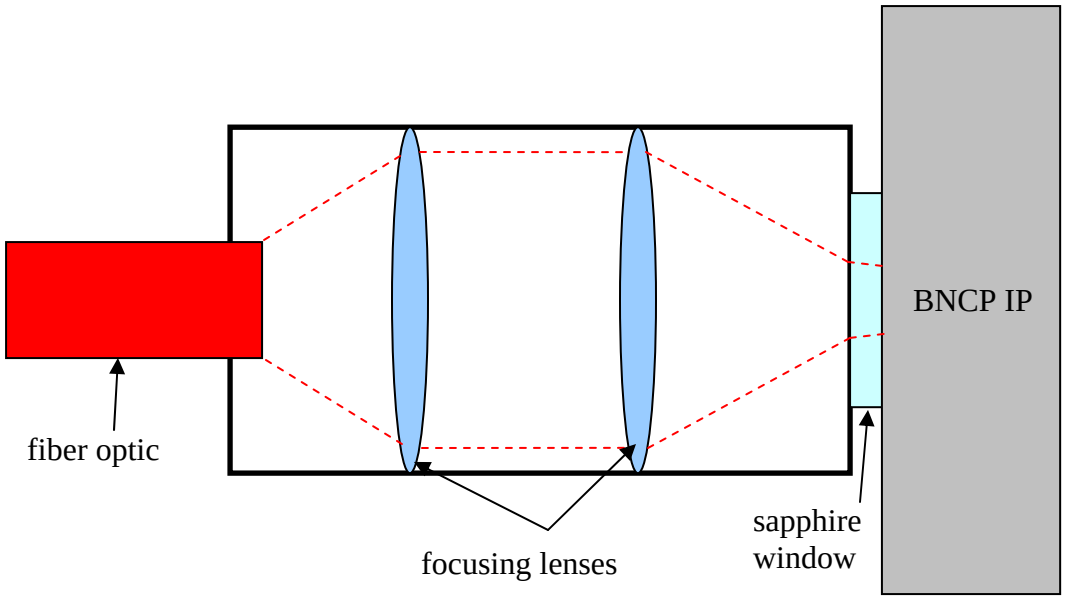

Figure 35: Diagram of detonator optics (not to scale).

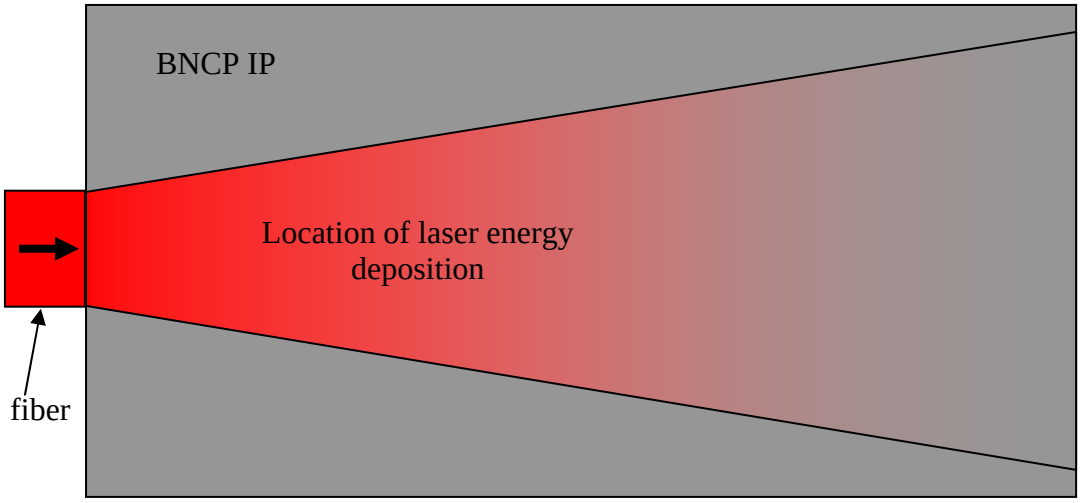

Figure 36: Spatial energy distribution function used by previous researchers.

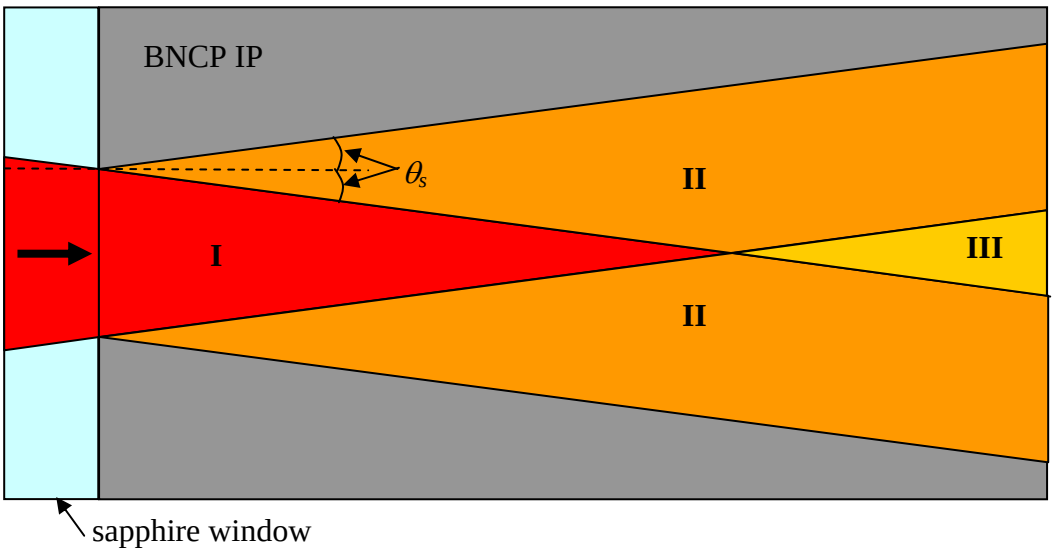

Figure 37: Diagram of actual energy distribution within IP column.

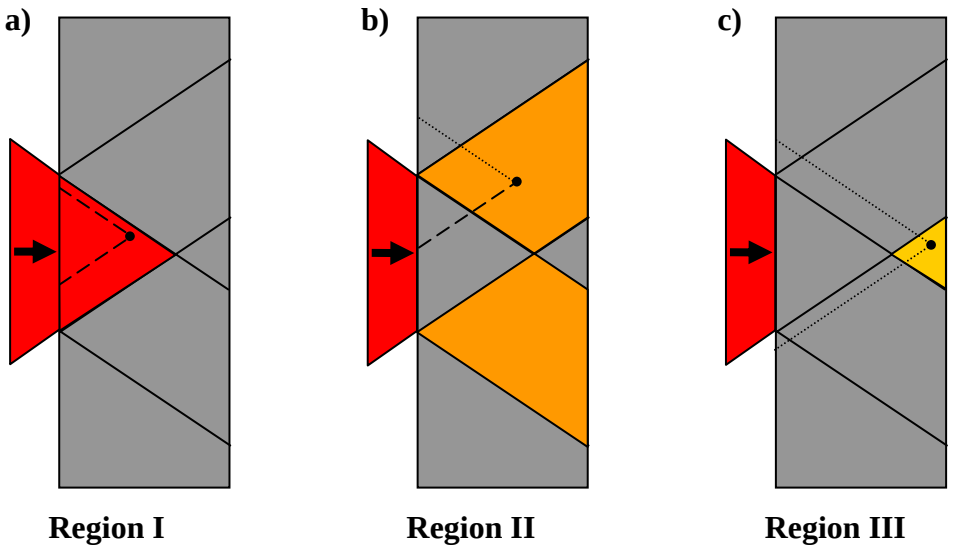

Figure 38: Regions of energy distribution in IP column.

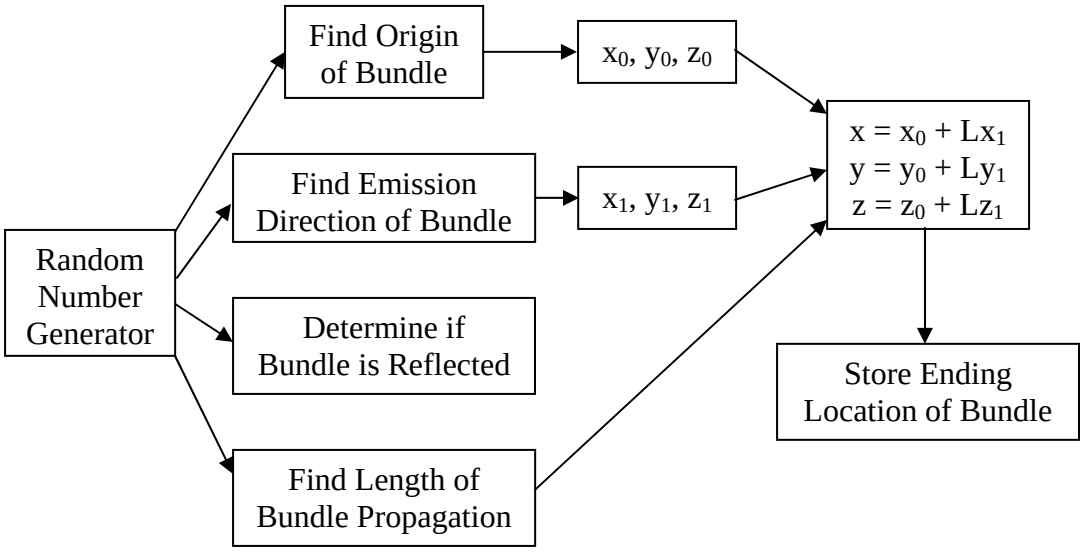

Figure 39: Block diagram of Monte Carlo code.

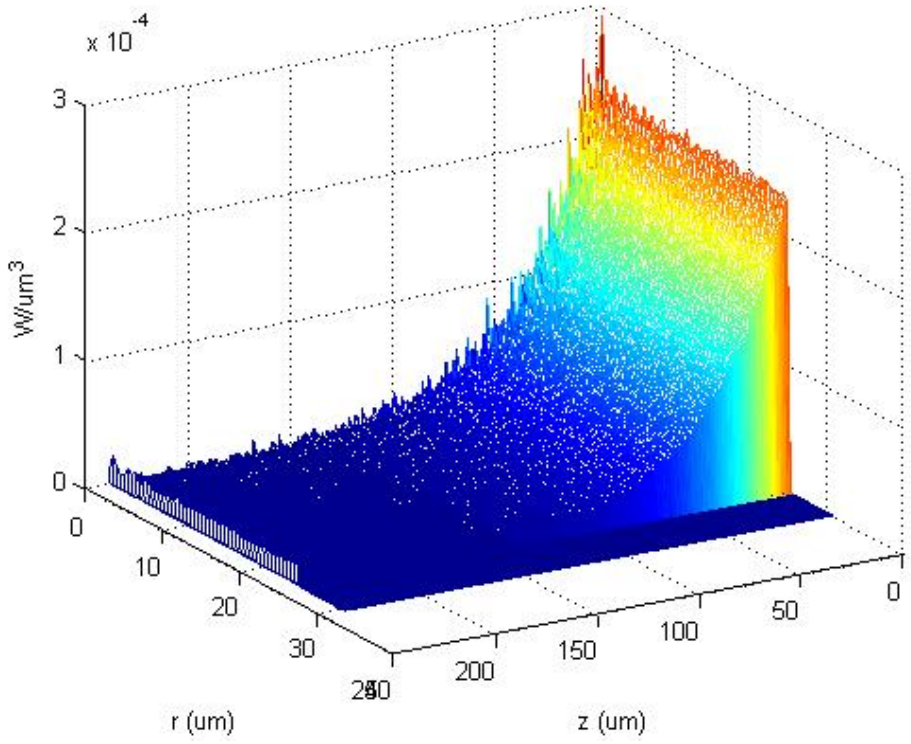

Figure 40: Energy deposition from Monte Carlo code

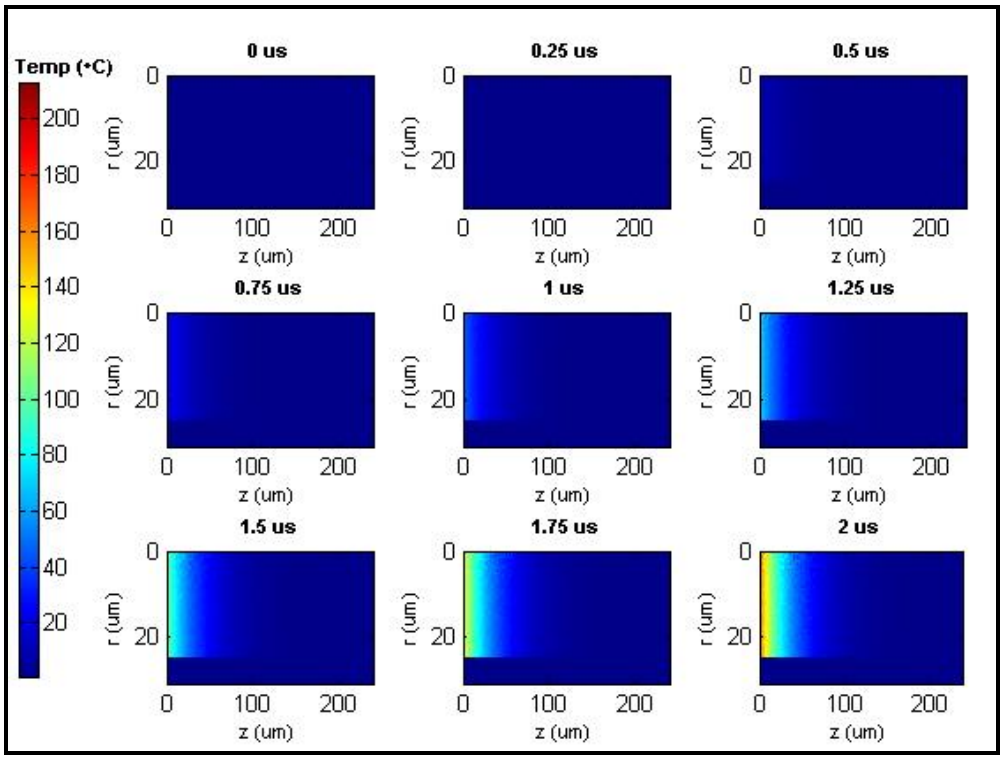

Figure 41: Temperature of IP column.

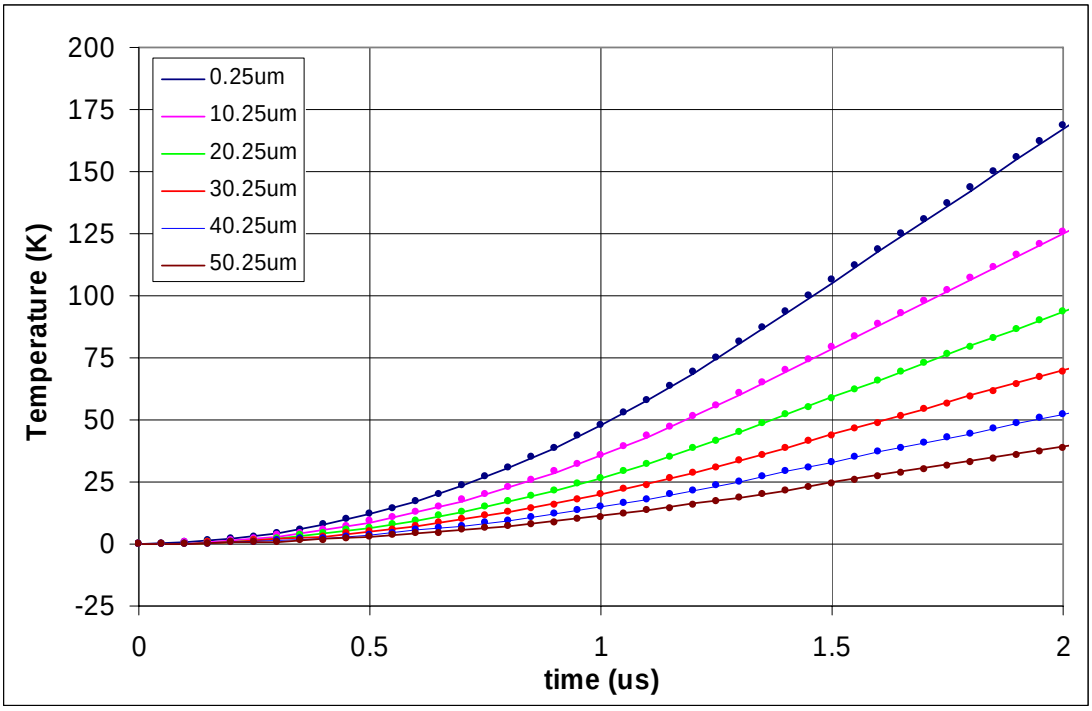

Figure 42: Comparison of Monte Carlo Code and analytical results.

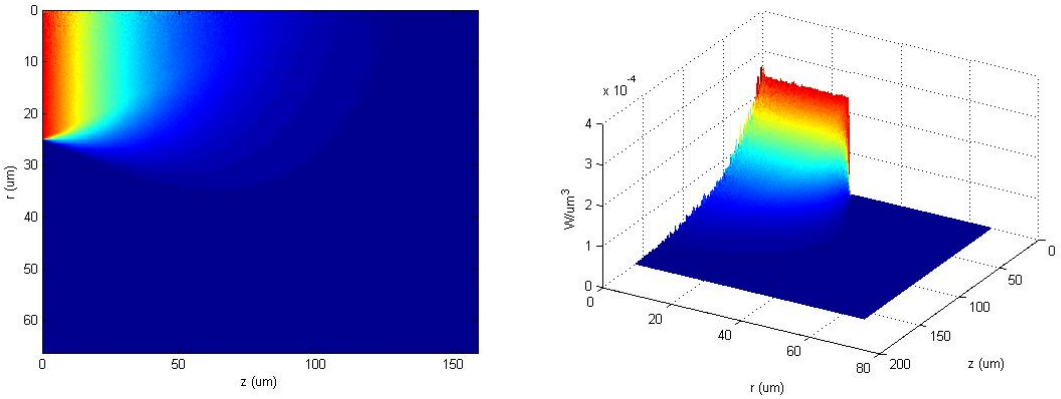

Figure 43: Contour and 3-D plot of spatial energy distribution for d_s = 50 μm.

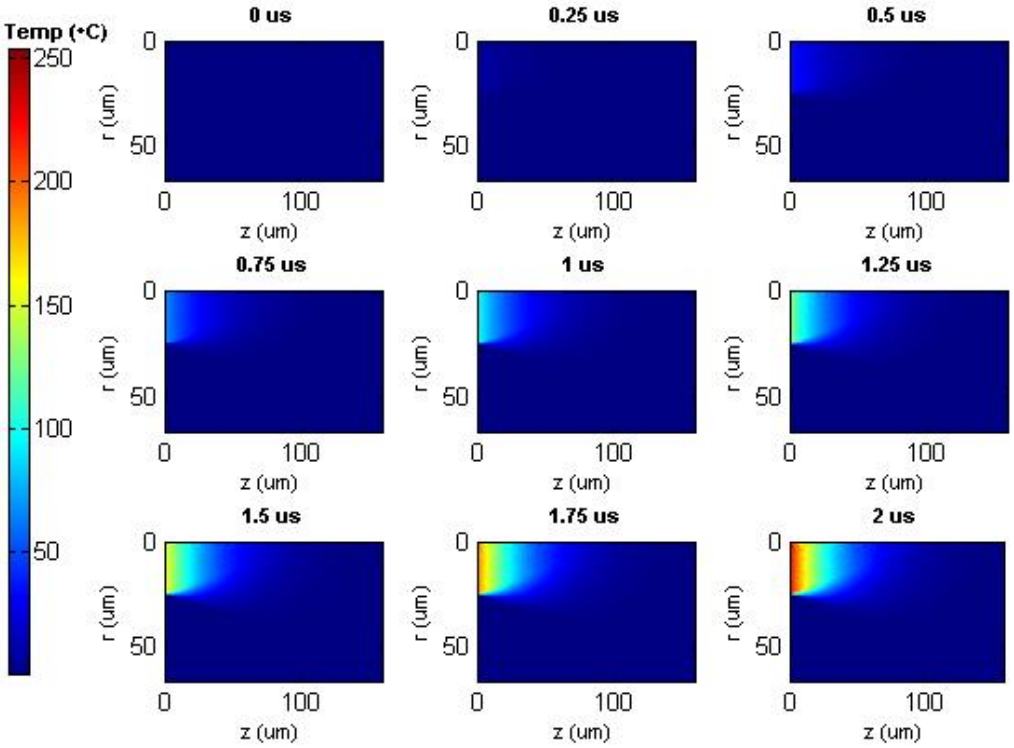

Figure 44: Temperature contour plots at several times for d_s = 50 μm.

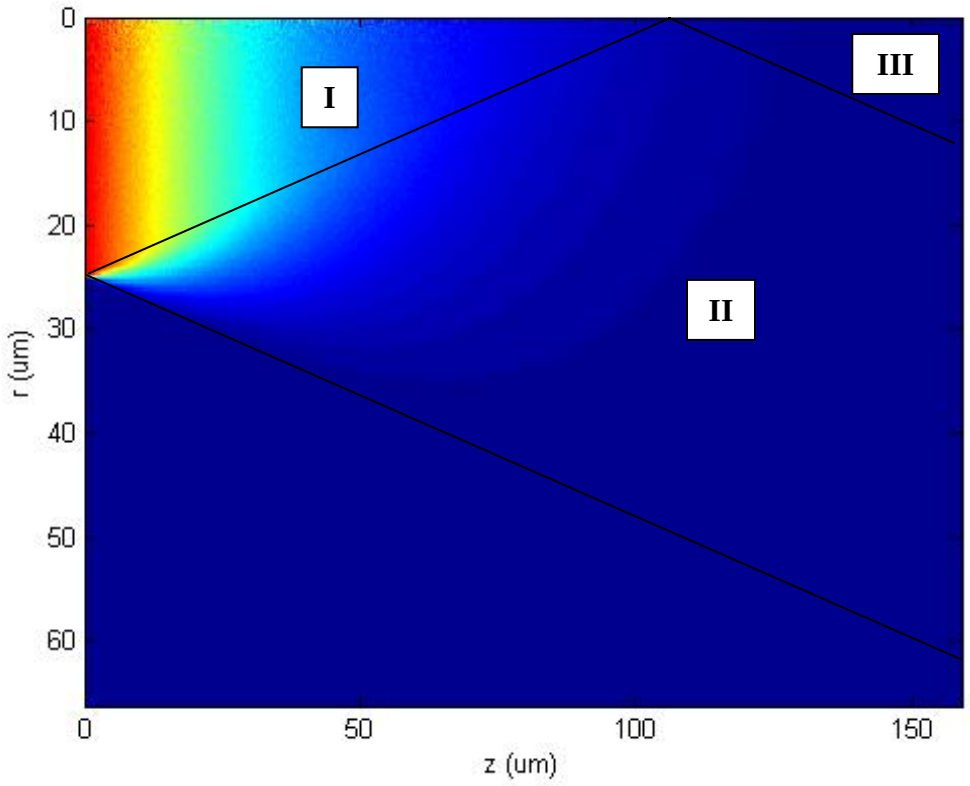

Figure 45: Spatial energy distribution function superimposed on regions I, II, and III.

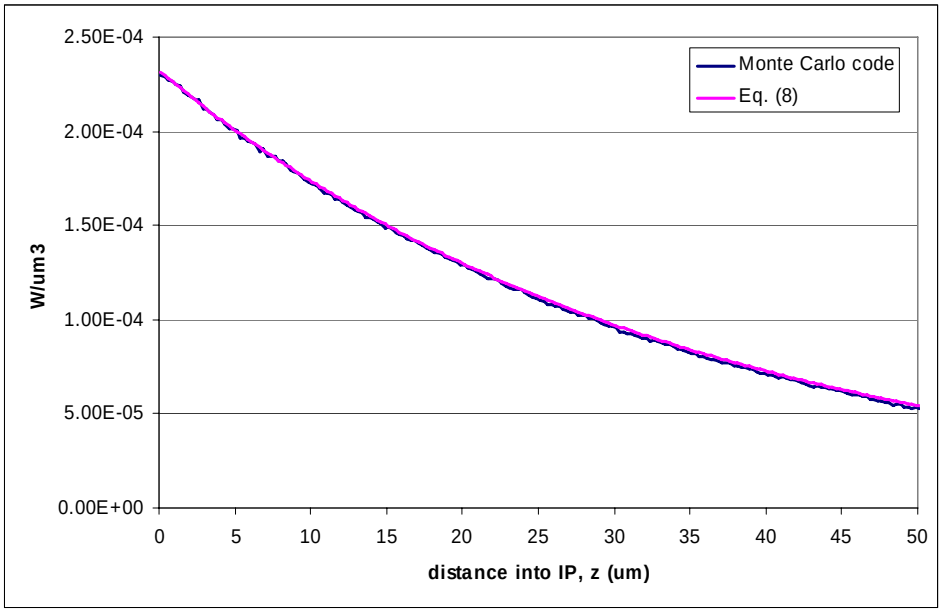

Figure 46: Comparison of Monte Carlo code in region I with 1-D result.

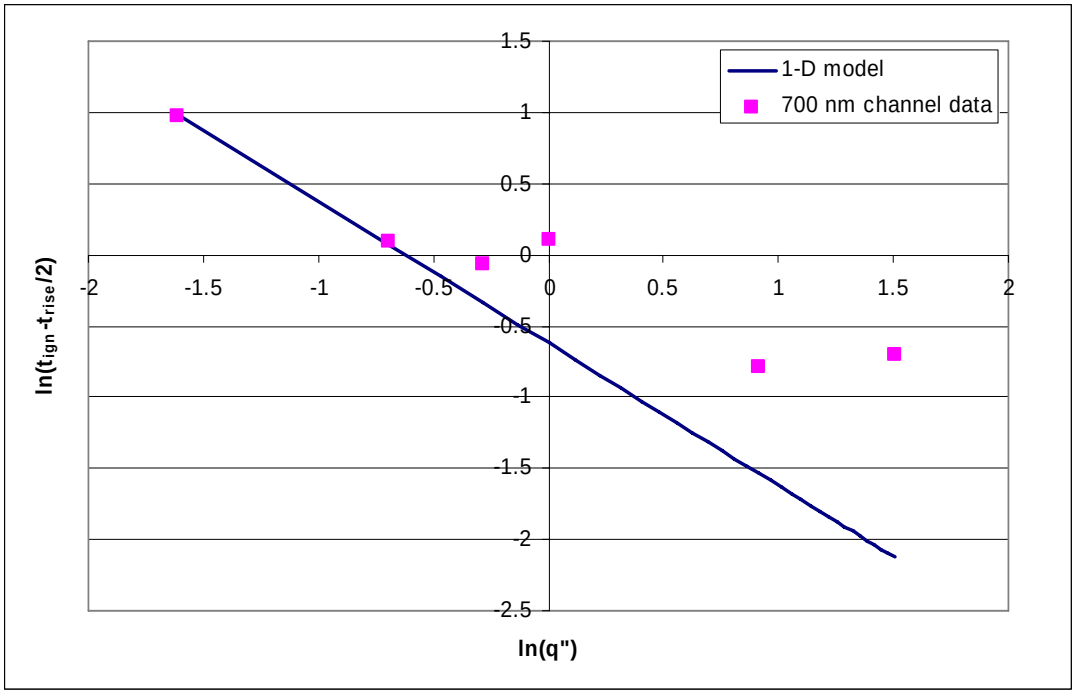

Figure 47: Comparison of 700 nm channel data and results predicted by 1-D model.

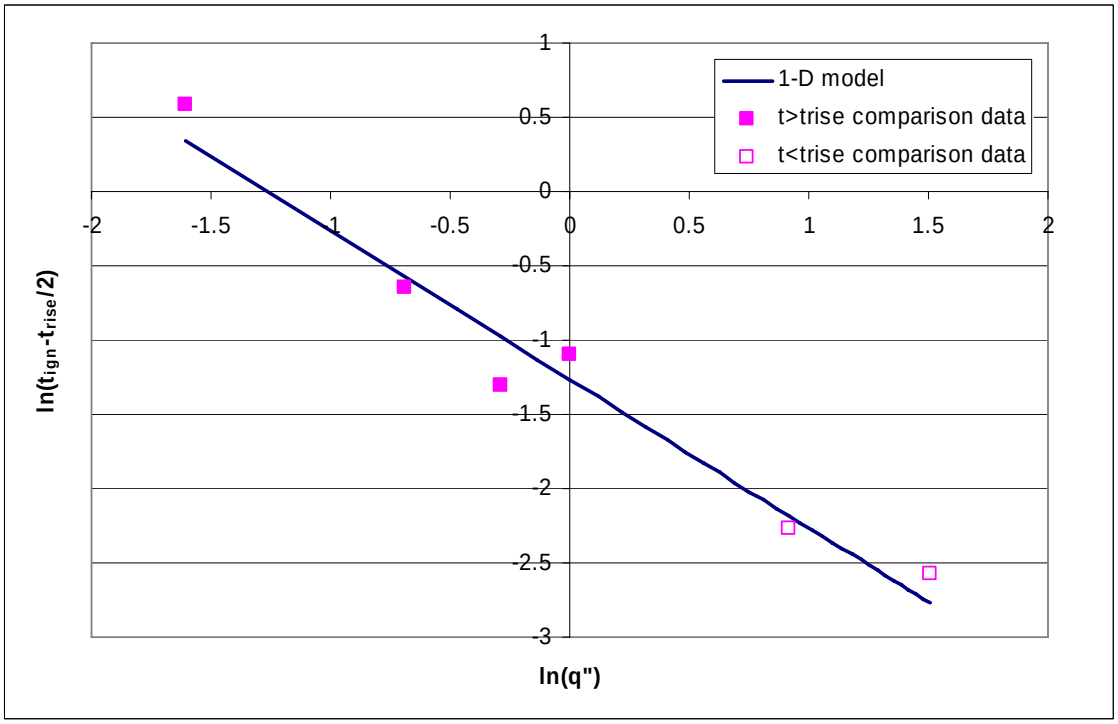

Figure 48: Comparison of detector comparison data and t > t_{rise} results predicted by 1-D model.

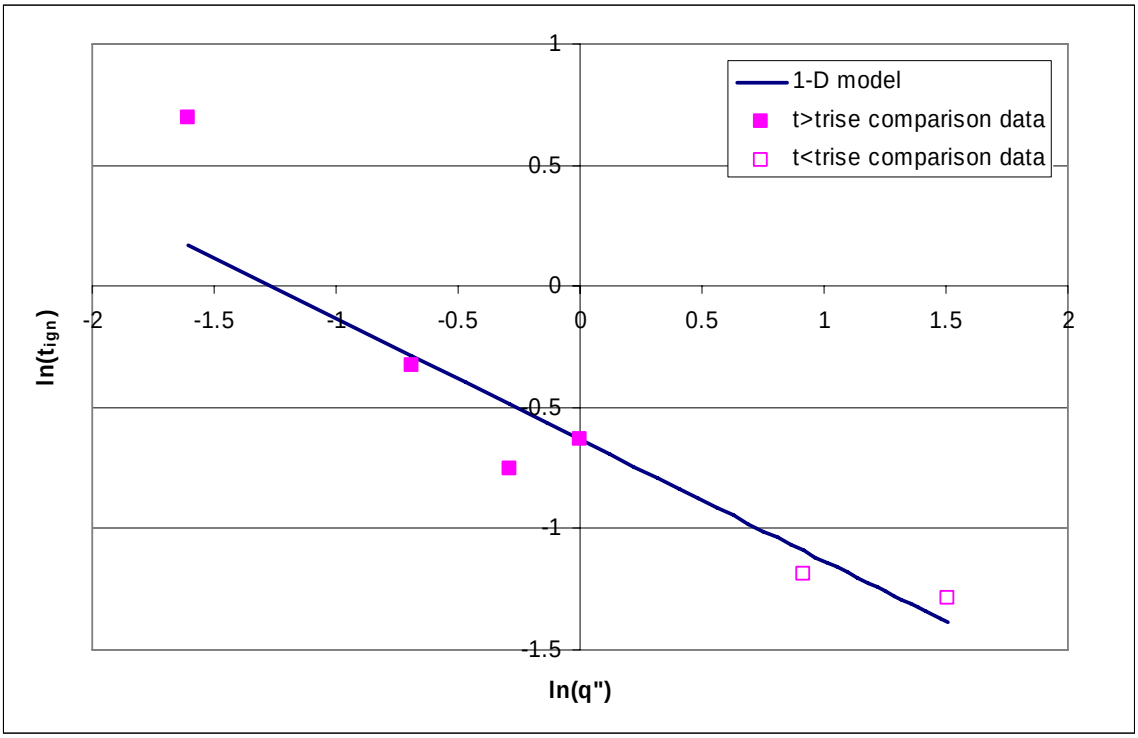

Figure 49: Comparison of detector comparison data and $t < t_{rise}$ results predicted by 1-D model.

12 Tables

Table 1: Test matrix.

Power Density [MW/cm^2]	Spot Size [μm]	# of Exp. [-]
0.2	200	5
0.2	100	5
0.5	100	5
0.5	50	5
0.75	100	5
0.75	50	2
1	50	5
2.5	50	5
4.5	40	9

Table 2: Wavelengths, filter characteristics, and detector types used in the five color pyrometer.

Wavelength (nm)	Band pass filter bandwidth (nm)	Transmission of band pass filter	# Dichroic filters in path (reflected)	# Dichroic filters in path (transmitted through)	Detector type
700	22	75%	2	0	PMT
900	12	80%	2	1	PMT
1270	10	50%	1	2	InGaAs
1600	60	85%	1	1	InGaAs
2100	90	75%	0	2	InGaAs

Table 3: Estimated transmittances of pyrometer components.

Component type	Transmission (%)
Collection optics (2 lenses)	88%
Collimating and focusing optics (2 lenses)	88%
Fiber transmission	Variable—usually 95%-100%
Fiber coupling efficiency	80%
Transmission through Dichroic	80%
Reflection from Dichroic	95%

Table 4: Five color pyrometer detector parameters.							
Wavelength (nm)	Detector Model #	Active area diameter (mm)	Capacitance (pF)	Time Constant (ns)	NEP (W/ Hz)	NEP @ 10MHz (pW)	Sensitivity @ wavelength (A/W)
1270	J22TE2-66C-R01M-1.7	1	125	625	8.9e-16	2.81	0.9
1600	J23TE4-3CN-R250U-1.9	0.25	75	375	4e-16	1.26	1.0
2100	J23TE4-3CN-R250U-2.4	0.25	75	375	5.1e-15	16.1	1.15

Table 5: Properties of NIR detector amplifiers.			
Model #	Gain	Noise	Noise @ 10MHz
313A-1	20 KV/A	10 pA/ Hz	0.0031 pA
322-6	40 dB	380 pV/ Hz	0.12 pV

Table 6: S/N estimate for NIR detectors assuming 10 nW input energy at each detector.						
	Output at Detector (nA)	Input to Preamplifier (nA)	Output of Preamplifier (uV)	Input to Amplifier (uV)	Output from Amplifier (V)	Overall S/N Ratio
Signal 1270 nm	9	9	180	180	1.8	3.5×10^3
Noise 1270 nm	.00253	.0025331	0.051	0.051	0.00051	
Signal 1600 nm	10	10	200	200	2	8×10^3
Noise 1600 nm	.00126	.0012631	0.025	0.025	0.00025	
Signal 2100 nm	11.5	11.5	230	230	2.3	6.2×10^2
Noise 2100 nm	.0185	.0185031	0.37	0.37	0.0037	

Table 7: Summary of variable pulse width experiments.

			Unfiltered PD		700 nm Channel			
PW	E Pulse	Result	t_{ign}	E_{ign}	$t_{ss\ ign}$	$E_{ss\ ign}$	t_{out}	SN
[µs]	[µJ]	[-]	[µs]	[µJ]	[µs]	[µJ]	[µs]	[-]
3.00	198.0	FIRE	0.25	8.0	0.75	40.7	4.24	SN01-C17
2.00	124.0	FIRE	0.27	8.9	0.67	32.1	4.18	SN02-C21
1.00	65.0	FIRE	0.28	9.6	0.62	31.1	4.22	SN03-C23
0.50	33.0	FIRE	0.24	7.7	0.64	28.8	4.35	SN04-C24
0.50	33.0	FIRE	0.26	8.4	0.80	32.3	4.38	SN05-C28
0.45	32.0	FIRE	0.38	15.8	0.68	30.1	4.17	SN06-C29
0.45	32.0	NO FIRE	-	-	-		-	SN07-C30
0.40	28.0	NO FIRE	-	-	-		-	SN08-C27
0.25	17.5	NO FIRE	-	-	-		-	SN09-C26
		Average	**0.28**	**9.7**	**0.69**	**32.5**	**4.26**	
		Std. Dev.	**0.05**	**3.0**	**0.07**	**4.2**	**0.09**	

Table 8: Summary of the averaged data from all experiments.

D	q_0"	t_{ign}	$t_{ss\ ign}$	t_{out}
[µm]	[MW/cm^2]	[µs]	[µs]	[µs]
200	0.2	1.98	2.13	5.32
100	0.2	2.10	3.56	6.62
100	0.5	0.75	1.40	4.47
50	0.5	0.68	1.16	4.38
100	0.75	0.44	1.10	4.15
50	0.75	0.54	1.22	4.54
50	1	0.53	1.31	4.89
50	2.5	0.30	0.66	4.10
40	4.5	0.28	0.69	4.26

Table 9: Output times with differences.

d_s	q_0"	t_{ign}	$t_{ss\ ign}$	t_{out}	t_{out}-t_{ign}	t_{out}-$t_{ss\ ign}$	$t_{ss\ ign}$-t_{ign}
[µm]	[MW/cm^2]	[µs]	[µs]	[µs]	[µs]	[µs]	[µs]
200	0.2	1.98	2.13	5.32	3.34	3.19	0.15
100	0.2	2.10	3.56	6.62	4.52	3.06	1.46
100	0.5	0.75	1.40	4.47	3.72	3.07	0.65
50	0.5	0.68	1.16	4.38	3.70	3.22	0.48
100	0.75	0.44	1.10	4.15	3.72	3.06	0.66
50	0.75	0.54	1.22	4.54	4.00	3.32	0.68
50	1	0.53	1.31	4.89	4.35	3.58	0.78
50	2.5	0.30	0.66	4.10	3.80	3.45	0.35
40	4.5	0.28	0.69	4.26	3.98	3.57	0.41
				Average	**3.90**	**3.28**	**0.62**
				Std. Dev.	**0.36**	**0.21**	**0.37**

Table 10: Values used for Monte Carlo code validation.	
Property	Value
β	290 cm^{-1}
α	0.8
ρ	1.55 g/cm^3
c_p	1.2 J/g-K
t_{rise}	1.3 μs
q_0''	$1x10^6$ W/cm^2
T_0	0ºC

Table 11: Values used for 3-D Monte Carlo code.	
Parameter	Value
q_0''	1000 kW/cm^2
n_s	1.76
d_f	100 nm
d_s	50 nm
α	0.8
β	290 cm^{-1}
N.A.	0.22
t_{rise}	0.4 μs
ρ	1.55 g/cm^3
c_p	1.2 J/g-K
T_0	0ºC

Table 12: Averaged data for all experiments with energy density.

D [μm]	q_0'' [MW/cm^2]	t_{ign} [μs]	E''_{ign} [$nJ/\mu m^2$]	$t_{ss\ ign}$ [μs]	$E''_{ss\ ign}$ [$nJ/\mu m^2$]	t_{out} [μs]
200	0.2	1.98	3.5	2.13	3.8	5.32
100	0.2	2.10	4.0	3.56	7.0	6.62
100	0.5	0.75	2.9	1.40	5.9	4.47
50	0.5	0.68	2.5	1.16	5.1	4.38
100	0.75	0.44	2.4	1.10	7.4	4.15
50	0.75	0.54	3.0	1.22	7.0	4.54
50	1	0.53	3.7	1.31	11.2	4.89
50	2.5	0.30	4.3	0.66	12.7	4.10
40	4.5	0.28	9.7	0.69	32.5	4.26

13 Appendix A: Summary of Experimental Data

		Ignition		Self-Sustained Ignition			
d_s	q_0"	t_{ign}	E"$_{ign}$	t_{ign}	E"$_{ss\ ign}$	t_{out}	SN
[μm]	[MW/cm^2]	[μs]	[nJ/μm^2]	[μs]	[nJ/μm^2]	[μs]	[-]
52	2.5	0.23	2.4	0.81	15.9	4.41	SN10-B17
49	2.5	0.38	5.5	0.62	11.2	4.17	SN11-B18
50	2.5	0.21	3.2	0.78	16.9	4.28	SN12-B19
51	2.5	0.47	8.0	0.61	11.6	4.20	SN13-B20
48	2.5	0.23	2.3	0.46	8.0	3.46	SN14-B08
	Average	**0.30**	**4.3**	**0.66**	**12.7**	**4.10**	
	Std. Dev.	**0.12**	**2.5**	**0.14**	**3.6**	**0.37**	
49	1.0	0.43	3.0	1.39	11.7	5.04	SN15-B11
51	1.0	0.72	5.4	1.42	12.0	4.79	SN16-B12
49	1.0	0.48	3.2	1.04	8.8	4.56	SN17-B24
51	1.0	0.41	2.6	1.41	12.4	5.43	SN18-B21
49	1.0	0.62	4.6	1.28	11.4	4.61	SN19-B26
	Average	**0.53**	**3.7**	**1.31**	**11.2**	**4.89**	
	Std. Dev.	**0.13**	**1.2**	**0.16**	**1.4**	**0.36**	
97	0.75	-	-	0.94	6.1	4.13	SN20-A13
98	0.75	0.35	1.7	1.3	9.0	3.99	SN21-A14
101	0.75	0.31	1.4	1.2	8.0	4.46	SN22-A28
100	0.75	0.62	3.9	1.04	7.1	4.22	SN23-A29
101	0.75	0.46	2.6	1.01	6.5	3.97	SN24-A17
		0.44	**2.4**	**1.10**	**7.4**	**4.15**	
		0.14	**1.1**	**0.15**	**1.1**	**0.20**	
51	0.75	0.45	2.5	1.50	8.0	4.50	SN25-B27
49	0.75	0.63	3.6	0.94	5.9	4.57	SN26-B30
	Average	**0.54**	**3.0**	**1.22**	**7.0**	**4.54**	
	Std. Dev.	**0.13**	**0.8**	**0.40**	**1.5**	**0.05**	
99	0.5	0.64	2.3	0.98	3.9	3.95	SN27-A07
100	0.5	-	-	1.39	6.2	4.47	SN28-A21
100	0.5	0.84	3.5	1.67	7.6	5.19	SN29-A19
102	0.5	0.74	3.0	1.59	7.1	4.53	SN30-A15
103	0.5	0.76	2.9	1.35	4.5	4.20	SN31-A30
	Average	**0.75**	**2.9**	**1.40**	**5.9**	**4.47**	
	Std. Dev.	**0.08**	**0.5**	**0.27**	**1.6**	**0.47**	
49	0.5	0.66	2.4	-	-	4.39	SN32-B04
50	0.5	0.70	2.6	0.93	3.7	4.16	SN33-B05
48	0.5	-	-	1.29	5.8	4.81	SN34-B22
53	0.5	-	-	1.15	5.2	4.14	SN35-B23
52	0.5	-	-	1.27	5.8	4.38	SN36-B06
	Average	**0.68**	**2.5**	**1.16**	**5.1**	**4.38**	
	Std. Dev.	**0.03**	**0.1**	**0.17**	**1.0**	**0.27**	
202	0.2	1.98	3.3	2.16	3.7	5.12	SN37-A08
200	0.2	1.42	2.7	1.55	3.0	4.66	SN38-A09
198	0.2	2.12	3.8	2.17	3.8	5.31	SN39-A25
196	0.2	2.02	3.6	2.24	4.1	5.51	SN40-A26
206	0.2	2.38	4.0	2.54	4.3	6	SN41-A27
	Average	**1.98**	**3.5**	**2.13**	**3.8**	**5.32**	
	Std. Dev.	**0.35**	**0.5**	**0.36**	**0.5**	**0.49**	
100	0.2	-	-	3.38	6.7	6.47	SN42-A12
98	0.2	-	-	3.60	7.1	6.85	SN43-A22
99	0.2	-	-	3.48	6.9	6.51	SN44-A23
97	0.2	-	-	3.53	6.9	6.79	SN45-A24
97	0.2	2.1	4.1	3.80	7.6	6.47	SN46-A31
	Average	**2.10**	**4.1**	**3.56**	**7.0**	**6.62**	
	Std. Dev.	**-**	**-**	**0.16**	**0.3**	**0.19**	

14 Appendix B: Fortran Source Code for Monte-Carlo Program

Main Program

```
      Program LDImain
C
C  This program's purpose is to find the energy distribution
C  in the LDI laser column
C
C  All dims are in um and radians unless noted.
C
C-----------------------------------------------------------------
C  MAIN PROGRAM VARIABLE LIST
C
C  parameters to describe general rays
C
C  x(1,2,3)    = ray origen and ending x,y,z coordinates
C  x1(1,2,3)   = ray x,y,z cosines
C
C  geometry and radiative property parameters
C
C  Ds       = HE laser spot diameter
C  rs       = HE laser spot radius
C  PD       = Power density at HE surface
C  Pwr      = total power deposited at surface
C  Df       = fiber diameter
C  rf       = fiber radius
C  NA       = numerical aperature of fiber
C  nw       = index of refraction of window
C  alpha    = HE surface absorptivity
C  K        = HE material extinction coefficient
C  sinS     = sine of angle limit of HE incident raditaion
C  zmax     = maximum range of z allowed
C  rmax     = maximum range of r allowed
C  incr     = resolution (in um) of solution
C  Vol      = volume contained in annular incremental region
C
C  Operational parameters/subroutines
C
C  N      = total number of rays from HE surface
C  NR     = number of increments (resolution) in R
C  NZ     = number of increments (resolution) in Z
C  data   = array containing r vs z vs heat gen
C  number = integer passed with random # generator (do not screw with)
C  phi    = phi polar angle (in x-y plane)
C  theta  = theta azimuthal angle
C  r      = radial location
C  z      = vertical distance from HE-window surface
C  H,I    = increment used here and there (always set to 0 before using)
C  Pi     = you can always use more Pi
C
C  Needed subroutines (not geometry specific)
C
C  ran2()   = random number generator
C
      DoublePrecision Pi,x(3),x1(3)
      DoublePrecision Ds, PD, Df, NA, nw, alpha, K, rs, rf
      DoublePrecision phi, theta, r, z, sinS, rmax, zmax, incr
      DoublePrecision Vol, Pwr, L, r1, r2
      Integer number, N, I, H, NR, NZ, Ndata(0:10000,0:10000)
      Integer rrow, zcol
      Character*20 filename,filename2
C
C  Get file names and necessary data from user
```

```
C
      Print*, 'Enter file name for flux distribution data file (CSV)'
      Read*, filename
      Open (Unit=10,file=filename,status='new')
      Print*, 'Enter Power Density at HE (in kW/cm2)'
      Read*, PD
      Print*, 'Enter fiber diameter (in um)'
      Read*, Df
      Print*, 'Enter fiber NA'
      Read*, NA
      Print*, 'Enter Window index of refraction'
      Read*, nw
      Print*, 'Enter HE spot diameter (in um)'
      Read*, Ds
      Print*, 'Enter HE surface absorbtivity'
      Read*, alpha
      Print*, 'Enter HE extinction coefficient (cm^-1)'
      Read*, K
      K = K*1.0d-04
C
C set parameters
C
      Print*, 'Initializing Parameters...Please Wait'
      N  = 100000000
      Pi = 3.141592654d+00
      rs = Ds/2.0d+00
      rf = Df/2.0d+00
      incr = 0.25d+00
      Pwr = PD*Pi*rs*rs*1.0d-05
      sinS = NA*rf/(nw*rs)
      zmax =  - dlog(1.0d-02)/K
      rmax = rs+zmax*dtan(dasin(sinS))
      NR = idnint(rmax/incr)
      NZ = idnint(zmax/incr)
      I=0
      Do 20 I=0,10000
        H=0
        Do 10 H=0,10000
          Ndata(H,I)=0
   10   Continue
   20 Continue
C
C*******************************************************
C  Monte carlo Algorithm
C
      I=0
      Do 100 I=1,N
        If (mod(I,100000).le.1) Print*, 'N= ',I
C
C  Set random entry position and direction cosines
C
        phi=2.d+00*Pi*dble(ran2(number))
        r=rs*dsqrt( dble( ran2(number) ) )
        x(1)=r*dcos(phi)
        x(2)=r*dsin(phi)
        x(3)=0.0d+00
        theta=dAsin(sinS*dsqrt(dble(ran2(number))))
        phi=2.d+00*Pi*dble(ran2(number))
        x1(1)=dsin(theta)*dcos(phi)
        x1(2)=dsin(theta)*dsin(phi)
        x1(3)=dcos(theta)
C
C  Set random penetration length and find ray ending
C
        L = - dlog(dble(ran2(number)))/K
        x(1) = x(1) + x1(1)*L
        x(2) = x(2) + x1(2)*L
        x(3) = x(3) + x1(3)*L
C
C  Find r, z location of ray ending and save to data matrix
C
```

```
        r = dsqrt(x(1)*x(1) + x(2)*x(2))
        z = x(3)
        zcol = idint(dble(NZ)*z/zmax)
        rrow = idint(dble(NR)*r/rmax)
        If (zcol.gt.NZ) zcol = NZ+1
        If (rrow.gt.NR) rrow = NR+1
        Ndata(rrow,zcol) = Ndata(rrow,zcol) + 1
  100 Continue
C
C*******************************************************
C  Print Data to file
C
C  Headers for data files (tab deliminated)
C
      Write(10,*) 'LDI Input Flux Data'
      Write(10,*) 'Power Density at HE surface (kW/cm2)=,,,,',PD
      Write(10,*) 'Fiber diameter (um)=,,,,',Df
      Write(10,*) 'Fiber NA=,,,,',NA
      Write(10,*) 'Window Index of refraction=,,,,',nw
      Write(10,*) 'Spot diameter (um)=,,,,',Ds
      Write(10,*) 'HE surface absorbtivity=,,,,',alpha
      K = K/1.0d-04
      Write(10,*) 'HE extinction coefficient (cm^-1)=,,,,',K
      Write(10,*) '# Monte Carlo Rays=,,,,',N
      Write(10,*) ' '
      Write(10,*) 'each column is a different distance z from the HE sur
     cface (in um)'
      Write(10,*) 'each row is a different raidal distance r from the ce
     cnterline (in um)'
      Write(10,*) 'data is in W/um^3'
      Write(10,*) ' '
C
      Write(10,890) ','
      H=0
      Do 110 H=0,NZ+1
        Write(10,900) (dble(H)*incr + incr/2.0d+00)
  110 Continue
      H=0
      Do 130 H=0,NR+1
        Write(10,910) (dble(H)*incr + incr/2.0d+00)
        r1 = dble(H)*incr
        r2 = dble(H)*incr + incr
        Vol = Pi*incr*(r2*r2-r1*r1)
        I=0
        Do 120 I=0,NZ+1
          Write(10,920) (dble(Ndata(H,I))/dble(N))*(Pwr/Vol)*alpha
  120   Continue
  130 Continue
      Print*, 'Program finished, data has been written to file'
C
C  Print format statements
C
  890 Format (A,$)
  900 Format (F8.3,',',$)
  910 Format (/,F8.3,',',$)
  920 Format (E11.4,',',$)
C
C  End program
C
      close (unit=10)
      end
```

Random number generator

```
      Function ran2(idum)
C
C  This function creates random numbers.  It was copied
C  from “Numerical Recipies in Fortran”.  It must be supplied
C  with a negative integer seed value, idum. After the initial
```

```
C  seed for idum, do not change this variable in the main
C  program
C
      Integer idum,IM1,IM2,IMM1,IA1,IA2,IQ1,IQ2,IR1,IR2,NTAB,NDIV
      Real ran2,AM,EPS,RNMX
      Parameter (IM1=2147483563,IM2=2147483399,AM=1./IM1,IMM1=IM1-1,
     *     IA1=40014,IA2=40692,IQ1=53668,IQ2=52774,IR1=12211,
     *     IR2=3791,NTAB=32,NDIV=1+IMM1/NTAB,EPS=1.2e-7,RNMX=1.-EPS)
      Integer idum2,j,k,iv(NTAB),iy
      Save iv,iy,idum2
      Data idum2/123456789/, iv/NTAB*0/, iy/0/
      if (idum.le.0) then
          idum=max(-idum,1)
          idum2=idum
          do 10 j=NTAB+8,1,-1
              k=idum/IQ1
              idum=IA1*(idum-k*IQ1)-k*IR1
              if (idum.lt.0) idum=idum+IM1
              if (j.le.NTAB) iv(j)=idum
  10      Continue
          iy=iv(1)
      endif
      k=idum/IQ1
      idum=IA1*(idum-k*IQ1)-k*IR1
      if (idum.lt.0) idum=idum+IM1
      k=idum2/IQ2
      idum2=IA2*(idum2-k*IQ2)-k*IR2
      if (idum2.lt.0) idum2=idum2+IM2
      j=1+iy/NDIV
      iy=iv(j)-idum2
      iv(j)=idum
      if (iy.lt.1) iy=iy+IMM1
      ran2=min(AM*iy,RNMX)
      return
      end
```

Distribution

1	MS 0123	Donna Chavez	01011
1	MS 0512	Tom Blejwas	02500
1	MS 0836	Gene Hertel	09116
2	MS 0899	Technical Library	09616
1	MS 1133	Greg Scharrer	05916
10	MS 1452	Everett Hafenrichter	02552
1	MS 1452	Tom Hafenrichter	02552
1	MS 1452	Steve Harris	02552
1	MS 1452	Michelle Steyskal	02552
1	MS 1452	Bill Tarbell	02552
1	MS 1452	Adam Wadin	02552
1	MS 1452	Eric Welle	02552
1	MS 1453	Wendy Cieslak	02550
1	MS 1453	Cara Murray	02553
1	MS 1453	Jim Salas	02553
1	MS 1453	Dan Sanchez	02553
1	MS 1454	Lloyd Bonzon	02554
1	MS 1454	Kevin Fleming	02554
1	MS 1454	Dennis Johnson	02551
1	MS 1454	Mike Kaneshige	02554
10	MS 1454	Robert Pahl	02554
5	MS 1454	Anita Renlund	02554
1	MS 1454	Shane Snedigar	02554
1	MS 1454	Alex Tappan	02554
1	MS 1455	Leanna Minnier	02555
1	MS 9018	Central Technical Files	08945-1
5	MS 9106	Chrisma Jackson	08226